9-1-2015

Precise Characterization and Investigation of Laser Cooling in III-V Compound Semiconductors

Chengao Wang

Chengao Wang
Candidate

Physics and Astronomy
Department

This dissertation is approved, and it is acceptable in quality and form for publication:

Approved by the Dissertation Committee:

Mansoor Sheik-Bahae, Chairperson

Richard Epstein

Kevin Malloy

Ganesh Balakrishnan

PRECISE CHARACTERIZATION AND INVESTIGATION OF LASER COOLING IN III-V COMPOUND SEMICONDUCTORS

BY

CHENGAO WANG

B.S., Applied Physics, Shanghai Jiao Tong University, 2004
M.S., Optical Science and Engineering, The University of New Mexico, 2007

DISSERTATION

Submitted in Partial Fulfillment of the

Requirements for the Degree of

Doctor of Philosophy
Optical Science and Engineering

The University of New Mexico

Albuquerque, New Mexico

July, 2015

DEDICATION

To my parents and my wife.

ACKNOWLEDGMENTS

I am grateful to Professor Mansoor Sheik-Bahae for his academic advice, support and encouragement during the many years of my Ph.D. program at UNM. He is very knowledgeable and always has a deep understanding of the physics. He makes himself available to his students at all times. The learning experience I gained in Professor Sheik-Bahae's group is invaluable and will be a treasure for the rest of my life.

I sincerely appreciate Professor Richard Epstein, Professor Kevin Malloy, and Professor Ganesh Balakrishnan for their scientific support and advisement throughout my academic years.

Dr. Mike Hasselbeck was involved in this project and contributed hugely. Working with him was a wonderful experience. I deeply thank him for his time and scientific support throughout my project.

I greatly appreciate Dr. Jerry Olson at National Renewable Energy Laboratory, Dr. Jeffrey Cederberg at Sandia National Laboratory and Dr. Andreas Stintz at Center for High Technology Materials at UNM for their support in providing us with GaAs samples.

I would like to thank all the former and current group members the fellow students: Dr. Babak Imangholi, Dr. Denis Seletskiy, Dr. Daniel Bender, Dr. Wendy Patterson, Chia-Yeh Li, Dr. Seth Melgaard, Zhou Yang, Aram Gragossian, Mohammadreza Ghasemkhani, Dr. Alexander Albrecht and Nathan Giannini for their generous help and useful discussions through the years.

I wish to thank Professor Rolf Binder at University of Arizona for his great support and advice on the theory about laser cooling in semiconductors.

I would like to thank Beth Fuchs, Douglas Wozniak, Dr. Chris Hains, Steve Wawrzyniec and Dr. Xiang He at Center for High Technology Materials for their support with material processing and equipment training.

I appreciate all the help from the department staff: Mary Dewitt, Jaye Jensen, Elliott Bailey, Doris Williams, Alisa Gibson, Gary Harrison, Tom Hess, Sandra Ortiz, Berilyn Thomas, Steve Portillo for graduate advisement, purchasing and computers.

I would like to thank John DeMoss and Anthony Gravagne for making various mechanical and electronic parts for my experiments.

PRECISE CHARACTERIZATION AND INVESTIGATION OF LASER COOLING IN III-V COMPOUND SEMICONDUCTORS

By

Chengao Wang

B.S., Applied Physics, Shanghai Jiao Tong University, 2004
M.S., Optical Science and Engineering, The University of New Mexico, 2007
Ph.D., Optical Science and Engineering, The University of New Mexico, 2015

ABSTRACT

The physics and engineering issues associated with laser cooling of III-V compound semiconductors, in particular GaAs double heterostructures (DHS), are theoretically and experimentally investigated. This research addresses the key concepts of external quantum efficiency (EQE) and parasitic background absorption in a semiconductor laser cooler. The external quantum efficiency describes how well recombination radiation is removed from the cooling device and is precisely measured by All-optical

Scanning Laser Calorimetry (ASLC). Using this technique, a record external quantum efficiency of 99.5% has been obtained with a GaAs laser cooler held at 100 K. However, high background absorption has hindered the observation of net cooling. Pulsed Power-dependent photoluminescence measurement (Pulsed PDPL) is proved to be an efficient way to determine the external quantum efficiency and screen the sample quality before device fabrication. We observe lateral lasing effect in both double heterostructure and quantum well semiconductors and show that the phenomenon can be explained by the effect of bandgap renormalization due to Coulomb screening. The knowledge gained in the research described here is essential toward the realization of net laser cooling in III-V compound semiconductors in the future.

Table of Contents

List of Figures

List of Tables

Chapter 1

Introduction

1.1 Overview

The term “laser cooling” is most often used in association with cooling and trapping of dilute gases of atoms and ions to extremely low temperatures. This area of science has progressed rapidly and has facilitated the observation of Bose-Einstein condensates and many related phenomena [1-3]. In laser cooling of gases, the translational energy of atoms is lowered through interaction with a laser field. Recently, cooling of a high-density gas through collisional redistribution of radiation has been demonstrated [4].

In the solid phase, atoms do not possess relative translational motion – their thermal energy is largely contained in the vibrational modes of the lattice, or phonons. In laser cooling of solids, the topic of this dissertation, photons in the red tail of the absorption spectrum are absorbed from a monochromatic laser source followed by spontaneous emission of more energetic (blue-shifted) photons. Extra energy, or heat, is extracted from lattice phonons. The removal of these phonons is equivalent to cooling the solid. This process has also been termed “anti-Stokes fluorescence” or “luminescence up-conversion” cooling [5].

To achieve laser cooling, thermal energy must be removed from the system in the three-step process illustrated in Fig.1.1. The cooling cycle proceeds as follows: i) a pump photon with energy less than the mean luminescence energy ($h\nu$) is absorbed to create excited electrons, ii) the optically excited electrons gain additional thermal energy from the lattice through phonon absorption and equilibrate with lattice, and iii) excited electrons return to ground state by emitting photons with an average mean photon energy ($h\nu_f$) that is higher than the pump photon ($h\nu$). Fig.1.2 shows the absorption and emission of a typical two level system. If the excitations decay primarily by photon emission and these luminescence photons are efficiently removed from the sample without heating it, net cooling can occur.

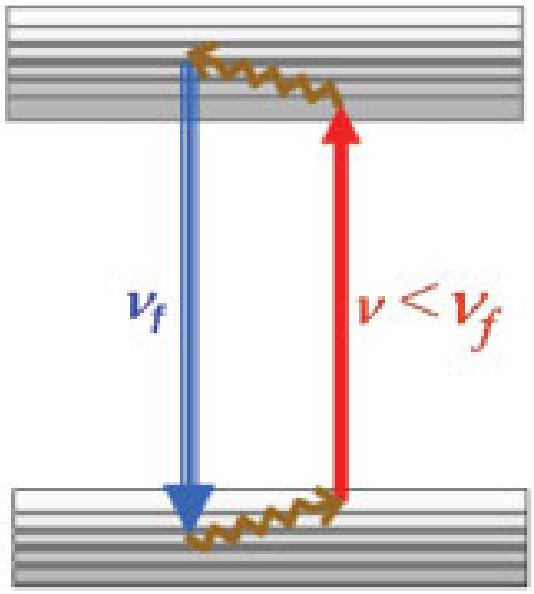

Fig.1.1. Laser cooling cycle in a solid. The light source of frequency hν excites atoms near the top of the ground state to the bottom of the excited state. Radiative decays occurring after thermalization emit photons with average energy $h\nu_f > h\nu$.

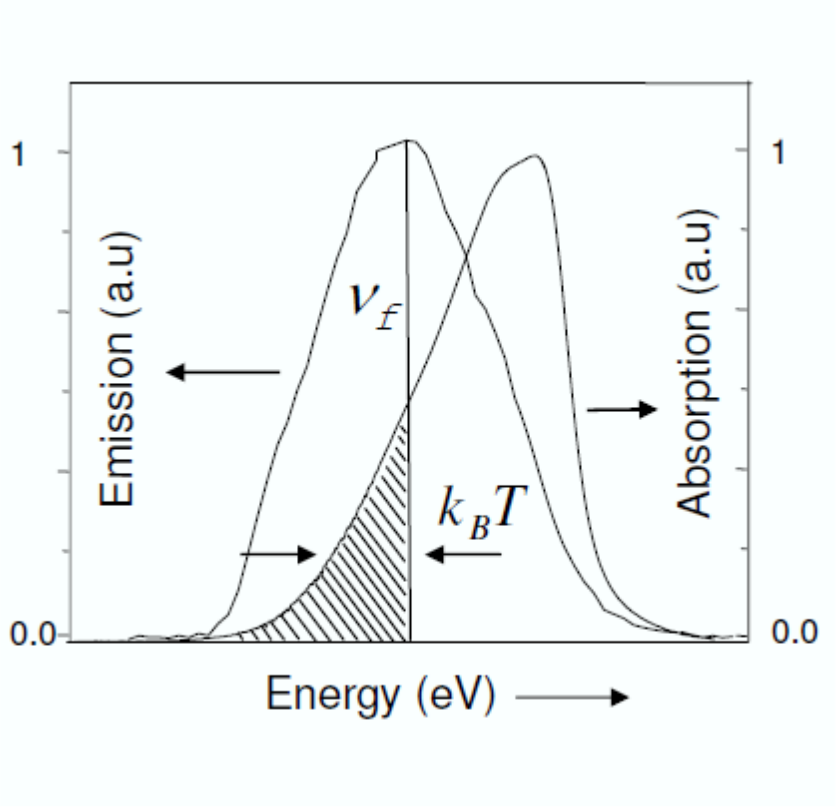

Fig.1.2. Absorption and emission of a typical two level system. Pump laser wavelengths longer than mean luminescence wavelength v_f (shaded area) must be used to achieve cooling.

The plausibility of this phenomenon was predicted by German physicist Peter Pringsheim in 1929, more than 30 years before laser was invented [6]. Pringsheim's prediction was initially rejected by some scientists as contrary to the second law of thermodynamics; Landau proved its principle in 1946 [7]. He established that the entropy lost by the sample is compensated by an increase in the entropy of the fluorescence light, which loses monochromaticity, phase coherence, and directionality. Net laser cooling remained elusive until 1995, when the first experimental demonstration of was achieved by Richard Epstein and co-workers at Los Alamos National Laboratories (LANL) [8].

Laser cooling of solids can be exploited to achieve an all-solid-state cryocooler [5, 9, 10] as conceptually depicted in Fig.1.3. The advantages of compactness, no vibrations, no moving parts or fluids, high reliability, and no need for cryogenic fluids have motivated intensive research. Space-borne infrared sensors are likely to be the first beneficiaries, with other applications requiring compact cryocooling reaping the benefits as the technology progresses.

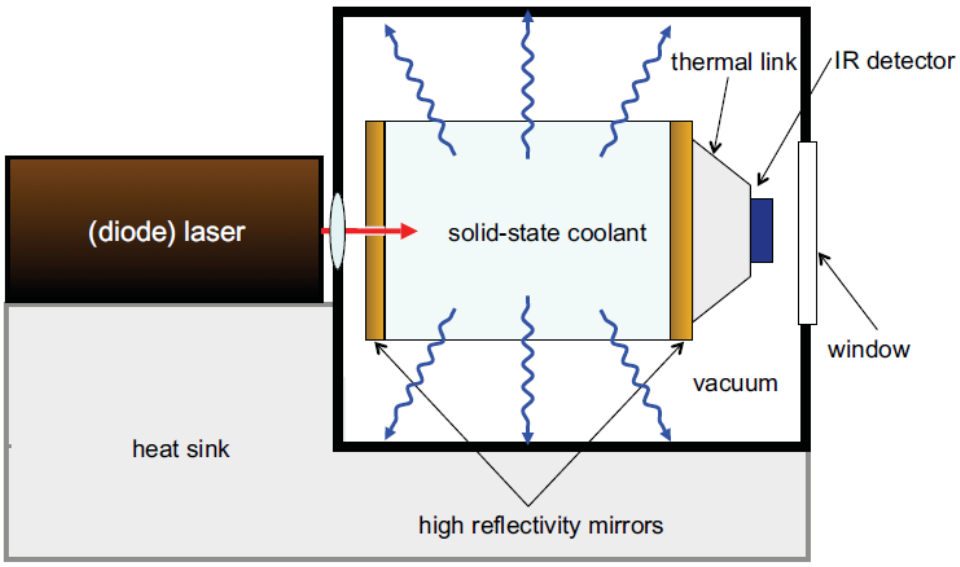

Fig.1.3. Schematic of an optical refrigeration system. Pump light is efficiently generated by a semiconductor diode laser. The laser light enters the cooler through a pinhole in one mirror and is trapped by the mirrors until it is absorbed. Isotropic fluorescence escapes the cooler element and is absorbed by the vacuum casing. A sensor or other load is connected in the shadow region of the second mirror [5].

Thermo-electric (TE) coolers based on the Peltier effect are the most relevant competing technology to laser cooling. While TE coolers possess most of the engineering advantages of laser coolers, their ultimate absolute temperature is limited. Multi-stage TE coolers have not been pushed lower than ~ 150 K, which is already

surpassed by the temperature range of state-of-the-art laser cooled rare-earth (RE) doped glasses or crystals [11, 12]. The design of TE coolers trades off absolute temperature for cooling power. In contrast, laser cooled glass can achieve temperatures comparable to a multi-stage TE cooler in a single stage [13, 14].

In many potential applications, the requirements on the pump lasers are not very restrictive. The spectral width of the pump light has to be narrow compared to the thermal spread of the fluorescence. Multimode, fiber coupled laser with spectral widths of several nanometers would be adequate. In an optical refrigerator, the cooling power is of the order 1 percent of the pump laser power. For micro-cooling applications, with mW heat lift, only modest lasers are adequate. For larger heat lifts, correspondingly more powerful lasers are needed. In all cooling applications, the cooling element has to be connected to the device being cooled, the load, by a thermal link; see Fig.1.2. This link siphons heat from the load while preventing the waste fluorescence from hitting the load and heating it.

Another potential application of laser cooling of solids is to eliminate heat production in high-power lasers. Even though laser emission is always accompanied by heat production, Bowman [15, 16] realized that in some laser materials, the pump wavelength can be adjusted so that the spontaneous anti-Stokes fluorescence cooling compensates for the laser heating. Such thermally balanced laser would not suffer thermal defocusing or heat damage.

1.2 Laser cooling in rare-earth doped solids

The first experimental demonstration of net laser cooling by Richard Epstein and co-workers at Los Alamos National Laboratories (LANL) in 1995 [8] used a polished, high purity glass sample (ZBLANP) doped with ytterbium (Yb) atoms. The cooling process occurs in the Yb atomic system, which removes thermal energy from the glass host to achieve net cooling of the sample. They attained a net cooling of 0.3K below ambient temperature. Two technical challenges were addressed and overcome in these experiments. The Los Alamos researchers had to have a system in which i) the vast majority of optical excitations recombine radiatively and ii) there is a minimal amount of parasitic heating due to unwanted impurities. Both of these critical engineering issues are key to the experimental success.

Since then, cooling in Yb has been observed in various host glass materials such as fluorochloride glass (Yb^{3+}:CNBZn), and fluoride glass (Yb^{3+}:BIG) by Fernandez *et al*. [17]. Improvements by the LANL group have led to an absolute temperature of 208 K starting from room temperature, with a corresponding heat lift of 30 mW [18].

Laser cooling has also been observed in different crystals such as: Yb^{3+}:$KGd(WO_4)_2$ [16], Yb^{3+}:YAG [19], Yb^{3+}:Y_2SO_5 [19], Yb^{3+}:KPb_2Cl_5 [20] and Yb^{3+}:BaY_2F_8 [21]. By making use of the sharp Stark resonance of ytterbium ions doped into a crystalline solid (YLF), Seletskiy *et al*. [11] achieved cooling to an absolute temperature of 155 ± 1 K accompanied by 90 mW of heat lift with a single-stage refrigerator. This surpasses the performance of currently available standard Peltier

coolers. Improvements by the same group has cooled Yb:YLF crystal to 91K, the coldest solid-state refrigeration temperature to date [12].

In 2000, Hoyt *et al*. obtained net cooling in thulium-doped glass (Tm^{3+}:ZBLAN) at about twice the laser wavelength of the Yb experiment [22]. This work was important because it confirmed energy gap scaling predictions, led to a temperature decrease of 26 K from room temperature [23]. Cooling by an amount of 1.5 K has been observed in a Tm^{+3}-doped BaY_2F_8 crystal by Patterson *et al.* [24]. More recently, cooling of Er^{3+} doped glass (CNBZn) and crystal (KPb_2Cl_5) at $\lambda \sim 0.870\mu m$ was reported by a Spanish group [25]. The cooling transition used in these experiments is between the ground state and the fourth excited state ($^4I_{9/2}$) of Er^{3+}. The presence of higher excited states in Er^{3+} may prove advantageous since the energy upconversion transitions are endothermic with a high quantum efficiency [25, 26].

1.3 Laser cooling in semiconductors

Although net cooling has been primarily demonstrated in rare-earth doped glasses and crystals, laser cooling of direct-bandgap semiconductors, such as GaAs, is more appealing because 1) Semiconductors have higher cooling power density; 2) much lower achievable cooling temperatures; 3) the opportunity for direct integration into electronic and photonic devices.

In rare-earth doped materials, the cooling transition occurs in localized donor ions within the host material while semiconductor involves transition between extended valence and conduction bands. Indistinguishable charge carriers in Fermi-Dirac

distributions may allow semiconductors to get much colder than RE materials. The highest energy levels of the ground state manifold in the RE-doped systems become less populated as the temperature is lowered, due to Boltzmann statistics. The cooling cycle becomes ineffective when the Boltzmann constant times the lattice temperature becomes comparable to the width of the ground state. This sets a limit of T ~ 100K for most existing RE-doped systems. No such limitation exists in pure (undoped) semiconductors and temperatures as low as 10K may be achievable [27].

Semiconductors should also achieve higher cooling power density compared to RE-materials. The maximum cooling power density (rate of heat removal) is $\approx N \times k_B T/\tau_r$, where N is the photo-excited electron (-hole) density and τ_r is the radiative recombination time. In semiconductors, the optimal density N is limited due to many-body processes and does not exceed that of moderately doped RE systems. We can gain 5–6 orders of magnitude in cooling power density because the radiative recombination rates in semiconductors are much faster than in RE ions.

Laser cooling of semiconductors has been examined theoretically [27-40] as well as in experimental studies [41-48].

Oraevsky [28] and Rivlin *et al.* [29] considered the cooling of a semiconductor crystal via anti-Stokes luminescence. They estimated the optimum carrier density and the lowest attainable temperature. A feasibility study by Sheik-Bahae and Epstein outlined the conditions for net cooling based on fundamental material properties and light management [30]. They considered the critical issues of luminescence trapping and red-shifting which had not been taken into account previously. Researchers at the University of Arizona [27, 31] studied luminescence upconversion in the presence of

partially ionized excitons, which must be understood to attain temperatures approaching 10 K. The role of bandtail states [34], the possible enhancement of laser cooling by including the effects of photon density of states as well as novel luminescence coupling schemes based on surface plasmon polaritons [35, 36] were introduced by Khurgin at Johns Hopkins University.

The first experimental attempt to cool GaAs semiconductor with laser light used a dome lens scheme for luminescence removal as reported by Gauck *et al.* [41]. They placed a passivated GaAs heterostructure between a flat piece of sapphire and a transparent ZnSe dome lens. The entire assembly was clamped using copper wires to achieve an optical interface between the sample and dome (See Fig.1.4). Their laser cooling sample was pumped with a tunable Ti:sapphire laser. Although no net cooling was attained, they observed reduced heating when the laser was tuned below the mean luminescence wavelength while maintaining the same excitation density. This was the first experimental evidence indicating that laser cooling of a semiconductor was possible. An external quantum efficiency of > 96% was deduced for their device.

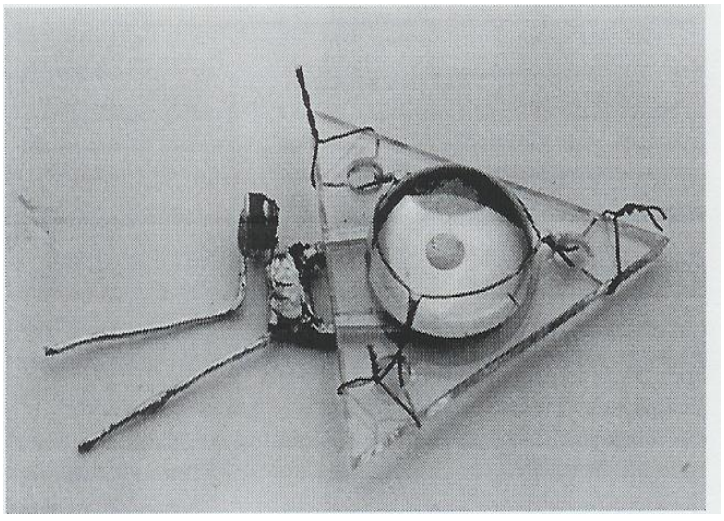

Fig.1.4. A photograph of the index-matching setup as used in Gauck's experiment.

In 1999, A European consortium claimed to observe local laser cooling in a GaAs/AlGaAs quantum well sample by 6K from a bath temperature of 45K [42].

The structure they selected consists of three uncoupled 90-Å-wide GaAs QWs with 0.1mm $Ga_{0.74}Al_{0.26}As$ barriers grown on semi-insulating GaAs substrate. The ratio of the luminescence intensities of two different magneto-exciton peaks is used as temperature indicator. As the quantum well is pumped with high laser intensity, the ratio of luminescence intensity from the magneto-exciton lines (hh(2s) to lh(1s)) drops. This is interpreted as local laser cooling by an amount ΔT = -6 K. Their results is reproduced in Fig.1.5.

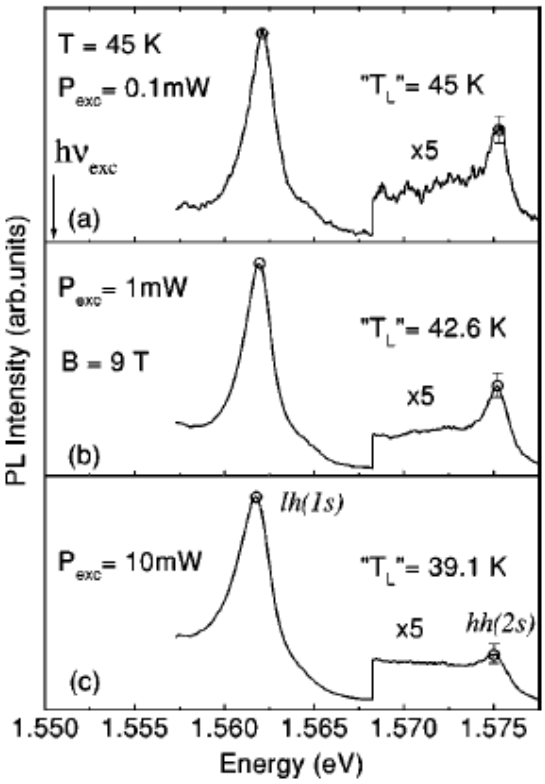

Fig.1.5. local cooling results claimed by Finkeißen *el al*. [42] Up-converted luminescence at a bath temperature of 45 K in a magnetic field of 9 T for three different excitation powers: (a) 0.1, (b) 1, and (c) 10 mW. The excitation energy was at the hh(1s), marked by the arrow. Circles: intensities deduced from a Maxwell distribution yielding a temperature T_L (error bars correspond to ±1.5 K).

Their result is surprising because with the GaAs substrate still attached to the quantum well, the vast majority of the pump laser power is deposited in the thick substrate of the device, converting to heat. The proximity of the substrate to the wells will swamp out any local cooling that may exist there. Luminescence from the quantum wells will be largely trapped by total internal reflection and re-absorbed in the substrate, which adds to the heat load on the wells. The temperature gradient between quantum wells and the cryostat is estimated and the result shows their deduced temperature decrease of ΔT = 6 K does not appear to be possible in this setup [49].

Upon careful investigation, it was found that their interpretation of local cooling was flawed because the high carrier density generated by the pump laser will affect the magneto-exciton spectra and distort the luminescence thermometry measurements they used [50]. Coulomb screening of the magneto-exciton binding potential can occur at sufficiently high carrier density and the luminescence intensity of high energy excitons will drop. Simulation shows that the exciton spectra might change in the manner observed without a temperature decrease (See Fig.1.6) [50].

The main conclusion is that using a single laser to both pump the sample and monitor temperature may lead to ambiguity in semiconductor cooling experiments. The excite-probe thermometry technique that we developed (covered in detail in Chapter 4) can avoid their mistake.

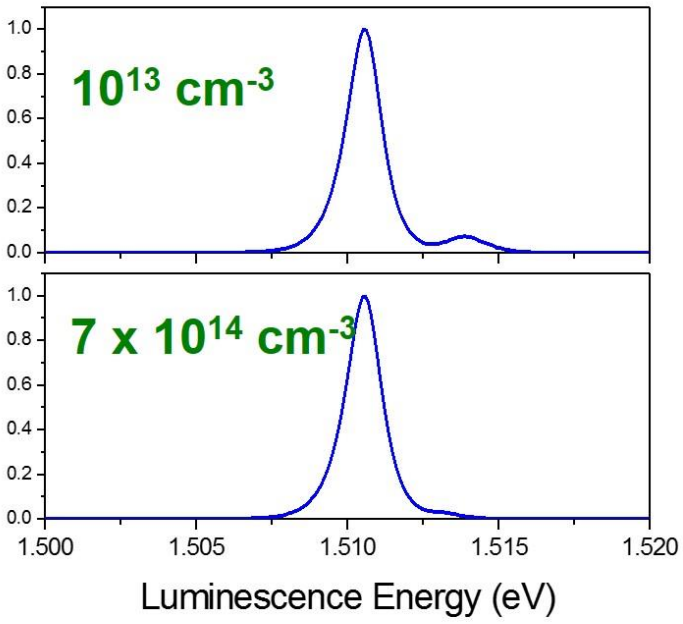

Fig.1.6. Calculated exciton contribution to luminescence in 3-D GaAs at 50 K. Peaks have been normalized and luminescence from the continuum is removed [50].

Researchers at the University of New Mexico improved and developed Gauck's method and measured the external quantum efficiency (EQE) in a InGaP/GaAs/InGaP double heterostructure (DHS) Van der Waals bonded to a ZnS hemisphere lens with high precision [44, 46]. They obtained a record EQE of 99.5% in bulk GaAs DHS semiconductor [47]. However, net cooling was still not achieved due to high parasitic background absorption. This work is the main topic of this Dissertation.

Recently, a group led by Xiong at Nanyang Technological University in Singapore demonstrated a net laser cooling in II-VI semiconductor cadmium sulfide (CdS) nanobelts (shown in Fig.1.7) by ~40K from room temperature by a 514nm laser, and by ~15K from 100K when pumped by a 532-nm laser [48].

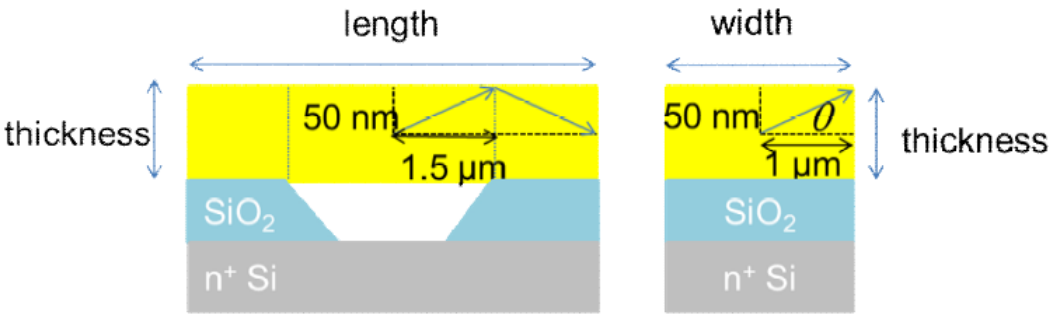

Fig.1.7. The side view (left) and front view (right) of the CdS nanobelt. The width and the thickness are 2 μm and 100 nm, respectively. The length is about 10 μm. The dimensions are not drawn to scale in the above schematic diagram.

The CdS nanobelts are suspended on a SiO_2/Si substrate and the laser cooling demonstration was conducted on the suspended segment. The size of the beam spot on the sample is ~2×2 μm^2. In cooling experiments, in order to accurately detect the local temperature of the sample, only the fluorescence emitted from a ~0.4×0.4 μm^2 area at the center of the laser spot was measured by adjusting the confocal pinhole to~40 ×40 μm^2.

They use a time-gated pump-probe luminescence thermometry (PPLT) technique to measure the laser cooling with set-up and time sequences as shown in Fig.1.8. The idea is very similar to the differential luminescence thermometry (DLT), which will be covered in detail in Chapter 4. Their experimental cooling results are reproduced in Fig.1.9 [48].

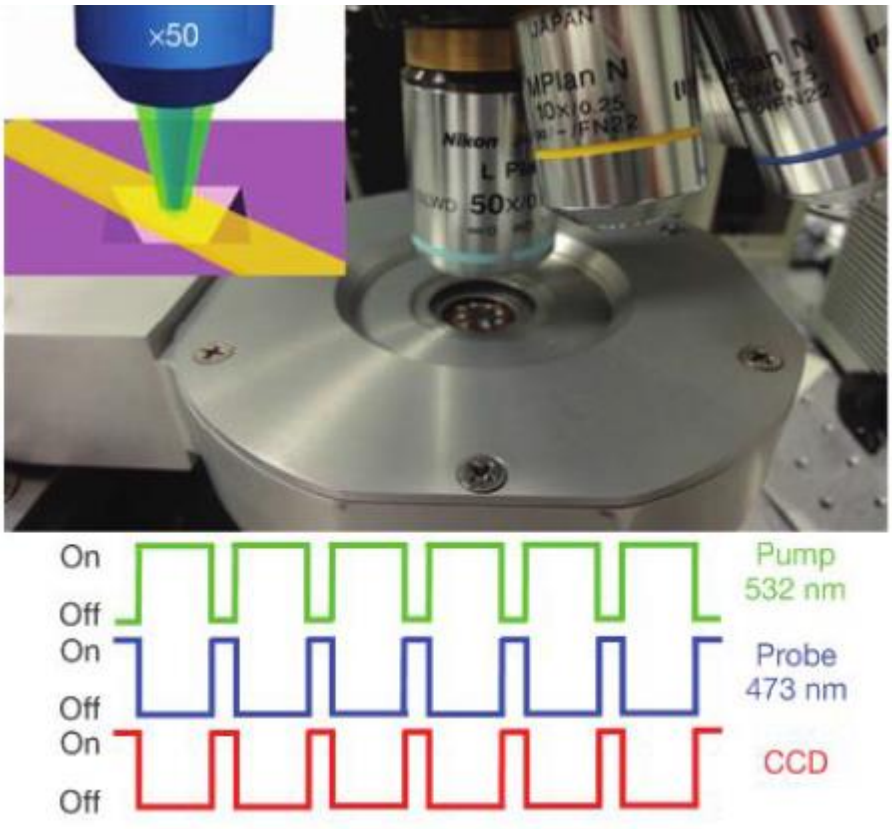

Fig.1.8. (Top) Measurement set-up with two laser beams (pump and probe) aligned on the same spot. (Below) Time sequence of the PPLT. After every 5 min of pumping, the pump laser was blocked momentarily and the probe PL spectrum was acquired immediately, excited by a 20 μW, 473-nm laser, and collected by a CCD.

They attribute the net laser cooling in CdS to strong coupling between excitons and longitudinal optical phonons (LOPs), which allows the resonant annihilation of multiple LOPs in luminescence up-conversion processes, high external quantum efficiency and negligible background absorption. Compared with GaAs, CdS has a much smaller surface recombination velocity [51] and a much lower Auger non-radiative recombination coefficient, owing to the larger bandgap [49]. In addition, the luminescence extraction efficiency approaches unity as a result of the subwavelength

thickness of the nanobelt. All these factors results a very high EQE in the CdS nanobelt system.

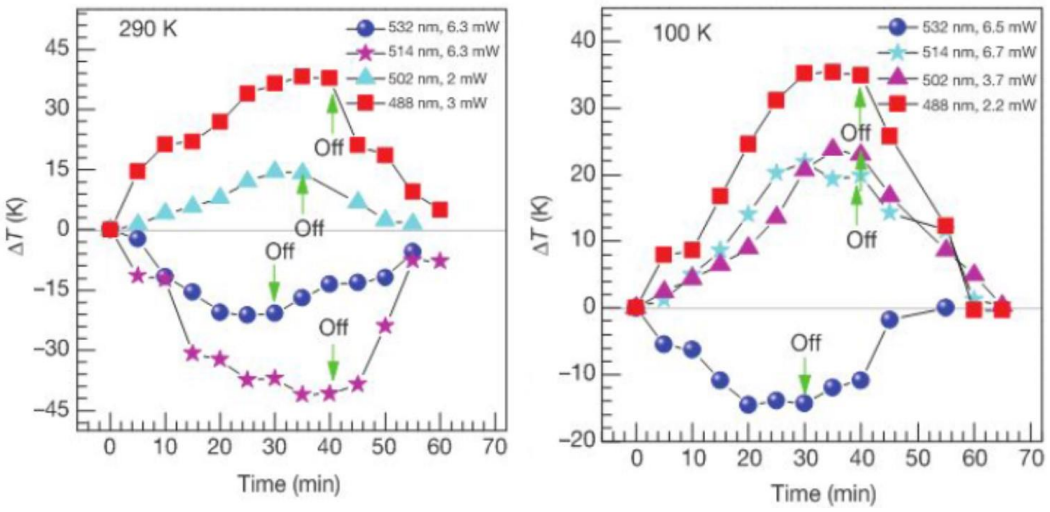

(a) (b)

Fig.1.9. Net laser cooling of CdS nanobelts. Temperature change, ΔT, versus time pumped by four laser lines (532,514,502 and 488 nm), using data extracted from photo luminescence spectra and corresponding calibration curve around (a) 290K. (b) 100K

This work is the first demonstration of net laser cooling in semiconductors. Though more understanding is needed for their cooling results, their work opens the way to future design of material for laser cooling in semiconductors. It would be an immediate advance to test other II-VI materials in the single-crystal, thin-film structures for laser cooling.

1.4 Summary

In this dissertation, the prospects for laser cooling in III-V compound semiconductors are theoretically and experimentally investigated. The various engineering obstacles are identified and solutions to overcome them are described. A detailed description of precise characterization for the GaAs double heterostructure (DHS) for laser cooling in semiconductors are presented. This characterization technique is universal and can also be applied to other semiconductor materials.

In Chapter 2, the cooling process in bulk intrinsic direct bandgap semiconductors is investigated theoretically. The external quantum efficiency (EQE) and cooling conditions are derived. Chapter 3 is dedicated to detailed device fabrication procedures for laser cooling samples with various designs. The precise characterization of semiconductor parameters and laser cooling experiments with GaAs are presented in Chapter 4. A new non-contact, high resolution temperature measurement scheme is developed and implemented. In Chapter 5, Power-dependent photo-luminescence (PDPL) technique is developed that allow us to rapidly screen the semiconductor cooling samples before device fabrication. Chapter 6 discusses the observation of lateral lasing in GaAs DHS and multiple quantum well (MQW) samples and shows that the phenomenon can be explained by the effect of bandgap renormalization due to Coulomb screening. The concluding chapter summarizes the results and outlines future improvements that would allow the observation of net laser cooling in III-V compound semiconductors.

Chapter 2

Fundamentals of Laser Cooling in Semiconductors

2.1 Overview

Laser cooling cycle in a two-level system has been introduced in Chapter 1 and is again shown in Fig.2.1. In this simple model, the interaction rate between electrons and phonons within each manifold is assumed to be far faster than the spontaneous emission rate, which is valid for a broad range of materials and temperatures.

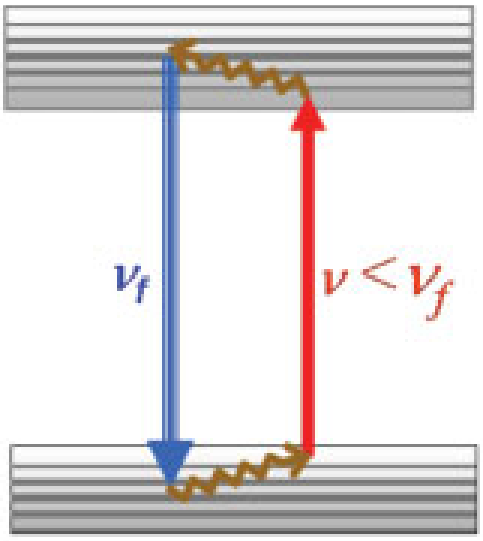

Fig.2.1. The laser cooling cycle in a solid. The light source of frequency $h\nu$ excites atoms near the top of the ground state to the bottom of the excited state. Radiative decays occurring after thermalization emit photons with average energy $h\nu_f > h\nu$.

The cooling efficiency or fractional cooling energy for each photon absorbed is:

$$\eta_c = \frac{h\nu_f - h\nu}{h\nu} = \frac{\lambda - \lambda_f}{\lambda_f} \tag{2.1}$$

where $\lambda=c/\nu$ and $\lambda_f=c/\nu_f$. This is obtained assuming all the fluorescence light is dumped in a heat sink and thus wasted. If, however, the escaping light is captured by a photovoltaic device to recycle this energy, the ultimate cooling efficiency can approach the Carnot limit [5].

Eq. (2.1) indicates that the cooling efficiency can be made arbitrary large by selecting $h\nu \ll h\nu_f$ (i.e. $\lambda \gg \lambda_f$). Practical considerations, however, dictate that $\Delta h\nu = h\nu_f - h\nu$ be of the order of the thermal energy k_BT. This is imposed, as will be discussed in more detail later, by vanishing optical absorption as $h\nu \ll h\nu_f$ as well as the presence of parasitic background absorption. The cooling efficiency is then approximated by a more practical limit:

$$\eta_c \approx \frac{k_BT}{E_g} \tag{2.2}$$

where the approximation $h\nu_f \approx E_g$, the bandgap energy of the semiconductor, has been made.

There are additional complications that reduce the cooling efficiency of a real device defined in Eq. (2.2). Some of the optical excitations decay via non-radiative or heat-producing channels. Internal quantum efficiency is defined as the ratio of the radiative recombination to the sum of the radiative plus non-radiative recombination:

$$\eta_{\text{int}} = \frac{W_r}{W_r + W_{nr}} \tag{2.3}$$

Not all the luminescing photons escape from the cooling device; this is quantified with an extraction or escape efficiency coefficient η_e.

This defines the external quantum efficiency η_{ext}, or EQE in which η_e modifies the internal quantum efficiency as follows: (derivation is given later in this Chapter)

$$\eta_{ext} = \frac{\eta_e W_r}{\eta_e W_r + W_{nr}} \approx \eta_{\text{int}}^{\frac{1}{\eta_e}} \tag{2.4}$$

In an ideal system, both the internal and external quantum efficiency are unity. This condition can never be achieved in practice, hence deleterious heating of the sample occurs. If the internal and external quantum efficiency are not well managed, this heating can overwhelm the laser cooling process.

Accounting for the external quantum efficiency, the cooling efficiency is modified as follows: (derivation will be given later in this Chapter)

$$\eta_c = \eta_{ext} \frac{\nu_f}{\nu} - 1 \tag{2.5}$$

An important operational consideration is that all the incident laser power may not be absorbed in the desired state. The presence of background absorption leads to a resonance absorption efficiency, defined as:

$$\eta_{abs} = \frac{\alpha(\nu)}{\alpha(\nu) + \alpha_b} \tag{2.6}$$

where $\alpha(\nu)$ is the resonant absorption and α_b is the parasitic background absorption, which is assumed to be wavelength independent. When the situation of non-ideal absorption exists ($\eta_{abs} < 1$), the cooling efficiency is further modified to:

$$\eta_c = \eta_{abs}\eta_{ext} \frac{\nu_f}{\nu} - 1 \tag{2.7}$$

The derivation of Eq. (2.7) will be given later. Net cooling is attained with the condition: $\eta_c > 0$. Taking $h\nu_f - h\nu \approx k_B T$, this leads to

$$\eta_{abs}\eta_{ext} > 1 - \frac{k_B T}{E_g} \tag{2.8}$$

The expressions and discussions above are general and can be applied to both rare-earth doped solids and semiconductors.

2.2 Laser cooling model for semiconductors

The essential difference between semiconductors and RE-doped materials is in their cooling cycles. In the latter, the cooling transition occurs in localized donor ions within the host material while the former involves transition between extended valence and conduction bands of a direct gap semiconductor (see Fig.2.2).

The laser cooling model for semiconductors, which is introduced below, mainly follows Ref [5, 30]. We consider an intrinsic (undoped) semiconductor system uniformly irradiated with a laser light at photon energy $h\nu$. Furthermore, we assume that only a fraction η_e of the total luminescence can escape the material while the remaining fraction ($1-\eta_e$) is trapped and re-cycled, thus contributing to carrier generation. For now, we will ignore the parasitic absorption of luminescence but will later consider its implications. For a given temperature, the rate equations for the electron-hole pair density (N) is given by [30]:

$$\frac{dN}{dt} = \frac{\alpha I}{h\nu} - aN - BN^2 - CN^3 + (1-\eta_e)BN^2 \tag{2.9}$$

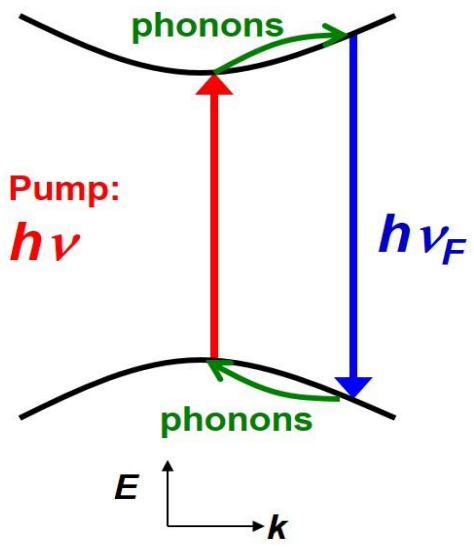

Fig.2.2. Cooling cycle in laser refrigeration of a semiconductor in which absorption of laser photons with energy $h\nu$ creates a cold distribution of electron-hole carriers. The carriers then heat up by absorbing phonons followed by an up-converted luminescence at $h\nu_f$.

Here $\alpha(\nu)$ is the interband absorption coefficient. I is the incident laser irradiance. The recombination process consists of non-radiative (AN), radiative (BN^2), and Auger (CN^3) rates. All the above coefficients are temperature dependent. Ref [49] gives a detailed discussion of the three recombination processes in semiconductors. The last term represents the increase in N from the re-absorption of the luminescence that does not escape, assuming the re-absorption occurs within the laser excitation volume.

Under steady-state conditions, Eq. (2.9) can be rewritten as:

$$0 = \frac{\alpha(\nu)I}{h\nu} - aN - \eta_e BN^2 - CN^3 \tag{2.10}$$

This indicates that the fluorescence trapping effectively inhibits the spontaneous emission as it appears through $\eta_e B$ only. This result has also been shown previously by Asbeck [52].

It is important to note that η_e is itself an averaged quantity over the entire luminescence spectrum.

$$\eta_e = \frac{\int S(\nu)R(\nu)d\nu}{\int R(\nu)d\nu} \tag{2.11}$$

Here *S(ν)* is the geometry-dependent escape probability of photons with energy *hν* and *R(ν)* is the luminescence spectral density that is related to the absorption coefficient through reciprocity using a "non-equilibrium" van Roosbroeck-Shockley relation (also known as Kubo-Martin-Schwinger (KMS) relation [53]:

$$R(\nu, N) = \frac{8\pi n^2 \nu^2}{c^2}\alpha(\nu)\left\{\frac{f_c(1-f_v)}{f_v - f_c}\right\} \tag{2.12}$$

where c is the speed of light and n is the index of refraction. $f_{v,c}$ are Fermi-Dirac distribution functions for the valence and conduction bands.

2.2.1 Cooling power density and cooling efficiency in semiconductors

The net power density that is deposited in the semiconductor is the difference between the power absorbed from the laser (P_{abs}) and that of the luminescence that escapes (P_{le}):

$$P_{net} = P_{abs} - P_{le} = [\alpha I + \Delta P] - [\eta_e B N^2 h\tilde{\nu}_f] \tag{2.13}$$

where the absorbed power density includes the resonant absorption (αI) and a term ΔP that accounts for the undesirable effects such as free-carrier absorption and other parasitic absorptive processes. The second term is the escaped luminescence power density at a mean luminescence energy $h\tilde{\nu}_f$ defined as:

$$h\tilde{\nu}_f = \frac{\int S(\nu)R(\nu)h\nu d\nu}{\int S(\nu)R(\nu)d\nu} \tag{2.14}$$

Note that the escaped mean luminescence energy can deviate (i.e. redshift) from its internal value (*S=1*) depending on the thickness or photon recycling conditions. With the aid of Eq. (2.10), we rewrite Eq. (2.13) as:

$$P_{net} = \eta_e BN^2(h\nu - h\tilde{\nu}_f) + ANh\nu + CN^3h\nu + \Delta P \tag{2.15}$$

Eq. (15) rigorously describes laser cooling of a semiconductor in a compact and simple form. It accounts for the practical considerations of luminescence trapping by introducing an inhibited radiative recombination ($\eta_e B$) and a shifted mean photon energy $h\tilde{\nu}_f$ for the escaped luminescence. For high external efficiency systems where *S(v) = 1*, Eq. (2.15) approaches that described in the literature with $\eta_e = 1$ and $h\tilde{\nu}_f = h\nu_f$ with ν_f denoting the mean fluorescence energy produced internally in the semiconductor.

The cooling efficiency η_c is defined as the ratio of cooling power density $Pc(=-P_{net})$ to the absorbed laser power density ($P_{abs} = \alpha I + \Delta P$). With the aid of Eq. (2.10), this efficiency can be expressed as:

$$\eta_c = \frac{\eta_e BN^2(h\nu - h\tilde{\nu}_f) + ANh\nu + CN^3h\nu + \Delta P}{\eta_e BN^2h\nu + ANh\nu + CN^3h\nu + \Delta P} \tag{2.16}$$

Ignoring the ΔP contributions for the moment, η_c can be written more simply as:

$$\eta_c = \eta_{ext}\frac{\tilde{\nu}_f}{\nu} - 1 \tag{2.17}$$

where η_{ext} describes the external quantum efficiency (or EQE):

$$\eta_{ext} = \frac{\eta_e B N^2}{AN + \eta_e B N^2 + CN^3} \tag{2.18}$$

The external quantum efficiency can be cast in terms of the internal quantum efficiency (η_{int}):

$$\begin{aligned} \eta_{ext} &= \frac{\eta_e B N^2}{AN + \eta_e B N^2 + CN^3} = \frac{1}{1 + \frac{AN + CN^3}{\eta_e B N^2}} \approx 1 - \frac{AN + CN^3}{\eta_e B N^2} \\ &\approx \left(1 - \frac{AN + CN^3}{BN^2}\right)^{\frac{1}{\eta_e}} \approx \left(\frac{1}{1 + \frac{AN + CN^3}{BN^2}}\right)^{\frac{1}{\eta_e}} = \eta_{\text{int}}^{\frac{1}{\eta_e}} \end{aligned} \tag{2.19}$$

where the binomial theorem is used to make the approximation with the realistic assumption that η_{ext} is near unity (>0.9). The term $1/\eta_e$ approximately denotes the number of luminescence recycling before it has a chance to couple out of the material.

One simple consequence of Eq. (2.18) is that there is an optimum carrier density $N^{opt} = (A/C)^{1/2}$ at which η_{ext} reaches a maximum:

$$\eta_{ext}^{\ opt} \approx 1 - \frac{2\sqrt{AC}}{\eta_e B} \tag{2.20}$$

The density-dependent EQE will be discussed in detail in Chapter 4 and 5.

Including background parasitic absorption ($\Delta P = \alpha_b I$) results in a more general form of cooling efficiency:

$$\eta_c = \eta_{abs}\eta_{ext}\frac{\tilde{\nu}_f}{\nu} - 1 \tag{2.21}$$

where the absorption efficiency η_{abs} is the fraction of the total absorbed photons from the pump laser that is consumed by the resonant absorption in the cooling region defined as:

$$\eta_{abs} = \frac{\alpha(\nu)}{\alpha(\nu) + \alpha_b} \tag{2.22}$$

where α_b denotes an effective background parasitic absorption coefficient and is assumed to be constant in the vicinity of the band-edge region.

2.2.2 Parasitic absorption of luminescence

If the pump laser suffers parasitic absorption, so will the luminescence since their frequencies are very close. We now examine the parasitic absorption problem and its effect on the cooling efficiency by revisiting Eq. (2.9). A small fraction ε_f of the trapped luminescence is absorbed parasitically and the remaining part (1-ε_f) is recycled through interband absorption thus contributing to the carrier generation.

Eq. (2.9) is rewritten as:

$$\frac{dN}{dt} = \frac{\alpha I}{h\nu} - aN - BN^2 - CN^3 + (1-\eta_e)(1-\varepsilon_f)BN^2 \tag{2.23}$$

Note that $1-\varepsilon_f = \bar{\alpha}_f / (\bar{\alpha}_f + \alpha_b) \approx 1 - \alpha_b / \bar{\alpha}_f$ where $\bar{\alpha}_f (\approx \alpha(\nu_f))$ is the interband absorption of the luminescence averaged over its spectrum. Following the same analysis leading to Eq. (2.21), we obtain the modified cooling efficiency:

$$\eta_c = \eta_{abs}\bar{\eta}_{ext}\frac{\tilde{\nu}_f}{\nu} - 1 \tag{2.24}$$

with a modified EQE ($\bar{\eta}_{ext}$) that is reduced from its ideal value in the high purity ($\alpha_b \approx 0$) approximation to:

$$\begin{aligned}\bar{\eta}_{ext} &= \eta_{ext}\frac{1}{1+\eta_{ext}\varepsilon_f(1-\eta_e)/\eta_e} \\ &\approx \eta_{ext} - {\eta_{ext}}^2\varepsilon_f(1-\eta_e)/\eta_e\end{aligned} \tag{2.25}$$

2.2.3 Free carrier absorption

Earlier in this section, free carrier absorption was ignored. Here, the effect of free carrier absorption on P_{net} and η_{ext} is estimated. The free carrier absorption is a source of heating in the active cooling layer. Free carries in the valence and conduction bands can interact with photons and make a transition to higher states within the bands.

Free carrier absorption is wavelength-dependent [54] and important for photons with energies less than semiconductor bandgap energy [55]. Free carrier absorption is often written with a cross section σ_{fca} [53, 54, 56]:

$$\alpha_{fca} = \sigma_{fca}N \tag{2.26}$$

The absorption power density due to free carrier absorption is $\sigma_{fca}NI$. Following Eq. (2.10), and assuming the radiative term dominates,

$$I \approx \frac{h\nu}{\alpha(\nu)}\eta_e BN^2 \tag{2.27}$$

This approximation defines the free carrier absorption power density P_{fca} as:

$$P_{fca} \approx \left(\frac{\eta_e B \sigma_{fca}}{\alpha(\nu)} \right) h\nu N^3 \tag{2.28}$$

Note that P_{fca} scales as N^3, which is the same as Auger recombination contribution to Eq. (2.15). This means the Auger recombination rate is effectively changed to a modified term *C'*:

$$C' \approx C + \frac{\eta_e B \sigma_{fca}}{\alpha} \tag{2.29}$$

The effect of free carrier absorption on external quantum efficiency in Eq. (2.18) can be approximated by replacing C with C'.

2.2.4 Cooling conditions and numerical estimates

The condition $P_{net} = 0$ occurs when cooling and heating are in balance. Eq. (2.15) shows P_{net} as a second order polynomial in *N*, so the roots define the carrier density range within which net cooling can be observed provided that $\eta_e B(h\tilde{\nu}_f - h\nu) \geq 2h\nu\sqrt{AC}$. Take $\Delta P = \alpha_b I + \sigma_{fca} N I$ and solve Eq. (2.15) using Eq. (2.27), we have:

$$N_{1,2} = \sqrt{\frac{A_0}{C'}} \left(1 \mp \sqrt{1 - \frac{A}{A_0}} \right) \tag{2.30}$$

where

$$A_0 = \left(\frac{h\tilde{\nu}_f - h\nu}{h\nu} - \frac{\alpha_b}{\alpha(\nu)} \right)^2 \frac{(\eta_e B)^2}{4C'} \tag{2.31}$$

is the break-even (maximum allowable) non-radiative decay rate for a given excitation energy *hν*. The minimum non-radiative lifetime is $\tau_0 = 1/A_0$.

Generating an e-h population density less than N_1 makes bulk and surface non-radiative recombination prevalent. On the other hand, generating carrier densities larger than N_2 makes non-radiative Auger dominant. Only in a range of densities between N_1 and N_2 in which radiative recombination is dominant can net laser cooling be expected.

In other words, net cooling can occur within an irradiance range of $I_1 < I < I_2$ where

$$I_{1,2} \approx \left(h\nu\eta_e B / \alpha(\nu)\right) N_{1,2} \tag{2.32}$$

The parameters B and C are fundamental properties of a semiconductor and have been calculated and measured extensively for various bulk and quantum-confined structures [53, 54, 57, 58]. The reported values for these coefficients, however, vary considerably. In bulk GaAs, for example, the published values are $2\times10^{-16} < B < 7\times10^{-16}$ m^3/s and $1\times10^{-42} < C < 7\times10^{-42}$ m^6/s [58]. These variations are primarily due to experimental uncertainties. We assume average values of $B = 4\times10^{-16}$ m^3/s and $C = 4 \times 10^{-42}$ m^6/s, while ignoring the effects of background and free carrier absorption. These assumptions allow us to gain insight into the feasibility and requirements for achieving net laser cooling.

Recently, it was found that free carrier absorption (FCA) at the band edge wavelengths is much smaller than previously expected [59, 60]. For GaAs, $\sigma_{fca} \approx 10^{-24}$ m^2 [59, 60], which requires $\alpha(\nu) \geq 10^3$ m^{-1} to ensure that free carrier losses are negligible (i.e. $C' \approx C$). This requirement is satisfied even at $\lambda = 890$nm (corresponding to $h\nu_f - h\nu \approx 2k_BT$) where $\alpha(\nu) \approx 10^4$ m^{-1}. We conclude that FCA does not pose a limitation on laser cooling.

Using Eq. (2.31), we plot in Fig. 2.3 the break-even non-radiative lifetime τ_0 as a function of η_e assuming $h\nu_f - h\nu = k_B T$ with $h\nu_f$ corresponding to $\lambda_f \approx 860$ nm at room temperature.

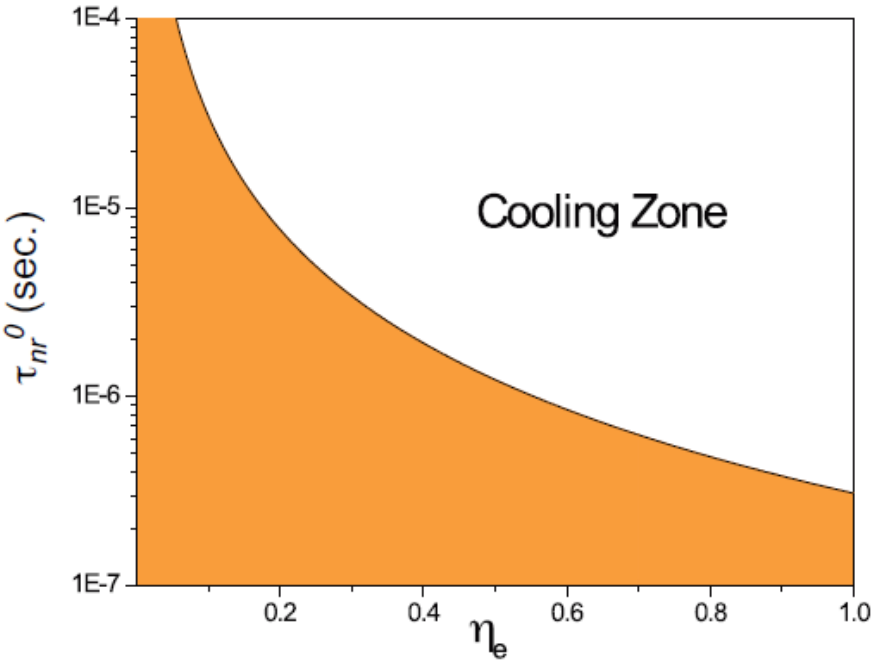

Fig.2.3. The break-even non-radiative lifetime as a function of the luminescence extraction efficiency in bulk GaAs calculated using typical values of radiative and Auger recombination at room temperature.

The orange area under the curve is the unwanted (heating) zone. Eq. (2.31) also suggests that decreasing the incident photon energy (e.g. at $h\nu_f - h\nu > k_B T$) relaxes this requirement. However, interband absorption drops rapidly as the excitation moves further in the Urbach tail and one may no longer ignore the background absorption. In the analysis in this Chapter, the background absorption is assumed to be in the active material. But in practice, it can also come from the passivation layer or from the interface. The investigation of the sources of background absorption experimentally is covered in Chapter 4.

The presence of band tailing in semiconductors is important in the laser cooling process. There are different phenomena that can explain the presence of band tailing in semiconductors: a) the Franz-Keldysh effect, b) excitonic effects, and c) phonon-assisted transitions d) the presence mid-gap levels due to impurities and imperfections in the crystal structure. A detailed discussion of these processes can be found in Ref [49].

To analyze the limitations of laser cooling imposed by background absorption, an alternate approach to study the break-even condition from cooling efficiency defined in Eq. (2.24) is used. The advantage here is that external quantum efficiency (η_{ext}) is related to cooling efficiency (η_c) in a straightforward manner. Net cooling happens when $\eta_c>0$. Rearranging this equation gives:

$$\eta_{abs}\eta_{ext} > \frac{h\nu}{h\tilde{\nu}_f} \tag{2.33}$$

Thus

$$\eta_{ext} > \frac{h\nu}{h\tilde{\nu}_f \eta_{abs}} \approx \frac{h\nu}{h\tilde{\nu}_f} + \frac{\alpha_b}{\alpha(\nu)} \tag{2.34}$$

A practical cooler will have the removed energy quantum $h\tilde{\nu}_f - h\nu$ of the order of the thermal energy k_BT. Applying this to Eq. (2.34) leads to the following estimate:

$$\eta_{ext} > 1 - \frac{k_BT}{h\tilde{\nu}_f} + \frac{\alpha_b}{\alpha(\nu)} \tag{2.35}$$

The above inequality emphasizes the critical role of α_b in achieving net laser cooling. The quantity η_{ext} can be measured accurately, so Eq. (2.34) defines the minimum value of EQE for a given background absorption provided $\alpha(\nu)$ is known. The absorption $\alpha(\nu)$ drops sharply for energies considerably below the bandgap, which

means this inequality may never be satisfied for any wavelength if α_b is too large. To quantify this argument, we need to know the band-tail absorption accurately. Starting with the measured low-density photoluminescence (PL) spectrum on a high quality sample, we obtain absorption spectra $\alpha(v)$ using the KMS relations of Eq. (2.12).

Using Eq. (2.34), the minimum required η_{ext} can be estimated as a function of hv for various values of α_b, as depicted in Fig.2.4. Here we assume an extraction efficiency η_e=0.1 which is typical of GaAs on a ZnS dome structure [30, 49].

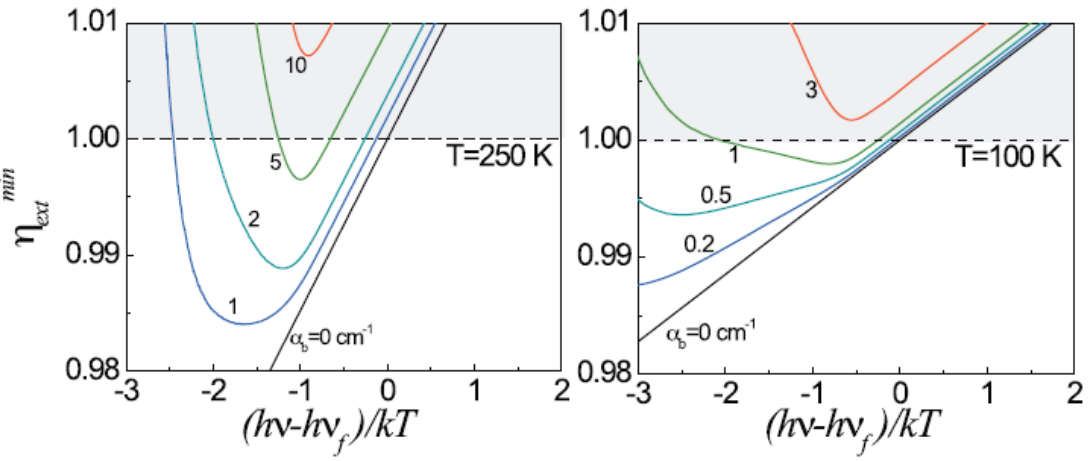

Fig.2.4. Minimum EQE required to achieve laser cooling versus the normalized excitation photon energy for GaAs at T=250 and 100K obtained from the inequality of Eq. (2.34). Note that for certain background absorption α_b, the requirement $\eta_{ext} > 1$ is unattainable (unphysical) for any wavelength. This restriction becomes more prevalent at lower temperature.

2.2.5 Laser cooling of semiconductors at low temperatures

Fig.2.4 indicates that the required EQE for cooling becomes more demanding as the temperature is lowered which is essentially a consequence of diminishing phonon

population at low temperatures. This result mirrors the situation in the rare-earth doped materials. Semiconductors, however, have the fortunate property that their EQE increases with decreasing temperature. The loss terms (*A* and *C* coefficients) decrease while the radiative rate (*B* coefficient) increases inversely with lattice temperature. Using the accepted scaling for $C(T) \propto exp(-\beta(300/T-1))$ with $\beta \approx 2.4$ for GaAs [44, 61], taking $B \propto T^{-3/2}$ [53, 62], keeping $h\tilde{\nu}_f / h\nu - 1 \approx k_B T / E_g$, and ignoring parasitic losses and the small temperature dependence of the band-gap energy, we obtain for the break-even non-radiative decay rate:

$$\frac{A_0(T)}{A_0(300)} \approx \left(\frac{300}{T}\right) \exp\left(\frac{\beta(300-T)}{T}\right) \tag{2.36}$$

At T = 150 K, for example, the break-even lifetime is lowered by ~40 times compared with the room temperature (T = 300 K) condition.

The material-dependent break-even optimum external quantum efficiency for cooling is obtained by combining Eq. (2.20) and Eq. (2.35) as:

$$\eta_{ext}^{\ opt} \approx 1 - 2\sqrt{A(300)C(300)} / \eta_e B(300) > 1 - k_B T / E_g \tag{2.37}$$

where the background absorption is assumed to be negligible. When temperature is included, the break-even external quantum efficiency at optimum carrier density becomes:

$$\begin{aligned} \eta_{ext}^{\ opt} &\approx 1 - 2\frac{\sqrt{A(300)C(300)}}{\eta_e B(300)} \left\{ \left(\frac{T}{300}\right)^{3/2} \exp\left[\frac{1}{2}\left(\frac{E_a}{0.026} + \beta\right)\left(1 - \frac{300}{T}\right)\right]\right\} \\ &> 1 - \frac{k_B T}{E_g(T)} \end{aligned} \tag{2.38}$$

which is derived from the known temperature scaling of radiative, Auger, and non-radiative recombination coefficients. This is visualized by plotting η_{ext} versus T as is

shown in Fig.2.5 for two values of η_e. This range of values of η_e corresponds to a GaAs structure bonded to a high refractive index dome of ZnS or ZnSe [30, 49]. The solid line indicates the break-even condition described by Eq. (2.38). This condition together with the fact that A (typically dominated by surface recombination) increases with temperature [62-64], makes the low temperature observation of laser cooling more favorable even though the overall efficiency ($\approx k_B T/E_g$) decreases. The plot shows that cooling is achievable below 200 K for a sample with η_e=0.2. The reduction in cooling efficiency is effectively due to the reduction of the electron-phonon absorption probability at lower temperatures.

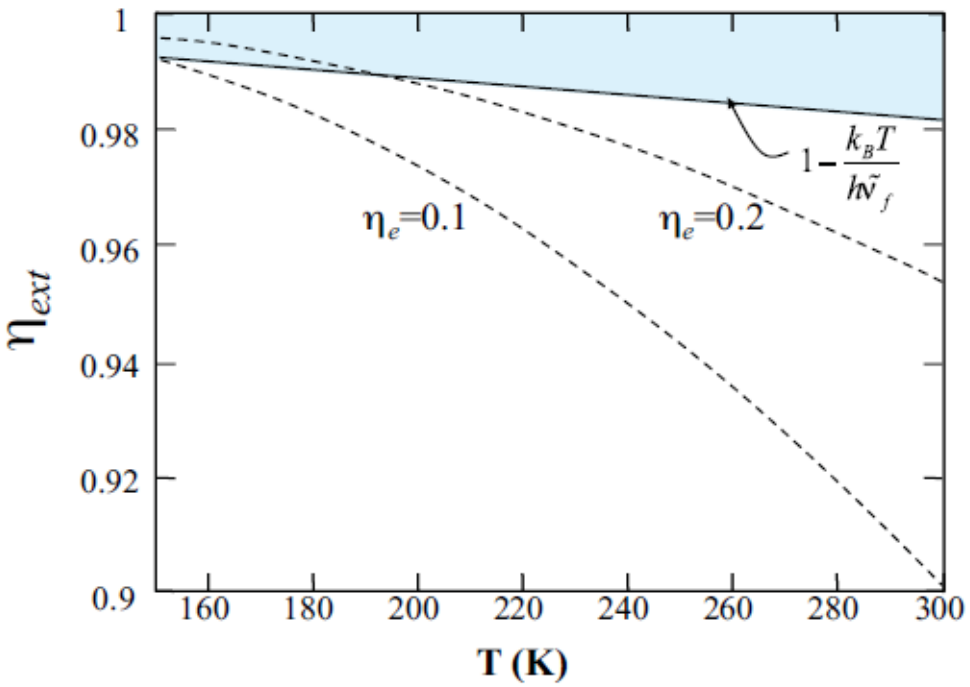

Fig.2.5. The required external quantum efficiency (EQE) as a function of temperature for GaAs under typical parameters.

2.2.6 Electron-phonon scattering

In the laser cooling process, electrons are excited from the top of the valence band to the bottom of the conduction band. The next step in the cycle requires photo carriers to absorb phonons. The temperature-dependent phonon absorption rate can be approximated as [53]:

$$W_{phonon} = W_{LO} + W_{LA} \approx \frac{\gamma}{\exp(\hbar\omega_{LO} / k_B T) - 1} + \sigma T \tag{2.39}$$

where W_{LO} and W_{LA} are scattering rates for optical and acoustic phonons, respectively and $\hbar\omega_{LO}$ is the LO phonon energy. γ and σ are constants for the contribution of optical and acoustic phonons, respectively.

The key message of Eq. (2.39) is that LO phonon absorption becomes disabled at sufficiently small temperatures; weaker acoustic phonon absorption is then required to maintain the laser cooling cycle. Because phonon absorption is a key component of laser cooling, the efficiency of the process is reduced at lower temperatures.

The phonon scattering timescale is of the order of hundreds of femtoseconds to a few picoseconds [53]. In the laser cooling experiment, phonon scattering can be assumed to occur instantaneously except at very low temperatures. In this temperature regime where only acoustic phonon absorption is operative, scattering rate becomes comparable to the radiative recombination rate (BN^2) and consequently cold carrier recombination occurs before complete thermalization with the lattice. This problem is significantly alleviated by employing quantum confined systems where σ is enhanced

by nearly 3 orders of magnitude. Enhanced cooling in quantum confined systems may allow operation at temperatures <10 K [30].

2.2.7 Absorption saturation due to band blocking

Another issue of concern is absorption saturation (band blocking) and many-body interactions. Band-blocking may be a limiting factor for long wavelength excitation where the low density of states gives rise to a stronger bleaching of the interband absorption. It is therefore necessary to have a good understanding of the absorption and emission spectra and its dynamic nonlinearities.

Theoretical models exist that deal with absorption spectra of semiconductor structures under various carrier densities and lattice temperatures [65-68]. Recently, a rigorous microscopic theory for absorption and luminescence in bulk semiconductors that includes the effects of electron-hole (e-h) plasma density as well as excitonic correlations has been introduced under the quasi-thermal equilibrium approximation [27, 31]. Here, we use a simple model to estimate the effect of band-blocking.

In the above discussion, we have assumed the resonant absorption $\alpha(\nu)$ is not dependent on carrier density. The band-to-band resonant absorption in a parabolic structure under low carrier density condition can be derived as [69]:

$$\alpha_0(\nu) = A_{21} \frac{c^2}{8\pi\nu^2 n^2} \rho_{jnt}(\nu) \tag{2.40}$$

where A_{21} is Einstein coefficient, c is speed of light, n is refractive index of the material and

$$\rho_{jnt}(\nu) = \frac{1}{4\pi^2}\left(\frac{2m_r}{\hbar^2}\right)^{3/2}(h\nu - E_g)^{1/2} \tag{2.41}$$

is the joint density of states, where E_g is the band gap energy, $\hbar$ is reduced Planck constant and m_r is the reduced mass expressed by:

$$m_r = \frac{m_e^* m_h^*}{m_e^* + m_h^*} \tag{2.42}$$

where m_e^* and m_h^* is the effective mass for electrons and holes, respectively.

We can lump many of the term onto an ever-present K and write:

$$\alpha_0(\nu) = K(h\nu - E_g)^{1/2} \tag{2.43}$$

The value of K can be determined from experiment.

When a large population density of e-h are generated, the absorption coefficient can no longer be represented by Eq. (2.43). In this case, we have to take into account the probability that the state from which the transition originates is filled multiplied by the probability that the terminal state is empty. Hence the absorption coefficient is proportional to a blocking factor described as:

$$f_v(1-f_c) - f_c(1-f_v) = f_v - f_c \tag{2.44}$$

The first term is for "up" transition probability and second for "down" transition probability. Here f_c and f_v are Fermi-Dirac probabilities of an occupied state in conduction and valence band, given by:

$$f_c = \frac{1}{\exp\left[\left(E_2 - F_n\right)/kT\right]+1} \tag{2.45-a}$$

$$f_v = \frac{1}{\exp\left[\left(E_1 - F_p\right)/kT\right]+1} \tag{2.45-b}$$

where F_n and F_p are quasi Fermi levels for conduction band and valence band, respectively. The optical transition happens between energy level E_1 and E_2, thus E_2-E_1=$h\nu$. The density-dependence absorption coefficient is then expressed as:

$$\alpha(\nu, N) = \alpha_0(\nu)\{f_v - f_c\} \tag{2.46}$$

The absorption $\alpha(\nu,N)$ depends on population density N through the Fermi energy levels F_n and F_p. At low e-h population density, $F_n \approx F_p \approx E_g/2$, thus $f_v \approx 1$ and $f_c \approx 0$, the absorption coefficient is density-independent. At high levels of optical pumping, band blocking occurs and $\{f_v - f_c\}$ approaches zero. This absorption saturation is due to the Pauli exclusion principle.

Using the electron-hole density of states corresponding to a simple two-parabolic band model, we calculate the carrier density at which the blocking factor $\{f_v - f_c\}$ vanishes at $h\nu = h\nu_f - k_B T$. The result is depicted in Fig.2.6 where this blocking density is contrasted with N_1 and N_2 of Eq. (2.30) evaluated using a constant A coefficient, and a temperature dependent B and C coefficient used earlier. It is seen that band-blocking tends to reduce the cooling density window at $T < 200$ K, and that cooling densities become unattainable at $T \approx 10$ K. The simple model overestimates band-blocking effects, but qualitatively agrees with the more rigorous microscopic theory [27, 31].

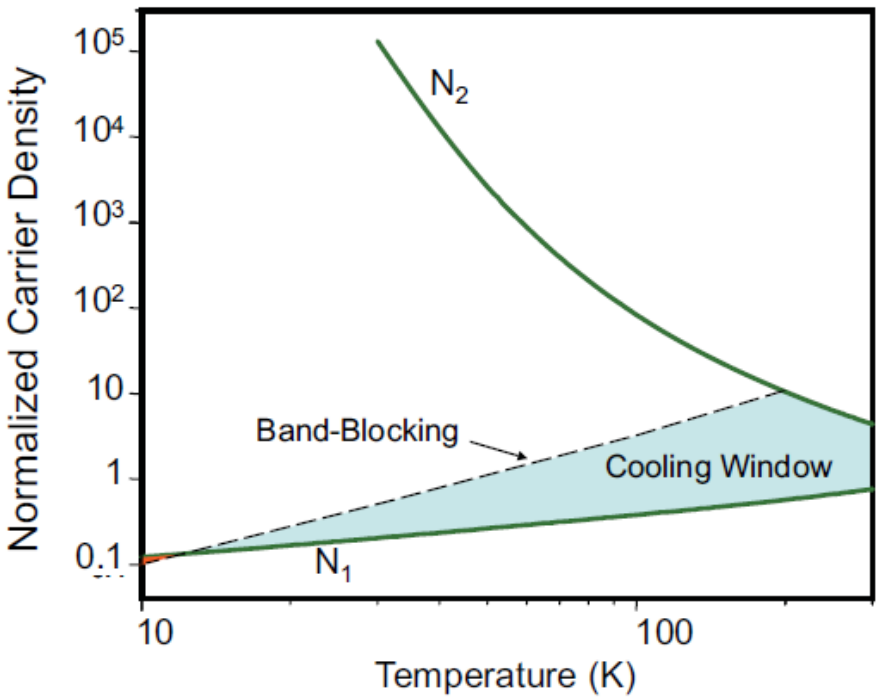

Fig.2.6. The upper carrier density N_2, given by Eq. (2.30) is seen to be unattainable in GaAs due to band-blocking as temperature is lowered below 200 *K*. The middle (dashed) line represents the calculated density at which the band-tail absorption at $h\nu = h\nu_f - k_B T$ completely saturates (i.e. $\alpha(\nu,N)=0$, Eq. (2.46)). This is a worst case scenario for which the non-radiative recombination rate is assumed to be constant with temperature.

Chapter 3

Device Processing and Fabrication

In order to perform the cooling experiment and enhance the luminescence extraction efficiency, the double heterostructure samples (DHS) needs to be removed from the GaAs substrate and bonded to nearly index-matched ZnS or ZnSe hemispheres.

In this chapter, the fabrication of GaInP/GaAs/GaInP double heterostructure sample for laser cooling application is discussed. For samples with release layers, the technique of epitaxial lift-off [70-72] and Van der Waals bonding [73-76] are used. For samples without release layers, the processing involves wet etching of the substrate and Van der Waals bonding.

3.1 Device fabrication for samples with release layers

A schematic of a GaInP/GaAs/GaInP double heterostructure before epitaxial lift-off is shown in Fig.3.1. The thickness of the active layer and passivation layers are optimized [49]. A thin layer (50nm) of AlAs or $Al_{0.98}Ga_{0.02}As$ is grown between the double heterostructure and the substrate as the release layer for lift off.

Samples grown by MBE are provided by Andreas Stintz at Center for High Technology Materials (CHTM) at University of New Mexico (UNM) and samples

grown by MOCVD are provided by Jeffrey Cederberg at Sandia National Laboratory (SNL) and Jerry Olson at National Renewable Energy Laboratory (NREL).

Processing is performed in a cleanroom environment at CHTM (with 100-1000 ratings [1]) to avoid trapping particles in between the double heterostructure and hemisphere lens.

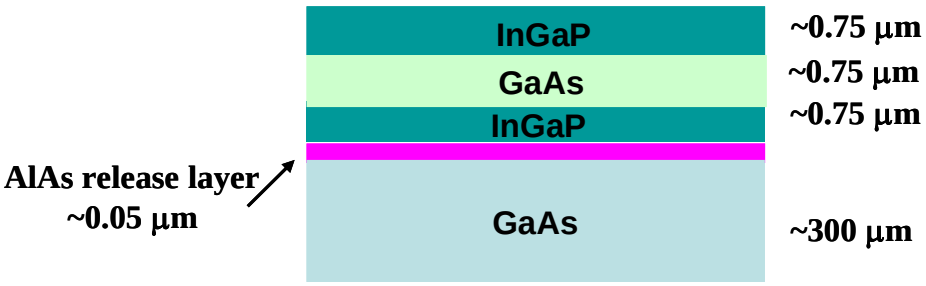

Fig.3.1. Sample structure for laser cooling of semiconductors. An AlAs layer is used to liftoff the sample from the substrate.

3.1.1 Lift-off and bonding without wax support

The procedure of lifting-off and bonding of samples without wax support was first established by Babak Imangholi and ref [49] gives a detailed discussion of this approach. A few improvements have been made recently. The following steps briefly describe the current process of sample fabrication without wax support.

Cleaving. The wafer is cleaved into square pieces of ~7mm×7mm by a cleaver along the crystal axis. This step replaces the dicing procedure used before. Compared

[1] Cleanroom class is defined as number of particles 0.5 micrometer and larger per cubic foot of air; e.g. A Class 10 cleanroom has a maximum of 10 particles per ft^3.

to dicing, cleaving is much simpler to perform and largely avoids the dust produced in the dicing procedure, which will likely to cause scratches on the surface of the sample both during the dicing process and afterwards.

Cleaning. The cleaved pieces are ultrasonically cleaned in DI water and subsequently cleaned on a cleanroom wiper tissue in sequence with acetone, methanol, isopropanol, and DI water followed by nitrogen gas drying.

Photolithography. Before applying photoresist, the sample is pre-baked on a hot-plate at no more than 90 DegC to evaporate any remaining water residue. A few drops of AZ-4620 photoresist is then applied on the surface for patterning. A procedure of ramping the spinner with velocity (nominally 500rpm) up and down at 5s intervals for 30s is required to provide a 5.6μm thick layer of photoresist. The sample is then post-baked on a 90 DegC hot plate for 90s to dry the photoresist solvent.

After photoresist coating, the sample is exposed to ultraviolet (UV) radiation at $\lambda \approx 405$nm through a positive photo-mask. The photo-mask with transparent circular holes will define individual samples after a 19s exposure to high intensity UV light from a mercury lamp. The photo-mask is in near-contact with the surface of the sample. The hole diameter is chosen considering the following factors: i) it must be larger than the laser pump spot size plus the carrier diffusion length. ii) The diameter must be small enough to maintain rigidity to bending and twisting during handling.

To develop the photoresist, the exposed sample is dipped for 2 minutes into a diluted AZ-400 solution and then DI water for 1 minute.

Fig.3.2 shows the side view of the sample after photolithography.

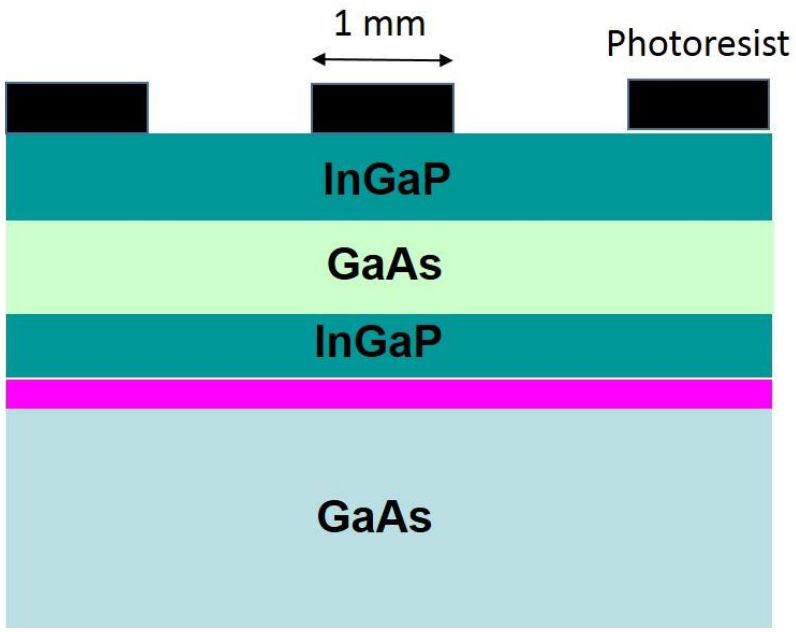

Fig.3.2. Side view illustration depicting the photoresist pattern on the heterostructure.

Etching. The next step is vertical etching using inductively coupled plasma (ICP). The etching rate of AZ-4620 photoresist is negligible compared to bare GaAs or GaInP. The ICP etch rate for GaAs or GaInP is 3μm per 10 min. The rate depends on plasma power, gas flow, and pressure. An etching time for a 1mm disk of ~12 minutes is used to assure of exposing the AlAs release layer (See Fig.3.3 for side view illustration).

Lift off. Lift-off is accomplished by etching the AlAs layer with a 49.2% HF acid solution. The HF solution strongly reacts with AlAs to produce a water soluble salt AlF_3 and a toxic colorless gas AsH_3 [72]. Due to the light weight of the released samples, they often fall back and re-attach to the substrate. This Van der Waals bond is very strong and prevents removal of the disk without destroying it. To overcome this problem, the samples before lift-off are adhered to a piece of Teflon fixture using black

wax in an upside down position (double heterostructure is under the substrate) and then dipped into the HF solution.

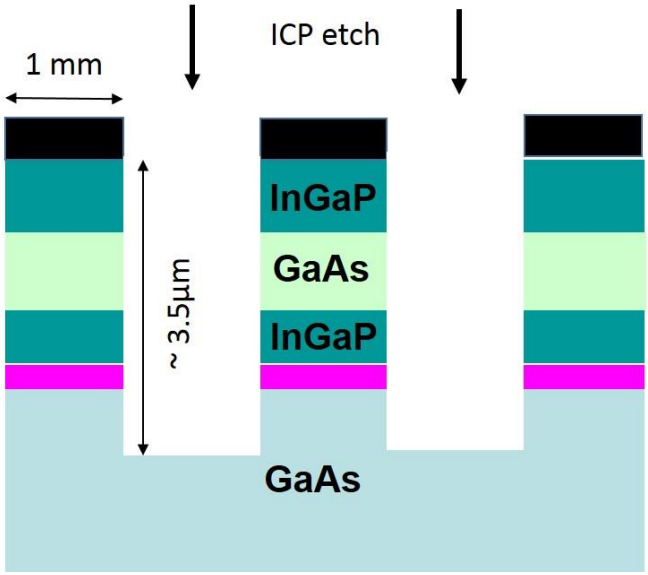

Fig.3.3. Side view illustration of the sample after ICP etching.

The etching time for 1mm disk is about 15 minutes at room temperature. After lift-off, DI water is added to the etch container several times to achieve a pH value of 7. At this point, the disks are ready for bonding to a dome lens.

Bonding. Van der Waals bonding is an established technique that has been used successfully in various applications [73-76]. The following steps are performed to directly bond the double heterostructure to ZnS or ZnSe dome lenses.

An ultrasound bath cleans the ZnS and ZnSe dome lenses first. The GaAs double heterostructure disks are suspended in water, then poured onto soft cleanroom wiper tissues. While the disk is still wet, the flat face of the dome is pressed gently on the disk. Proper alignment begins immediately to center the disk. After alignment, the

dome is gently pressed for a few seconds. Fig.3.4 shows the schematic of the bonded DHS sample on the dome lens.

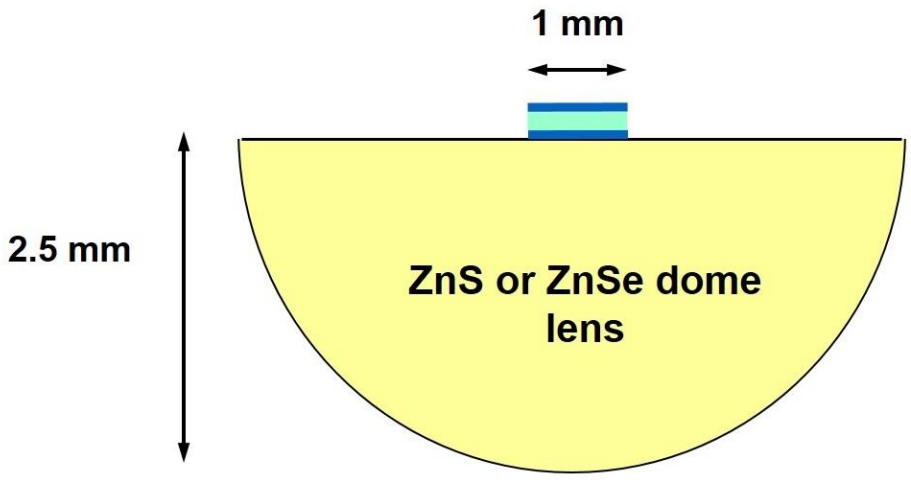

Fig.3.4. Schematic of the bonded DHS sample on the dome lens.

To judge the quality of the bonding, it is simple to observe the sample at perpendicular and grazing angles through the dome lens [41]. A completely visible disk from 0 to 80 degrees incidence indicates a uniform bond.

3.1.2 Lift-off and bonding with wax support

The previous procedure was used at the early stages of research for laser cooling of semiconductors. However, the whole process is very complicated and time-consuming. After lift-off, a samples floating in the DI water is very fragile and may shatter. This imposes limitations on the maximum size of the sample that can be lifted off without damage or distortion. The ones that remain intact tend to bend and curl after they are

poured onto the wiper tissues for bonding, making it difficult to perform the bonding as well as adding stress to the sample. In addition, for one batch, 20+ samples are made and normally only 1 or 2 are needed for bonding; the others are wasted. Thus, it is imperative to come up a simpler procedure that will eliminate or ameliorate the mentioned problems.

Yablonovitch *et al.* developed a procedure that uses pre-applied wax to support the samples during lift-off, making it robust and easy to handle [75]. We generally follow their method but make a few adjustments for our application. The following steps describe the current process of sample fabrication using wax support.

Cleaving. The wafer is cleaved into the desired sizes depending on different application requirements. Cleaving becomes difficult as sample sizes gets smaller. Samples as small as 1mm ×1mm to as large as 1cm ×1cm have been successfully cleaved.

Cleaning. The cleaved pieces of DHS sample are ultrasonically cleaned in DI water and subsequently cleaned in sequence with acetone, methanol, isopropanol, and DI water followed by nitrogen gas drying.

Applying wax. Pellets of Apiezon W wax (black wax) are cut off and placed on top the cleaved sample on the heterostructure side. The size of the pellet needs to be just slightly smaller than the size of the sample. With the sample on a microscope glass slide, it is transferred to a hot plate of 120 DegC. This temperature is high enough to melt the wax but low enough to prevent the wax from flowing uncontrollably. The black wax is slowly melted and fills the entire sample due to surface tension. If not all corners of sample are covered, more wax will be added and melted again for the entire surface of the sample to be covered.

In Ref [76], a recently developed technique to apply the Apiezon W wax to the sample is introduced. A heated syringe and needle (typically 100 to 120 DegC) is used to apply pure molten wax directly onto the sample. A subsequent reflow at an elevated temperature (typically 100 DegC) will form a smooth film. This technique can also be used to deposit wax selectively on mesas etched through the epilayers and AlAs lift-off layers. This apprarch is nesscessry if the sample is large or has fine features, but in our application sample is relatively small so simply placing pellet drops and melting is adequate.

As discussed before, to prevent the sample from re-attching to the substrate after lift-off, it needs to be placed upside down during the lift-off process. This is achievd by attaching the sample upside down to a Teflon fixture using blackwax (See Fig.3.5). We first place black wax on the Teflon fixture and melt it, then let the piece to cool for a few seconds before putting the sample on top of it. The temperature of black wax at that moment should be high enough to adhere the sample to the fixture but low enough to cause any reflow of the black wax on the heterostructure side of the sample.

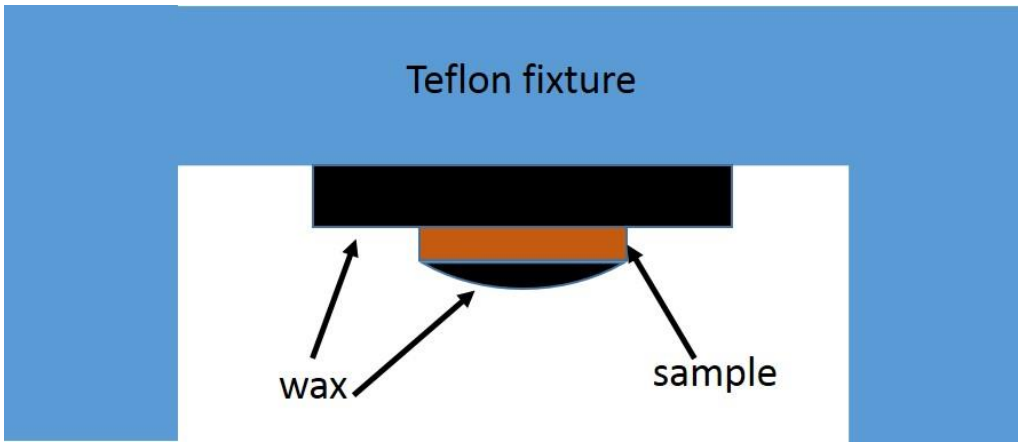

Fig.3.5 DHS Sample supported by black wax and adhered to a Teflon fixture before lift-off.

Lift off. Lift-off is accomplished by etching the AlAs layer with a 49.2% HF acid solution. In some cases, especially when dealing with large samples, the gas product created in the chemical reaction between HF and AlAs will crack the layer structure. If this happens, diluted HF solution (~10%) will be used to reduce the etch rate, which makes it easy for gas to escape and avoid cracking. After lift-off, DI water is added to the etch container several times to achieve a pH value of 7.

Bonding. The whole bonding process is performed under water to reduce contamination of the sample and to avoid exposing the crystal to air. The lifted-off sample is poured into a glass beaker with a valve-controlled drain at the bottom, which is custom-made from Adams & Chittenden Scientific Glass.

The bonding crystal is ultrasonically cleaned beforehand and also placed inside the beaker. If a hemisphere lens is used as the bonding crystal, it is initially fixed inside a small recess hole in a metal piece using clear wax, with the flat surface facing upward. This step is necessary to perform the bonding and the pressing after the bonding.

A Teflon vacuum wand from Fluoro Mechanic with both suck and blow function is used as a pick-and-place tool. The vacuum wand comes with attachable tips with holes of different diameters, making it possible to handle small semiconductor samples of varying sizes.

The water is gently stirred in the beaker to make the wax-side of the sample to face upward. Then the vacuum wand is used to pick up the sample and gently place it onto the desired position on the crystal. The water is slowly drained while the sample is gently pressed. After the water is completely drained, a lens tissue is placed on the

top of the sample to remove excess water. After drying, typically for one day under a weight of 20 g/mm^2, a close-contact Van der Waals bonding is obtained.

Remove wax. Apiezon W wax is removed by immersing the sample in Toluene solvent for 5 minutes. Clear wax is subsequently melted using Acetone to separate the hemisphere from the metal fixture. The sample is cleaned in DI water and dried by nitrogen gas.

In Ref [76], trichloroethylene solvent (TCE) is used to remove the black wax. However, our previous research shows that TCE is both toxic and very hard to clean and always leaves a small but measurable amount of residue. Such residue is deleterious for luminescence absorption. Toluene eliminates this problem as the sample is completely clean after black wax removal.

Fig.3.6 shows the surface morphology of two typical bonded samples under microscope magnification. The sample sizes are both about 1.5mm ×1.5mm. The bonding quality, as shown by surface morphology, varies from sample to sample. For some samples as shown in Fig.3.6(b), we observe some defects which are bubbles (i.e. unbonded areas) that form between the substrate and the film. This is most probably due to dust particles trapped on the back side of the film during the transfer from the original substrate to the new host substrate.

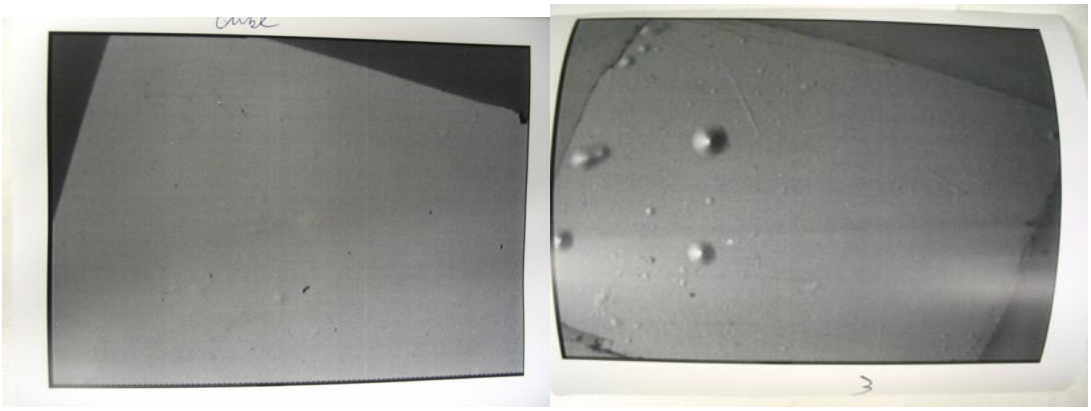

(a) (b)

Fig.3.6. Surface morphology of two DHS samples bonded to ZnS hemisphere lens.
(a) bonded sample with no bubbles (b) bonded sample with some bubbles.

Samples fabricated using wax support are found generally to have much better bonding quality compared to samples bonded without wax support. Thus, the fabrication procedure with wax support is now the standard processing approach for laser cooling application and the majority of the experimental data presented in this dissertation are from samples processed with wax support.

In conclusion, the process with wax support has the following advantages over the previous approach. First, it can produce samples with varying sizes easily; second, the whole process of lift-off and bonding is performed under water, minimizing contaminations from exposure to air; third, with support of black wax, the sample will not shatter and curl; fourth, the procedure distinguishes the two sides of the double heterostructure, which will minimize contamination as well as offer possibilities for experiments with asymmetric samples. Last but not the least, it is estimated that the new procedure will save more than 70% of the processing time compared to the previous approach.

3.2 Device fabrication for samples without release layer

In some occasions, we obtain samples without an AlAs release layer. Those samples cannot be lifted off using the previous method. In additional, there are other applications with quantum wells samples for Vertical External Cavity Surface Emitting Lasers (VECSEL) where AlAs is also a component of the Distributed Bragg Reflector (DBR), so lift-off using AlAs release layer is not an option.

Following Ref [77], we use a selective wet etching process to etch away the GaAs substrate. The following steps describe the process for GaAs substrate etch and subsequent bonding to crystal.

Cleaving, Cleaning, and Applying wax. These three steps are the same as for the fabrication of samples with release layer using wax support.

Protect the sidewall. Since the active region of the sample has the same material as the substrate, GaAs, the etchant will etch the active region from the side as well as etching the substrate vertically. To prevent this from happening, we protect the sidewalls of the sample using clear wax.

The first step is to melt a pallet of clear wax on a microscope slide on a hot plate of 90 DegC. After the wax is completely melted, the microscope slide is removed from the hot plate to cool off for a few seconds. While the wax is still soft, the semiconductor sample is placed onto the wax with the substrate side on the top (See Fig.3.7). The sample is then gently pressed into the clear wax. The temperature of the clear wax at the precise moment should be low enough to prevent any reflow of the black wax.

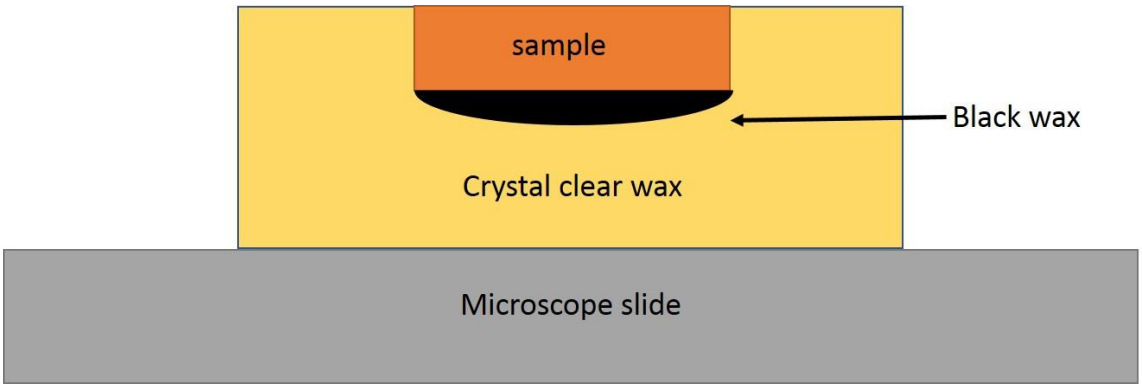

Fig.3.7. Schematic of the DHS sample supported by black wax and immersed inside clear wax before wet etching.

Selective wet etching. Ideally, the sample needs to be mechanically thinned to 100-150 μm before wet etching. This will largely help avoid over-etching and make the etched sample more uniform. Due to the lack of equipment, we do not perform this step and mainly rely on careful observation to stop the etching process at precise moment. The sample in placed on a holder in a home-made jet-etcher machine (Fig.3.8). The flow rate of etchant from the jet etcher is controlled by a valve. The etchant used is a mixture of hydrogen peroxide (H_2O_2) 30% concentrated and ammonium hydroxide (NH_4OH) 58% concentrated. The composition of the two solutions, which is given by the volume ratio $\gamma=V_{H_2O_2}/V_{NH_4OH}$, is the parameter which is used to vary the etch rate and insure the selectivity of the etch. Lepore *et al.* did a systematic study for the relationship between the volume ratio and etch selectivity [77]. We choose $\gamma=30$ in our experiment to have a reasonable selectivity and fast etch rate, which is estimated to be 3-6 μm/min depending on the flow from the jet etcher.

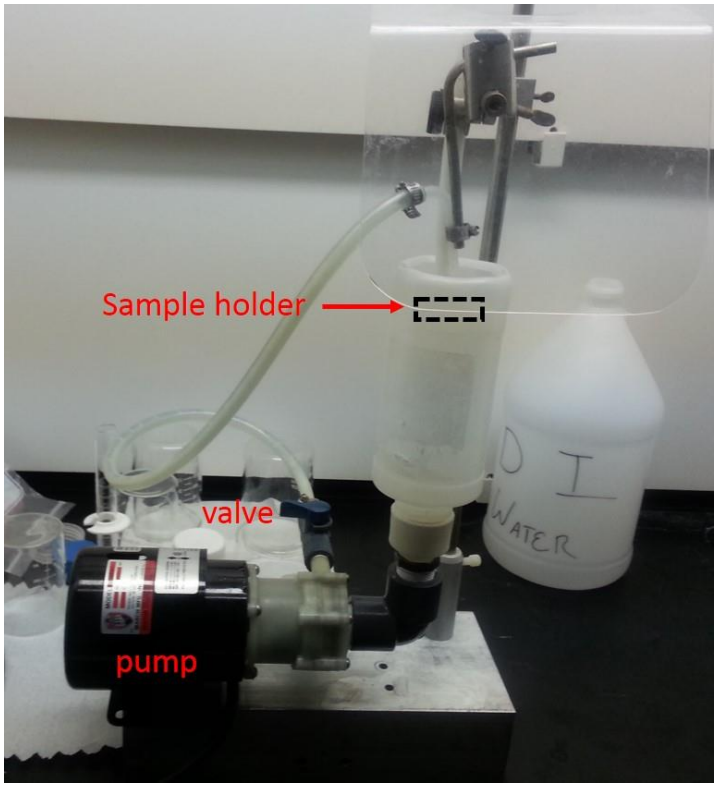

Fig.3.8. Picture of jet etcher.

As the sample is being etched, it will first become hazy and then at the spot where the flow directly hits, it will turn shiny with blueish color, which is the sign that it has etched through the GaAs layer and hit the InGaP layer. At this point, the flow is adjusted slower and then stopped when the entire sample becomes shiny.

The sample is rinsed in DI water immediately after wet etch.

Bonding The sample is immersed into Acetone to remove the clear wax. Afterward, the bonding follows the same procedure as described in Sec. 3.1.2.

3.3 Investigation of post-processing annealing

An additional bake-out procedure was tried after sample bonding by Demeester *et al.* [76]. They found out that this bake-out process would increase the bonding strength. The bake-out temperature depends on the material on which the sample is bonded. A bake-out under vacuum by increasing the temperature slowly to 450 DegC was necessary to get a good bonding strength on glass. A temperature of only 170 DegC is required for good bonding on a few hundred nanometer thick polyimide. They devise a 'Scotch Tape' test to quantify the strength of the bonding after bake-out at different temperatures. This test uses a Scotch tape to adhere to the sample and then strip it off quickly. The area of the sample that is striped off indicates the strength of the bonding. We repeated this test on a DHS sample bonded to ZnS flat pieces and obtained a similar result. There is a critical temperature of about 500 DegC, above which the strength of the sample is greatly enhanced (Fig.3.9). The temperature profile for the bake-out process is shown in Fig.3.10.

However, more tests show that when baked above 400 DegC, the DHS samples on ZnS tend to break into several pieces along the crystal axis, which prevent us from including this baking process into our standard fabrication procedure. This area needs more investigation in the future and could possibly lead to better bonding quality for the cooling sample. However, bake-out process could also lead to deleterious effects on the sample quality for cooling, specifically an increase of the non-radiative recombination rate [49], which should also be considered during future investigation.

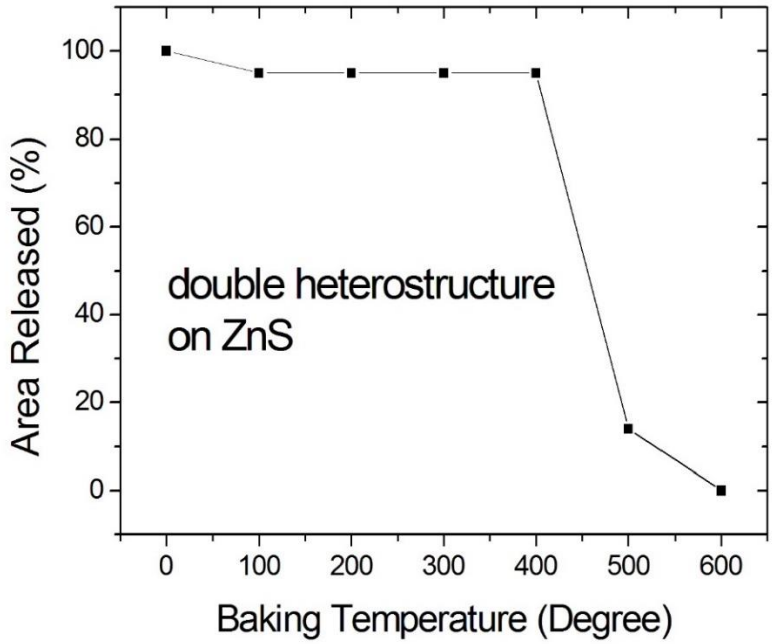

Fig.3.9. Influence of the bake-out temperature on the bonding strength (measured as the amount of released film after a tape test).

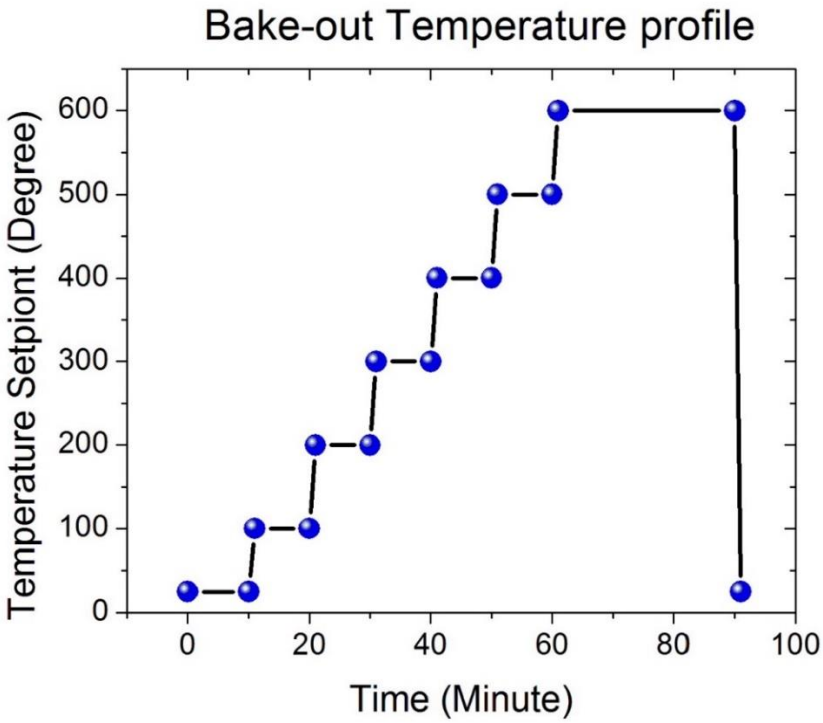

Fig.3.10 Temperature profile for the bake-out test.

3.4 Bonding quality measurement

The bonding quality of the sample is of critical importance. In laser cooling applications, good bonding ensures high luminescence extraction efficiency and enhances the external quantum efficiency. In VECSEL application, good bonding is needed for efficient heat dissipation, which is critical for laser performance.

One way to judge the bonding quality is to observe the sample at perpendicular and grazing angles through the dome lens. A completely visible disk from 0 to 80 degrees incidence indicates a uniform bond. However, this method is qualitative and subjective. A more quantitative way to determine the bonding quality is preferred.

In investigating the background absorption of the DHS sample (this part will be covered in detail in Chapter 4), we perform an experiment to measure the temperature change of the sample under constant pump power for a wide range of wavelengths. The temperature change is directly related to the absorption power of the sample at a given wavelength. The data shows a clear modulation feature, which we attribute to the etalon effect of the sample between air and the bonding crystal. The modulation amplitude, by simulation, is highly dependent on the index of material at both sides of the sample. For a good bonding, one side is air while the other is crystal; for a bad bonding, however, both sides are air (See Fig.3.11).

A sample with bonding judged to be acceptable by the subjective grazing-angle observation also shows etalon modulation features that match a simulation assuming an ideal interface (See Fig.3.12).

This method, however, involves precise temperature measurement and can be quite time-consuming, thus it might not be an ideal tool to determine the bonding

quality. But the available data still confirms our current process does produce high quality bonded samples.

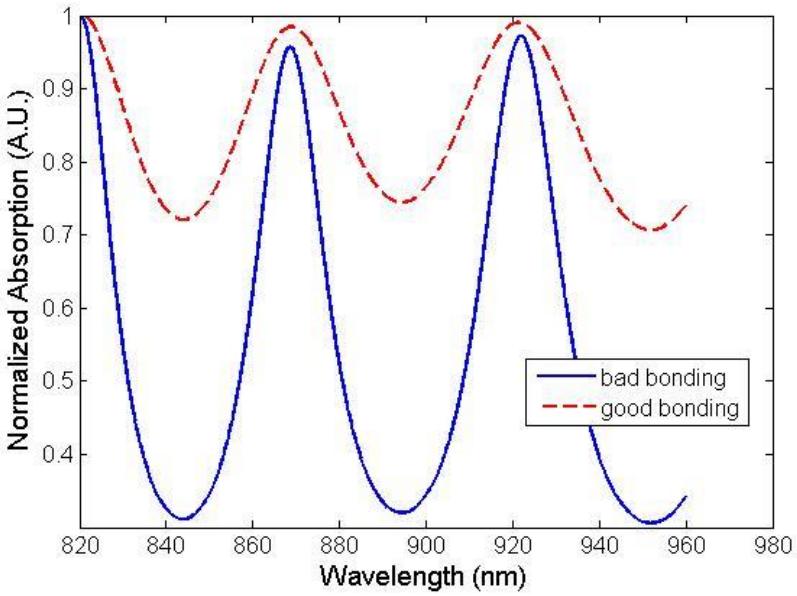

Fig.3.11 Simulation of absorbed optical power in the semiconductor DHS for good bonding (one side is air, the other side is ZnS) and for a bad bonding (both sides are air).

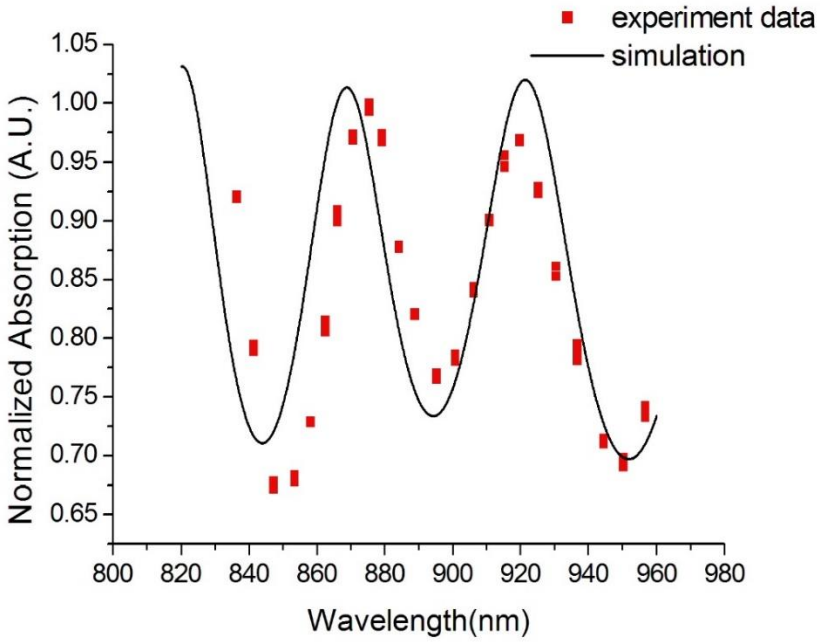

Fig.3.12. Experimental data (red dots) of the absorption in the semiconductor DHS matches well with simulation, confirming a good bonding.

Chapter 4

Precise Measurement of External Quantum Efficiency and Background Absorption in Semiconductors

4.1 Introduction

External quantum efficiency (EQE or η_{ext}) is an important parameter that characterizes many photonic devices. It is widely used to evaluate light emitting diodes (LED), photovoltaics, semiconductor lasers, and emerging technology such as laser-induced refrigeration of solids [5].

In photovoltaics, EQE is a measure of the available open-circuit voltage and high EQE is a necessity for approaching the Shockley-Queisser efficiency limit [78]. Thus a good solar cell should be designed as a good LED, with good light extraction.

As discussed in Chapter 2, EQE is a critical parameter in laser cooling of solids. The essential idea is to have a single coefficient that accounts for both the efficiency of the photon-electron conversion process (internal quantum efficiency) and the efficiency of moving light into and/or out of the device (coupling efficiency). Internal quantum efficiency is deleteriously affected when electronic excitations lose energy through the production of heat. This non-radiative recombination can be mediated by phonons, interfaces, surfaces, dislocations, defects, and even other charge carriers. The light coupling efficiency is driven by Fresnel reflection and the condition of total internal reflection. This leads to photon recycling and the concomitant production of wasteful heat due to the presence of parasitic background absorption. It is often difficult to model or even anticipate how the various disparate mechanisms degrade performance. Instead, empirical data should guide device development. It is therefore crucial to have in place an experimental scheme for precision measurement of efficiency. This allows such problems to be identified and addressed systematically.

In this Chapter, we present a procedure for precision quantification of photoluminescence external quantum efficiency in bulk GaAs double heterostructures. Device characterization is performed in the context of optical refrigeration (laser cooling in solids), where the demands on EQE are extreme. For this application, EQE is defined as the fraction of photo-excited electron-hole pairs which produce luminescence photons that escape the device into free-space. It has been established that laser-induced cooling of GaAs will occur only when EQE exceeds 99%, i.e. far greater than needed for useful operation of other semiconductor photonic devices [30]. In addition, it becomes progressively more difficult to make an accurate measurement

of EQE as its value approaches unity. These challenges have driven the development of the methodology described here. We emphasize that our results are general. The principles may be applied to a variety of photonic systems, including those not based on semiconductors.

Schnitzer *et al.* measured the EQE of planar AlGaAs/GaAs/AlGaAs double heterostructures at room temperature by pumping above the bandgap (cw diode laser at λ = 780 nm) and collecting the integrated photoluminescence [79]. This signal was referenced to scatter from a white Lambertian surface to calibrate the EQE. They observed an EQE as high as 72% corresponding to an internal quantum efficiency of 99.7% in the GaAs layer. Dunstan pointed out that separate measurement of photoluminescence and a photo-thermal signal for the same excitation conditions can yield the absolute quantum efficiency [80]. This is because the absorbed power must be converted into either light or heat: a fractional increase of one must be accompanied by a fractional decrease of the other. This approach can give higher measurement accuracy as EQE approaches unity. Gfroerer *et al.* used this principle to measure an EQE as high as 63% with an InP/InGaAs heterostructure [43]. Luminescence was collected in tandem with sample temperature using a thermistor as a function of excitation power. By normalizing these two fractional quantities to the excitation power and plotting them against each other, the expected linear relationship is observed. Absolute calibration is then attained with a least-squares fit of the data.

Extremely high internal quantum efficiency of GaAs is attained when surface recombination is passivated with GaInP layers. Using a modified form of the above experiment, Catchpole *et al.* measured an EQE of 92% with a passivated GaAs/GaInP

planar heterostructure mounted on a ZnSe substrate [81]. They showed that modulated pump light can increase sensitivity and reduce complications from long-term thermal drift. Gauck *et al.* attached a similar GaAs/GaInP heterostructure to a ZnSe hemispherical lens to increase luminescence extraction efficiency, resulting in an EQE of 96% at the optimum excitation level [41]. Operating a similar device at 100K resulted in an EQE approaching 99% [5].

All the preceding measurements of EQE take place by varying the pump power at a fixed wavelength, i.e. at a wavelength where absorption is strong and sufficiently separated from the mean luminescence wavelength. Gauck *et al.* realized that when EQE is exceptionally high, tuning the pump wavelength below the mean luminescence wavelength at an optimized, fixed photo-excitation might lead to the observation of net cooling. In a second experiment, they tuned the pump wavelength through the mean luminescence wavelength of GaAs and into the band-gap absorption edge. At a constant photo-excitation, they measured reduced heating into the band tail, but no net cooling [41]. They did demonstrate, however, the high quality of their GaAs sample and the potential for semiconductor-based optical refrigeration. Their work generated a strong interest in laser-cooling with GaAs and led to more theoretical and experimental research [5, 28, 29, 42, 44, 46, 47].

In this Chapter, we show that wavelength-dependent temperature change can be used to directly measure the photoluminescence EQE of a semiconductor photonic device. This approach has been effective for characterizing optical refrigerators made from rare-earth doped fluoride glass and crystal [11]. It is based on Dunstan's concept

of simultaneous measurement of fluorescence and temperature, but has the advantage that absolute EQE is obtained from uncalibrated temperature measurements only.

4.2 Theoretical fundamentals for measurement of external quantum efficiency

For an intrinsic semiconductor, the recombination of photo-generated electron hole pairs (N) is conveniently written as the sum of the non-radiative (AN), radiative (BN^2), and Auger (CN^3) processes, where A, B, and C are corresponding decay coefficients [30]. This defines the internal quantum efficiency:

$$\eta_{int} = \frac{BN^2}{AN + BN^2 + CN^3} \tag{4.1}$$

All of these coefficients are temperature dependent. For bulk, crystalline GaAs used in heterostructures, the B and C coefficients are fundamental properties and should not depend on the growth process. The non-radiative decay, however, depends on purity but is primarily affected by surface recombination [82]. It can be mitigated by passivating the interfaces in the epitaxial growth of double heterostructures, which dramatically enhances internal quantum efficiency.

The luminescence extraction efficiency (η_e) accounts for radiation trapping and re-absorption (i.e. photon recycling), which limits the amount of luminescence that exits the heterostructure. Light escaping from a high refractive index semiconductor such as GaAs into air or vacuum experiences severe radiation trapping due to total internal reflection giving $\eta_e \sim 2\%$. This can be improved by surface texturing [83],

photonic crystal structures [84], or the use of nearly index-matching domes as in LED technology [85]. We use GaAs/GaInP lattice-matched heterostructures grown by metal-organic chemical vapor deposition (MOCVD) or molecular beam epitaxial (MBE). Referring to Fig.4.1, samples can be detached from the GaAs substrate by etching a thin release layer of AlAs using HF. Released structures are then van der Waals bonded to nearly index-matched dome lenses formed from ZnS or ZnSe to increase η_e by about an order of magnitude. These materials are used because of their very low absorption at the luminescence wavelengths of GaAs [86]. Details of the sample fabrication is covered in Chapter 3.

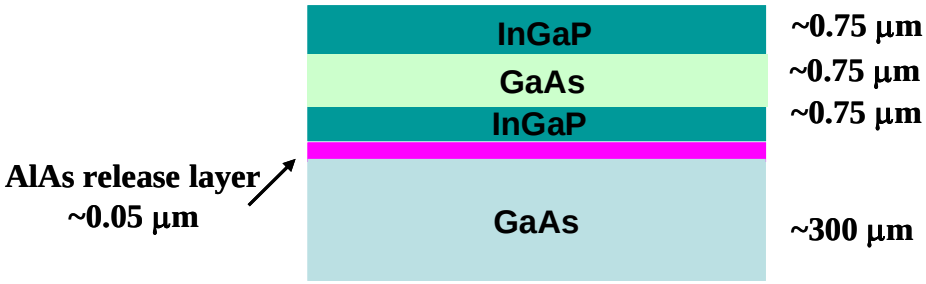

Fig.4.1. Sample structure for laser cooling of semiconductors. An AlAs layer is used to liftoff the sample from the substrate.

The coefficients η_{int} and η_e define EQE (η_{ext}) as the fraction of photo-generated electron-hole pairs that appear as luminescence photons outside the structure [5]:

$$\eta_{ext} = \frac{\eta_e BN^2}{AN + \eta_e BN^2 + CN^3} \tag{4.2}$$

To proceed, we write the net power (P_{net}) deposited in the sample by laser excitation at frequency ν as [30]:

$$P_{net} = \alpha_r(\nu)I - \eta_e BN^2 h\tilde{\nu}_f = \eta_e BN^2(h\nu - h\tilde{\nu}_f) + ANh\nu + CN^3 h\nu$$
$$= h\tilde{\nu}_f \eta_e BN^2 \left(\frac{1}{\eta_{ext}} \frac{\nu}{\tilde{\nu}_f} - 1 \right) \tag{4.3}$$

where $\alpha_r(\nu)$ is the frequency-dependent resonant band-edge absorption coefficient, I is the laser intensity and the escaped (i.e. measured) mean luminescence frequency $\tilde{\nu}_f$ is defined as:

$$\tilde{\nu}_f = \frac{\int S(\nu)R(\nu)\nu d\nu}{\int S(\nu)R(\nu)d\nu} \tag{4.4}$$

Here $S(\nu)$ is the geometry-dependent escape probability and $R(\nu)$ is the luminescence spectral density.

The term in front of the bracket in Eq. (4.3) represents the escaped luminescence power density:

$$P_{lum} = h\tilde{\nu}_f \eta_e BN^2 \tag{4.5}$$

The pump-induced temperature change ΔT, which is proportional to P_{net}, can therefore be written as:

$$\Delta T = \kappa P_{net} = \kappa P_{lum} \left(\frac{1}{\eta_{ext}} \frac{\nu}{\tilde{\nu}_f} - 1 \right) \tag{4.6}$$

where κ is a proportionality constant depending on the thermal load on the sample.

Measuring the temperature change as the pump frequency λ is scanned while maintaining constant photo-excitation (i.e. maintaining P_{lum} constant) generates a straight line given by Eq. (4.6). The x-axis crossing point corresponds to $\Delta T = 0$ and defines the pump frequency where heating exactly balances cooling, i.e., ν_{cross}. This zero-crossing condition (x-axis intercept of Eq. (4.6), which represents the onset of laser cooling) has never been attained in experiments with semiconductors due to the presence of background absorption as discussed below. The zero-crossing in semiconductors can be deduced, however, by linear extrapolation of the frequency-dependent heating data. EQE is then found by forming the ratio:

$$\eta_{ext} = \frac{\nu_{cross}}{\tilde{\nu}_f} \tag{4.7}$$

At and below the energy band-gap of the semiconductor, non-resonant parasitic absorption may be evident. This is caused by impurities and becomes important when resonant absorption weakens in the band-tail states. To account for the presence of background absorption, we write:

$$\eta_{abs}(\nu) = \frac{\alpha_r(\nu)}{\alpha_r(\nu) + \alpha_b} \tag{4.8}$$

where α_b is the parasitic/background absorption coefficient that is assumed to be constant. The absorption efficiency falls off rapidly when pumping at wavelengths longer than the band-gap. Eq. (4.6) is modified to account for the absorption efficiency:

$$\Delta T = \kappa P_{net} = \kappa P_{lum}\left(\frac{1}{\eta_{ext}\eta_{abs}}\frac{\nu}{\tilde{\nu}_f} - 1\right) \tag{4.9}$$

The product $\eta_{ext}\eta_{abs}$ describes the efficiency of converting an absorbed laser photon to an escaped luminescence photon.

4.3 Experimental setup and results

Following Gauck *et al*., we tune the pump wavelength and monitor the relative temperature change. The photoluminescence P_{lum} gives direct measure of the excitation density and must be maintained constant. We collect the full luminescence spectrum with a CCD array, including some of the scattered pump laser. The collection optics are aligned to minimize scattered laser light; residual signal is removed from the PL with a numerical procedure. Our experiment differs from Ref. [41] in several respects. We measure EQE over a range of temperatures at and below room temperature (80-300K) by mounting the sample in an optical cryostat. EQE increases at lower temperature because the recombination components change favorably, i.e. *B* increases, while *A* and *C* decrease [53, 61, 62]. The GaAs heterostructure is attached to a ZnS hemispherical lens by van der Waals bonding instead of using wire clamps (See Fig.1.4). A clamping fixture is undesirable because it can absorb luminescence, heat up, couple thermal energy back into the sample, and reduce the EQE. For the same reason, we do not use contact thermocouples or thermistors to measure temperature. In this demanding application, temperature must be determined with an all-optical approach.

4.3.1 Differential luminescence thermometry

Infrared cameras detect thermal black body radiation and are often used for non-contact temperature measurement. At low temperature and/or when the material of interest is transparent at thermal wavelengths, these cameras are inadequate. This is the case with the semiconductor GaAs, which has a direct band gap of about 1.42 eV (870 nm) at 300 K. Instead, we use the temperature dependence of the luminescence resulting from band-gap shift and broadening. The peak of the luminescence spectrum clearly marks the fundamental band edge. In addition, the shape of the spectrum reveals temperature-dependent photo-carrier populations. These features are depicted in Fig.4.2. The combination of spectral shift and broadening provides exceptional temperature resolution when implemented with direct band gap semiconductors such as GaAs. We can then determine whether a material is heating or cooling and by how much. A comprehensive reference on the subject of temperature measurement using luminescence can be found in the text by Zhang and Grattan [87].

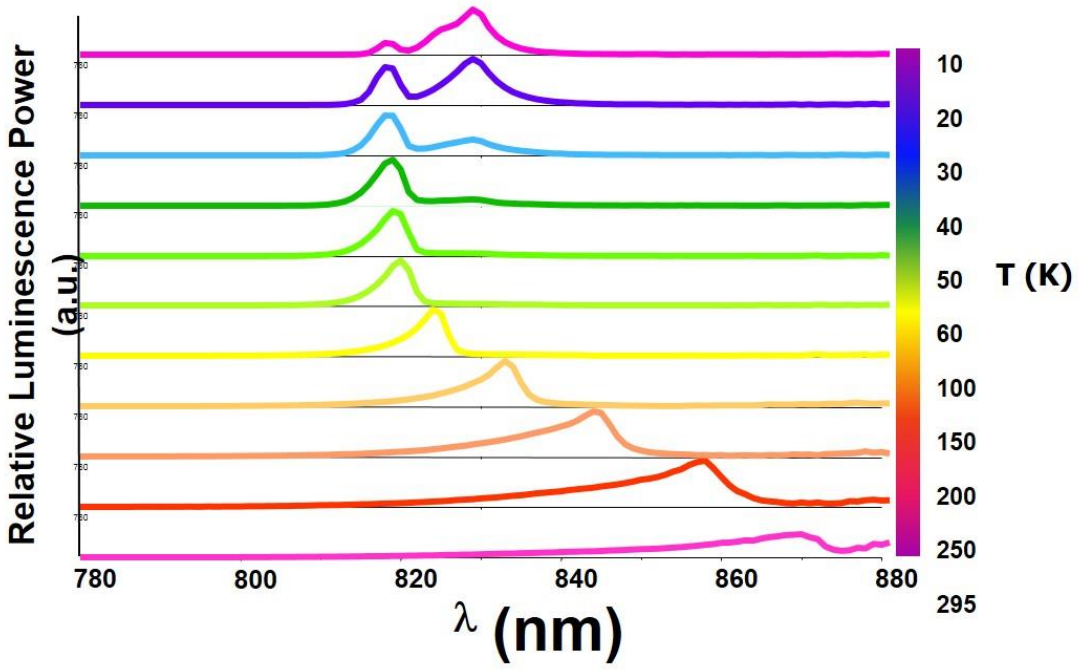

Fig.4.2. Luminescence of GaAs in the range 10-295 K. Excitation is with a 5mW laser at a wavelength λ=532 nm far above the band gap [49].

We demonstrate the sensitivity of our method as follows. A GaAs heterostructure bonded to a ZnS hemispherical lens is held on the coldfinger of an optical cryostat with its temperature controlled to 100K ± 1 mK by a proportional-integration servo-loop. A cw probe laser (λ = 680 nm; power: ~ 5 mW) weakly photo-excites the sample resulting in a continuous luminescence spectrum shown in Fig.4.3(a). When the cryostat setpoint is lowered, the sample cools and the band-gap expands resulting in a blue-shift of the peak luminescence. Conversely, raising the setpoint causes a luminescence red-shift. Two spectra obtained at temperatures differing by 500 mK are superimposed in Fig.4.3(a) and appear identical. After normalization and subtraction, however, a peak and valley is evident as shown in Fig.4.3(b). The resulting differential signal is a peak-valley or a valley-peak feature depending on the sign of

temperature change while the height of the differential peak indicates the magnitude. By controlling scattered light and dark current, the limitation imposed by signal-to-noise gives a differential temperature resolution of better than 1 mK at 100K. We call this technique differential luminescence thermometry (DLT). Therefore, the combination of the two techniques of DLT and the laser-induced temperature change can be viewed as an All-optical Scanning Laser Calorimetry or ASLC, for brevity.

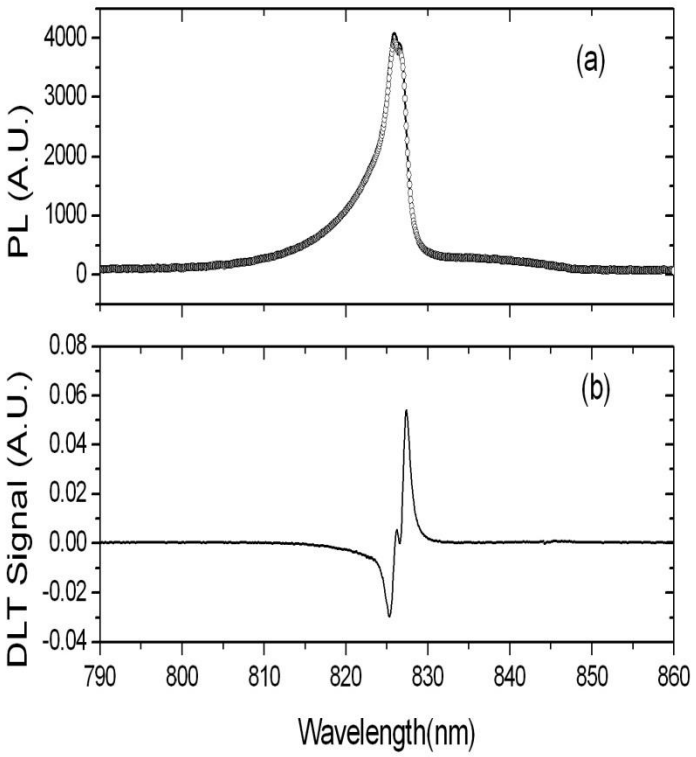

Fig.4.3. (a) Bandgap luminescence of GaAs at 100 K and 100.5K. The overlapped spectra (solid line and open circles) appear identical except at the peak. (b) Subtracted spectra clearly reveal a differential (or DLT) signal corresponding to a temperature change of 0.5 K.

4.3.2 Experiment setup for ASLC

In the EQE experiment shown in Fig.4.4, we use a GaAs/GaInP passivated heterostructure bonded to a ZnS hemispherical lens. A reference spectrum is recorded at the cryostat temperature setpoint of 200K with the pump laser blocked. New spectra are then obtained as the unblocked pump laser is tuned; these are normalized and subtracted from the reference to determine the pump-induced temperature change via DLT. The pump laser is homebuilt cw Ti:sapphire laser producing up to 4.5W tunable in the wavelength range of 750–900 nm. The thermal link between sample and coldfinger is adjusted so the sample can attain a new steady state temperature in the presence of pump light on the timescale of ~ 1 minute. It is important to emphasize that there are two photoluminescence signals: i) PL from the pump to monitor photo-excitation and ii) PL from the probe to track temperature. The signals are separated with time-gating. DLT data is collected by chopping the pump beam at 5 Hz and synchronously gating the spectrometer CCD readout, i.e. temperature spectra are recorded when the pump is momentarily blocked and the high density PL has decayed. Luminescence temperature measurements of GaAs must be made in the small-signal regime because of complications that can occur with changing photo-excitation density. The diode probe laser wavelength is chosen to be sufficiently short (λ = 680 nm) so it does not appear in the recombination spectrum. Spectra are normalized at the band edge wavelength (i.e. at the peak of the luminescence spectrum) and subtracted from the normalized reference spectrum to generate a DLT signal.

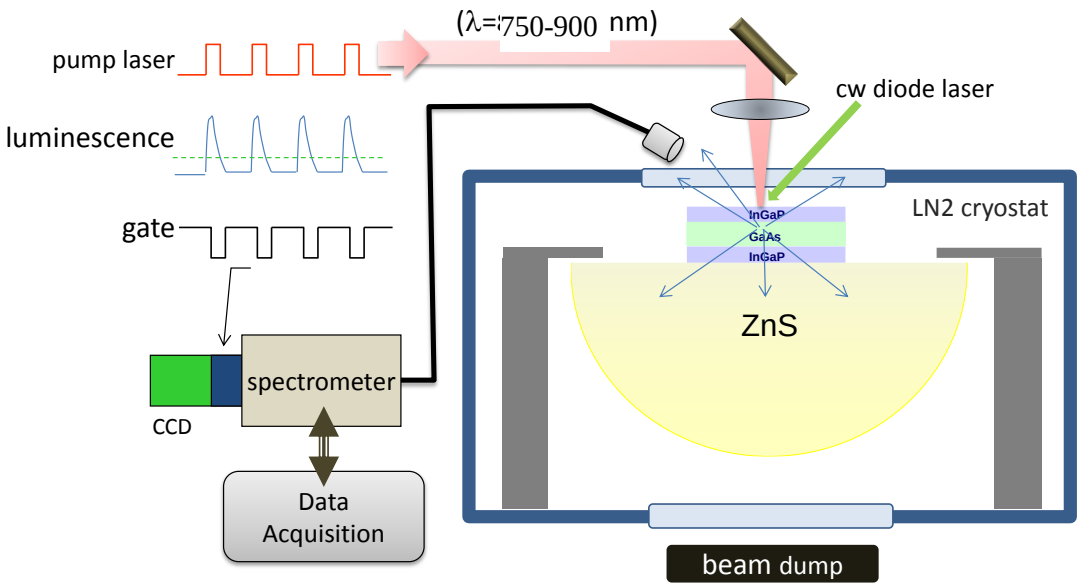

Fig.4.4.Experimental setup of All-optical Scanning Laser Calorimetry (ASLC) for measuring the external quantum efficiency at various lattice temperatures in GaAs/GaInP double heterostructures. The temperature change is measured using differential luminescence thermometry (DLT).

Fig.4.5 shows ASLC data as the pump is tuned between $1.50eV < hv < 1.60\ eV$. Although not a requirement, the y-axis depicts temperature change in degrees Kelvin. Axis calibration is made in a separate experiment to verify the linearity of DLT for the specific conditions. The temperature change ΔT varies linearly with v provided the photo-excitation density is kept constant. Because the resonant absorption $\alpha_r\ (v)$ is frequency-dependent, the laser power must be adjusted as it is tuned to maintain the density as ascertained by a constant integrated PL spectrum. The data for pump frequencies $\nu > \tilde{\nu}_f$ is fit with a least-squares procedure and extrapolated to give a zero-crossing frequency of hv_{cross}=1.399 eV. The mean luminescence photon energy

$h\tilde{\nu}_f = 1.478eV$ is calculated from the high density PL spectrum, resulting in η_{ext} = 94.7 ± 0.15% using Eq. (4.7).

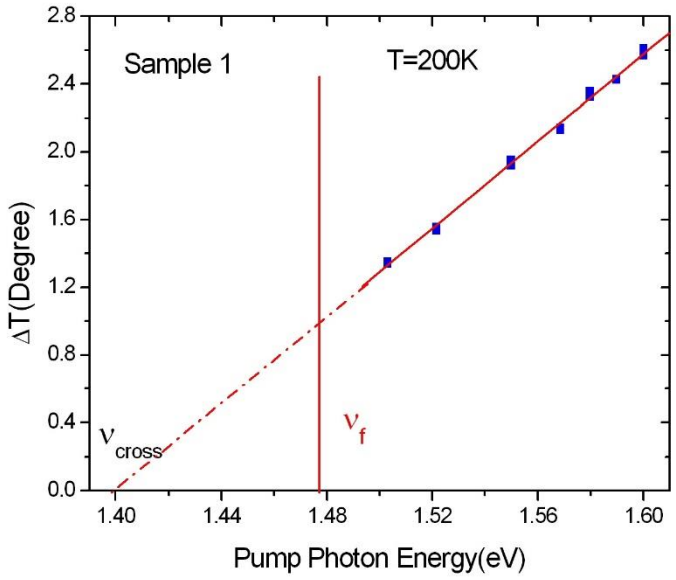

Fig.4.5. Differential heating data obtained by ASLC method for measuring the external quantum efficiency on sample 1.

At frequencies smaller than $\tilde{\nu}_f$, parasitic absorption cannot be neglected in comparison to resonant absorption. The absorption efficiency deviates significantly from unity (η_{abs} < 1) with a strong frequency-dependence. This is the cause of the departure from the linearity exhibited in Fig.4.7. To account for the behavior at and below the band-gap energy, we need an accurate measure of $\alpha_r(\nu)$ to use in Eq. (4.8). This is gained from a separate PLE measurement; results are shown in Fig.4.6. By assuming a frequency-independent background absorption (α_b = 15 cm^{-1}) as a fitting parameter, our model can accurately describe the full range of heating data shown in

Fig.4.7 (solid curve). High frequency pump photons independently determine the EQE while pumping in the band-tail quantifies the background absorption.

Using the technique and setup above, we have tested a series of samples at various temperatures and carrier densities. The samples are either grown by MBE, provided by Andreas Stintz at Center for High Technology Materials (CHTM) at University of New Mexico (UNM) or grown by MOCVD, provided by Jeffrey Cederberg at Sandia National Laboratory (SNL) and Jerry Olson at National Renewable Energy Laboratory (NREL). The results of all tests are summarized in Appendix A. A general conclusion is that samples grown by MBE have lower parasitic absorption compared to MOCVD.

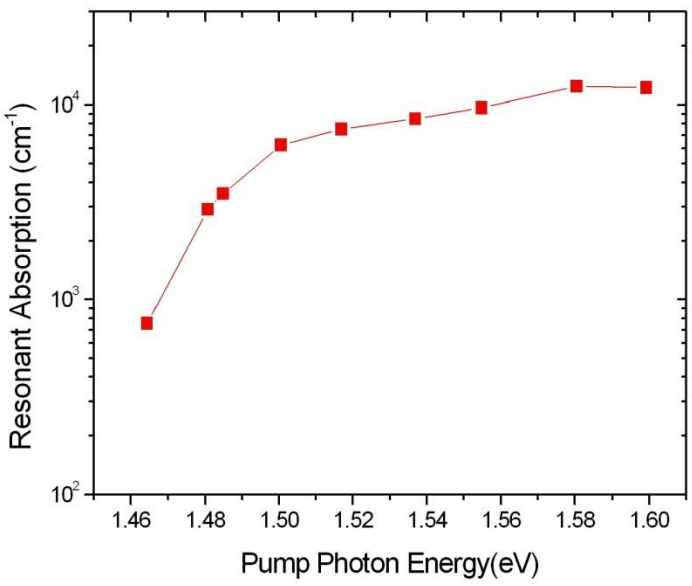

Fig.4.6. Resonant absorption coefficient as a function of photon energy obtained from photoluminescence excitation (PLE) measurement.

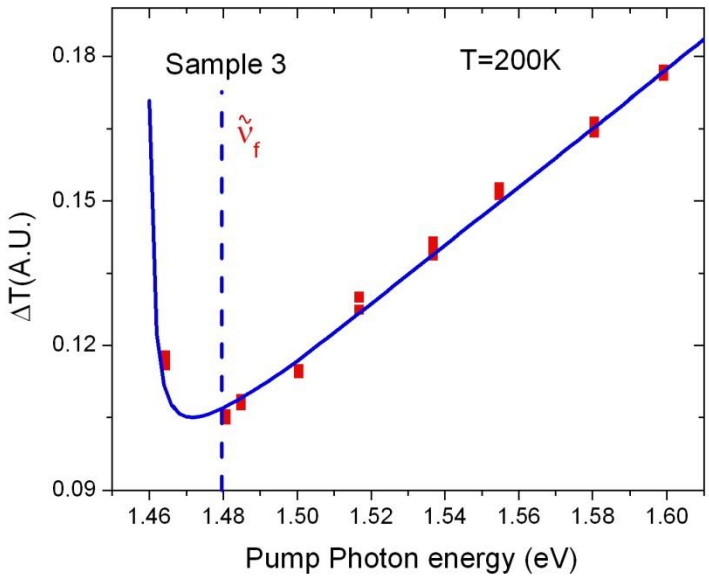

Fig.4.7. Scanning laser calorimetry for sample 3. The presence of background absorption prevents the observation of net cooling at long wavelengths.

Repeatability of the ASLC technique is proved to be very good. Fig.4.8 shows a series of tests done at 100K on one sample, spanning over almost one year. Note that even though different test results are expected due to slightly different pump spot for each experiment, the EQE data are still consistent for the same conditions for all tests.

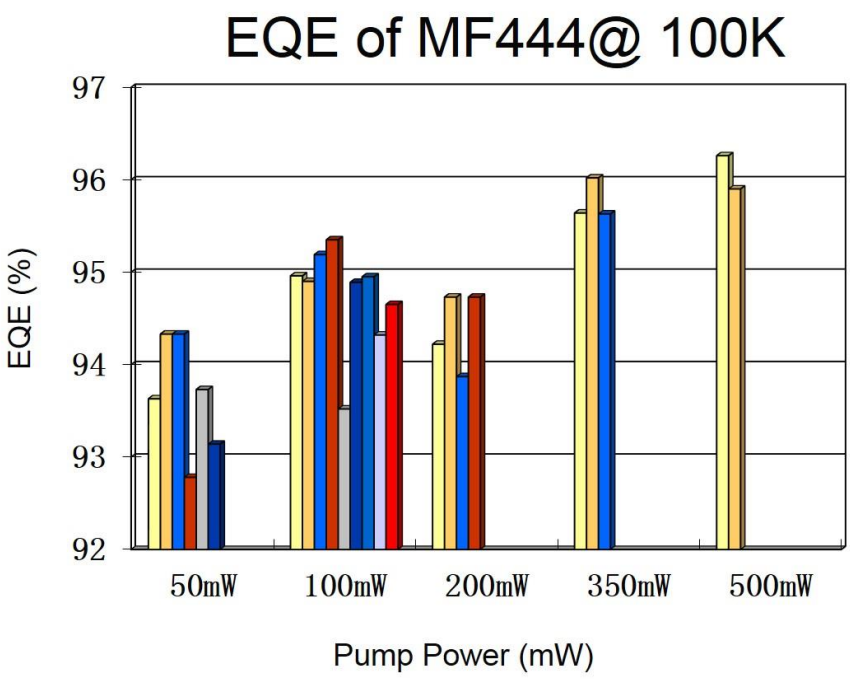

Fig.4.8. Results of EQE for one sample (MF444) under different carrier densities at 100K.

4.3.3 Optimum carrier density for EQE

In semiconductors, EQE is a nonlinear function of carrier density and temperature as can be seen in Eq. (4.2). At very low and very high carrier densities, the non-radiative and Auger recombination, respectively, will dominate and degrade EQE. The optimum density has been shown to have the following analytical form:

$$N_{opt} = \sqrt{\frac{A}{C}} \tag{4.10}$$

and the corresponding optimum absorbed pump power density is:

$$P_{opt} = h\nu\eta_e BN_{opt}{}^2 = h\nu\frac{A\eta_e B}{C} \tag{4.11}$$

It is assumed that the device is pumped in the density regime where radiative recombination dominates, i.e. $BN^2 >> AN + CN^3$. The maximum attainable EQE is then [5, 30]:

$$\eta_{ext}^{\max} = \frac{\eta_e B N_{opt}^{\ 2}}{A N_{opt} + B N_{opt}^{\ 2} + C N_{opt}^{\ 3}} \approx 1 - \frac{2\sqrt{AC}}{\eta_e B} \tag{4.12}$$

For EQE approaching unity, we can define a normalized absorbed pump power density at a given wavelength:

$$\bar{P} = \frac{P_{abs}}{P_{opt}} \approx \frac{N^2}{N_{opt}^{\ 2}} \tag{4.13}$$

This allows EQE to be written as an explicit function of pump power:

$$\begin{aligned} \eta_{ext}(\bar{P}) &= \frac{\eta_e B N^2}{AN + \eta_e B N^2 + CN^3} \\ &= 1 - \frac{AN + CN^3}{\eta_e B N^2} \\ &\approx 1 - (1 - \eta_{ext}^{\max}) \frac{1 + \bar{P}}{2\sqrt{\bar{P}}} \end{aligned} \tag{4.14}$$

This power dependence is plotted in Fig.4.9 with the peak identifying the optimum pump power. EQE is far more sensitive to the pump power below the optimum level than above it.

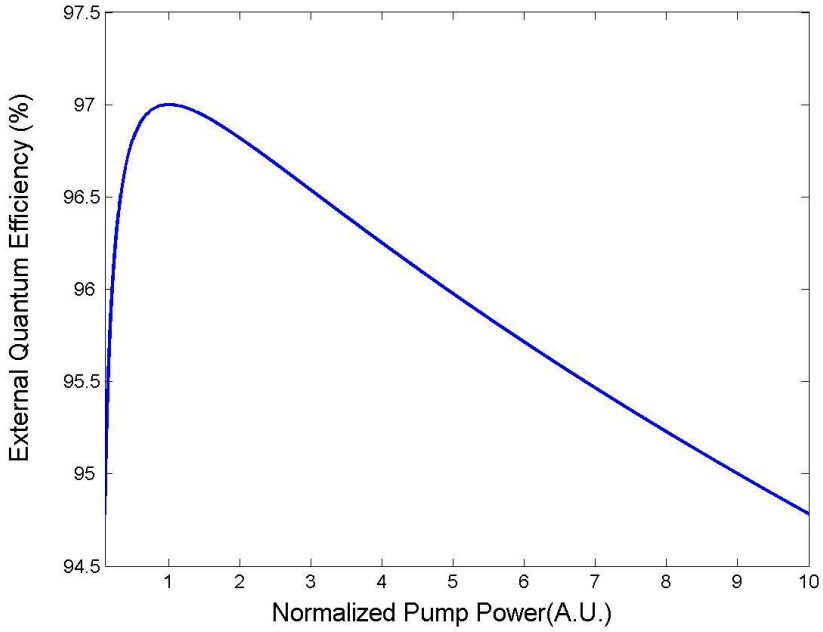

Fig.4.9. Calculated external quantum efficiency as a function of normalized pump power assuming a maximum external quantum efficiency of 97%.

One experimental approach for determining the optimum carrier density is to measure EQE directly at a range of photo-excitation levels, but this is a very time-consuming process. A direct and equally precise method is to measure sample heating at a fixed wavelength with varying pump power.

We can write the net heating power as follows:

$$P_{net} = \alpha_r I \left(1 - \eta_{ext}(P) \frac{\tilde{\nu}_f}{\nu} \right) \tag{4.15}$$

Given that $\Delta T \propto P_{net}$ and the incident pump laser power at a given wavelength $P \propto P_{abs} = \alpha_r I$, we have

$$\frac{\Delta T}{P} \propto 1 - \eta_{ext}(P) \frac{\tilde{\nu}_f}{\nu} \tag{4.16}$$

With the help of Eq. (4.14), this temperature change per input power is plotted in Fig.4.10 for $\tilde{\nu}_f / \nu$ = 0.9, 0.95, and 1.00. Each curve minimum clearly identifies the optimum pump power.

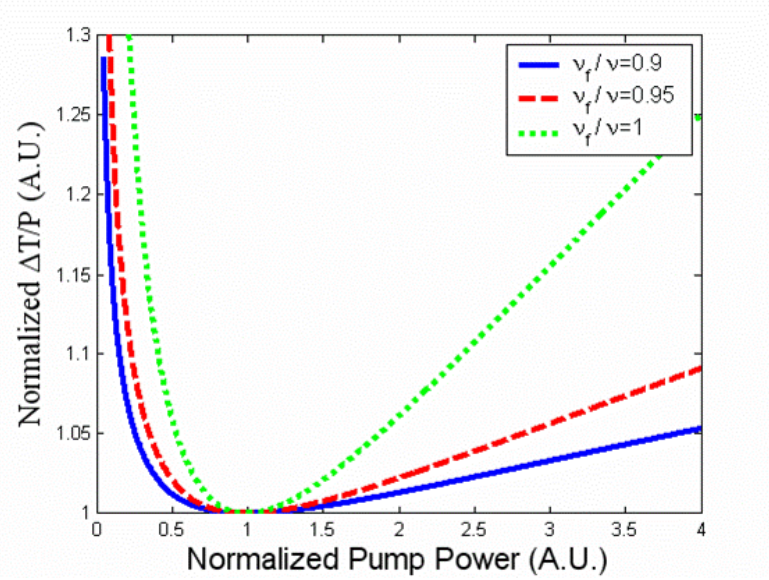

Fig.4.10. Calculated heating to power ratio as a function of normalized pump power.

Experimental results for sample 3 at 100K are shown in Fig.4.11. An optimum excitation power of ~200 mW for a spot size of ~150 μm corresponds to an optimum carrier density of $\sim 3 \times 10^{17} cm^{-3}$.

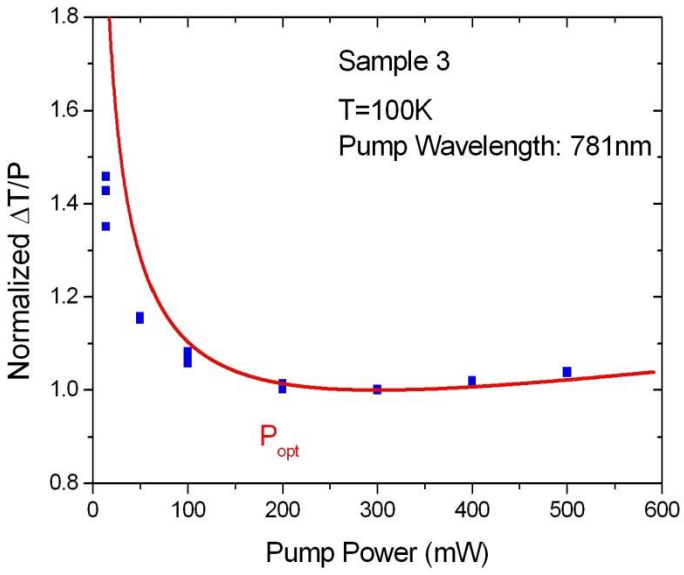

Fig.4.11. Power-dependent temperature measurement data for sample 3 at 100K using differential luminescence thermometry. Blue dots are the experimental data and red line is the theoretical curve (Eq. 4.16) using $\eta_{ext}^{max} = 91\%$.

The optimum power or carrier density can be independently verified with a complementary but less complicated power-dependent photo-luminescence (PDPL) measurement. The use of PDPL technique as a method to obtain the value of EQE rapidly will be covered in Chapter 5.

From Eqs. (4.2), (4.3), and (4.5), we can re-write the spectrally-integrated exiting luminescence power density as follows:

$$P_{lum} = h\tilde{\nu}_f \eta_e B N^2 = \frac{h\tilde{\nu}_f}{h\nu} P_{abs} \eta_{ext}(P) \tag{4.17}$$

In an experiment where the laser wavelength is fixed, the relative luminescence signal normalized to incident laser power (P) as we vary the power is:

$$\frac{P_{lum}}{P} = \beta \eta_{ext}(P) \tag{4.18}$$

where β is a constant. The normalized luminescence power scales directly with EQE and shows a maximum at the optimum pumping power. This is demonstrated experimentally on sample 3 in Fig.4.12. PDPL is generally simpler and easier to implement because it does not require resolution of what are usually small temperature changes in the former approach.

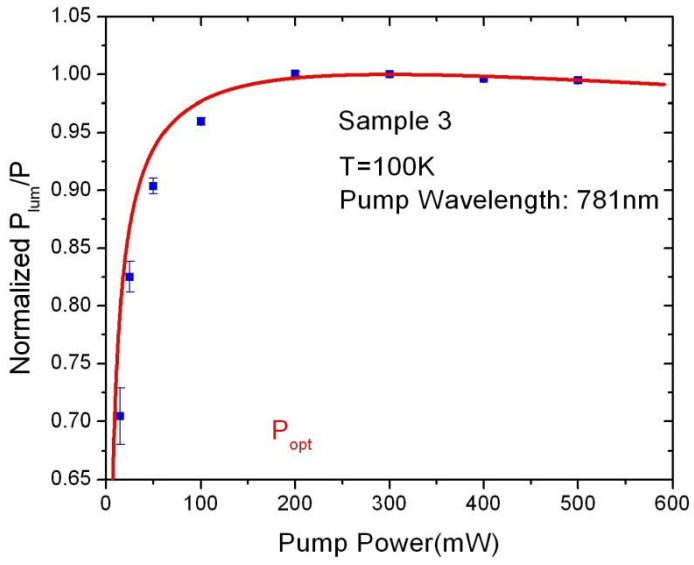

Fig.4.12. Power-dependent photoluminescence measurement on sample 3 at 100K. Blue dots are the experimental data and red line is the theoretical curve.

4.3.4 Temperature dependence of EQE

EQE is temperature-dependent because the radiative and non-radiative rates exhibit strong temperature dependence. Radiative recombination scales as $B \propto T^{-3/2}$ to T^{-2} [62]

and Auger recombination has been shown to follow the form $C \propto \exp(-T_a / T)$ where T_a is a characteristic temperature that depends on the details of the band-structure [61]. For dominant Auger process that involves electron/electron/heavy-hole, $T_a \sim \mu E_g / k_B$ where $\mu = m_c / m_h < 1$ is the ratio of electron to heavy-hole effective masses, and k_B is the Boltzmann constant.

The non-radiative decay is known to have different temperature behavior depending on the mechanism. It has been suggested that surface recombination should display an activation energy (temperature) similar to the Auger process, i.e. $A \propto \exp(-T_S / T)$ [62], although such a generalization has not been experimentally established. Recent modeling in GaAs/GaInP heterostructures suggests more complex density and temperature dependence as the doping type and level in the core and passivation layers are varied [40]. The temperature dependence of coefficients *A*, *B* and *C* in Eq. (4.2) predicts higher EQE at lower lattice temperatures. This is confirmed by our measurements for sample 1 as shown in Fig.4.13.

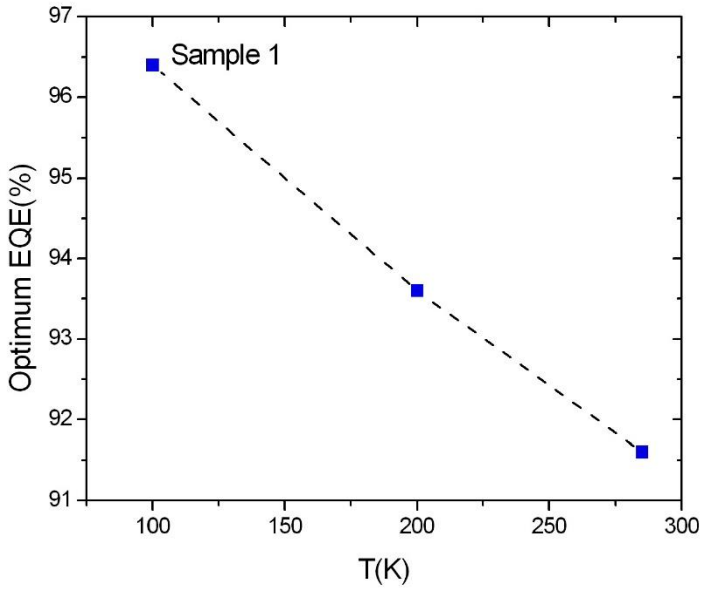

Fig.4.13. Measured external quantum efficiency as a function of temperature for sample 1.

We also find the optimum pumping power at different setpoint temperatures using PDPL; results are displayed in Fig.4.14. Although the trend is similar to that observed with EQE, it is important to point out that the functional dependence of the coefficients is different: optimum EQE is $1-2\sqrt{AC}/\eta_e B$ (Eq. 4.12) while optimum power scales as *AB/C*. The data in Fig.4.14 indicates that *B* and *C* experience a stronger temperature-dependence compared to *A* (i.e. $T_a << T_s$).

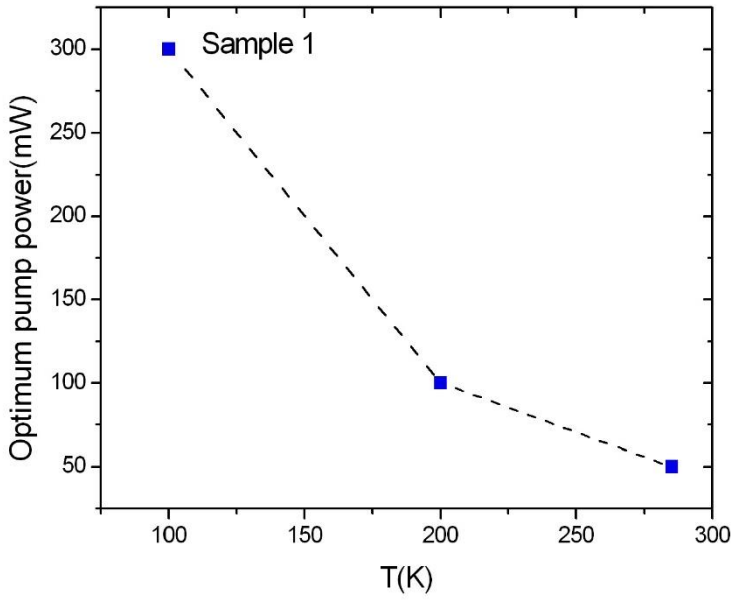

Fig.4.14. Measured optimum pump power as a function of temperature for sample 1.

For a relatively pure bulk semiconductor at a fixed temperature, the coefficients *B* and *C* are material constants. According to Eq. (4.11), the optimum pump power is directly proportional to the non-radiative recombination coefficient *A*. This means that a measurement of the optimum pump power will give a direct indication of *A* and hence EQE. This can be a very useful tool because it is possible to determine the *A* coefficient directly before implementing a time-consuming measurement of the external quantum efficiency. Testing six different GaAs heterostructures confirms that EQE scales inversely with optimum pump power (Table 4.1).

Sample number	Growth technique	Optimum Power (mW)	EQE (%)
1	MOCVD	50	96.4
2	MOCVD	50	96.9
3	MBE	100	91.0
4	MBE	200	90.0
5	MOCVD	200	87.9
6	MOCVD	200	78.0

Table.4.1. Six samples tested with optimum power and EQE shows inverse relationship.

4.3.5 Growth optimization for EQE

The fabrication of GaAs/InGaP double heterostructures (DHS) by MOCVD is not new, but laser cooling in these heterostructures is a challenging task and represents a worthwhile test of the materials and the synthesis technique. The GaAs/GaInP structure can be grown lattice matched and sufficiently high PL lifetimes have been observed to suggest they are a good candidate among III-V materials for laser cooling demonstration [64].

Our collaborators at Sandia National Laboratory (SLN) tried to precisely control of the growth sequence to reduce the interface recombination [47]. To prepare GaAs/InGaP DHS, they utilized low-pressure MOCVD at 60 Torr. Trimethyl gallium (TMGa) and trimethyl indium (TMIn) were combined with arsine or phosphine in a vertical high-speed rotating disk (1000 rpm) chamber. Two different TMGa sources allowed the GaAs growth rate to be varied independently of the need to achieve a lattice-matched GaInP composition. The temperature was controlled at 650 ℃ using

emissivity correcting pyrometry. For GaAs, a growth rate of 20 nm/min was achieved with 25 μmol/min at a V/III ratio of 50. For GaInP, a growth rate of 35 nm/min was obtained with 35 μmol/min of TMGa and 26 μmol/min of TMIn at a V/III = 160. They found the best surface morphology was obtained with GaAs (100) with a six degree miscut toward a (111)A direction. This substrate specification was used for all samples evaluated in the study below. Growth was initiated by depositing a 50 nm AlAs layer, for use in subsequent epitaxial lift off, followed by 700 nm of GaInP, 700 nm GaAs, and 700 nm of GaInP. The wafer was cooled to 300 ℃ before the PH_3 flow was terminated. The GaInP barriers were doped with silicon to a level of 2 x 10^{17} cm^{-3}, while the GaAs layer was not intentionally doped with an n-type background of 1 x 10^{15} cm^{-3}.

Their initial experimental efforts deposited GaAs and InGaP heterostructure continuously, without acknowledgment of the chemical differences between compounds. This growth sequence is illustrated in Fig.4.15(a). The reality is much more complex. Chemical exchange leads to unintended composition grading over short distances between these two compounds [88-90]. They observed this dramatically as significant compressive strain in what should be lattice matched superlattice structures. To avoid this grading, a thin GaP layer was inserted between the inverted interface, going from GaInP to GaAs as illustrated in Fig.4.15(b) [91, 92]. GaP is under significant tensile strain grown on GaAs or lattice matched GaInP so only very thin layers can be used. They grew nominally 0.6 nm, but did not attempt to characterize this thickness. This insertion eliminated the compressive stress observed in the GaAs/GaInP superlattices. The only interface they impacted was the inverted one; the

regular GaAs to GaInP interface was grown continuously without any adjustment. This is in contrast to other reports that perform treatments on both interfaces [93, 94]. They speculate that the inverted interface undergoes significant intermixing on the anion sub-lattice and indium segregation, while the regular interface is well ordered [95].

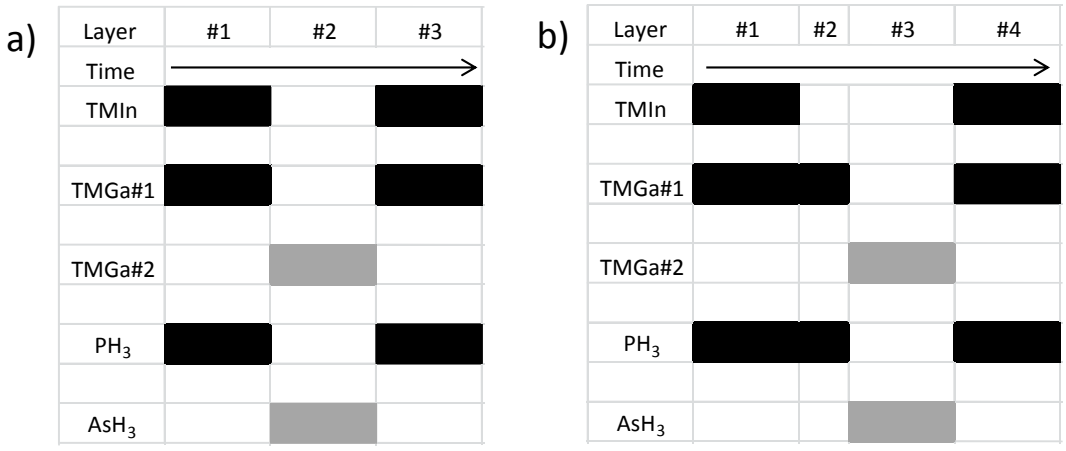

Fig.4.15. Illustrations of the growth sequences used for a) Sample 1 and b) Sample 2. In b) A thin GaP layer is introduced between the lower barrier and the active GaAs layer. The time dimension is not drawn to scale for illustration purposes.

To characterize the MOCVD candidate laser cooling GaAs/GaInP double heterostructures prior to a cooling attempt they temporally and spectrally resolve photoluminescence (PL) emission. A CW diode laser operating at 785 nm is routed through a fiber optic illuminating the sample. Photoluminescence is collected through the same fiber which is bifurcated sending a fraction of the collected PL to a scanning monochromator for spectral detection. Fig.4.16(a) illustrates the results of the characterization for the growth conditions detailed in Fig.4.15. Room temperature PL from sample 2 exhibits a much smoother spectrum below the band edge, Fig.4.16(a,

black line). In contrast, PL from sample 1, Fig.4.16(a, red line), shows an extended pedestal below the gap arising from the lack of an intermediate GaP layer on the inverted GaAs/GaInP interface. The existence of this pedestal indicates the presence of states not associated with bulk GaAs. They believe these states lead to non-negligible background absorption when pumping below the bandgap where the resonant absorption is rapidly diminishing.

In a second series of measurements they use a pulsed laser diode (λ = 785 nm, 58 ps duration and 5.5 pJ per pulse) operating at 25 kHz to illuminate the GaAs layer. A collection fiber is placed in front of the sample and off axis relative to the excitation laser to avoid collection of reflected laser light. Gathered PL emitting from the opposite end of the collection fiber is collimated and sent through a 785 nm notch filter to remove any residual laser light and subsequently detected with a photomultiplier tube (PMT) (Hamamatsu H10721-20). The time-resolved decay is spectrally integrated and averaged on an oscilloscope. They fit the late-time tail of the photoluminescence decay tail to avoid contribution from Auger and radiative recombination mechanisms present in GaAs at high carrier concentration. Fitting with a single exponential indicates minimal contribution from these nonlinear terms and gives the non-radiative recombination lifetime [44].

Time resolved PL from samples 1 and 2 is presented in Fig.4.16(b, red and black lines respectively). With judicious treatment of the inverted GaAs/GaInP interface, nonradiative lifetime in excess of 21 μs can be achieved, Fig.4.16(b, black line). Without an optimized interface, the non-radiative recombination rate increases

and lifetimes can drop by more than an order of magnitude. An example of this reduction is observed in Fig.4.16(b, red line).

Based on the temporal-spectral PL characterization, sample 1 is a more favorable candidate for laser cooling. Fig.4.17 shows All-optical Scanning Laser Calorimetry (ASLC) data. The linear fit to data points above the band edge (>1.50 eV) gives a record high EQE of $99.5 \pm 0.1\%$, Fig.4.17 (solid line). This is the highest EQE ever recorded in GaAs semiconductor bulk crystals.

Through precise control of the growth sequence, improved crystallographic order at the inverted GaAs/GaInP heterojunction results in high EQE. This improvement in EQE comes via a reduction in interface recombination.

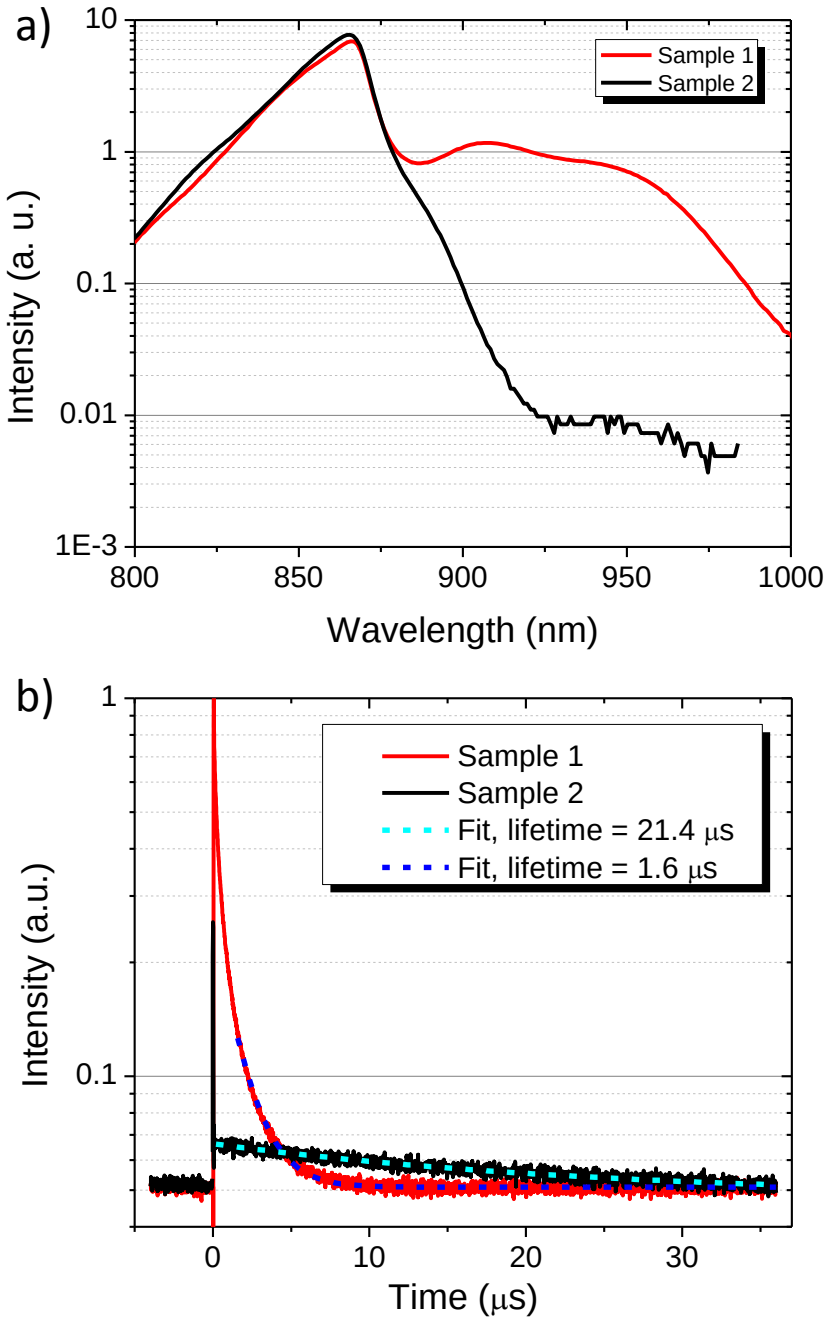

Fig.4.16. (a) PL spectra collected from samples with the growth conditions of Fig.4.15. The pronounced pedestal of sample 1 (red line) indicates states below the bandgap arising from the lack of an intermediate GaP layer. (b) PL lifetimes for the two samples in (a). Measured data (solid lines) and single exponential fits (dashed lines) show a large difference in nonradiative lifetime.

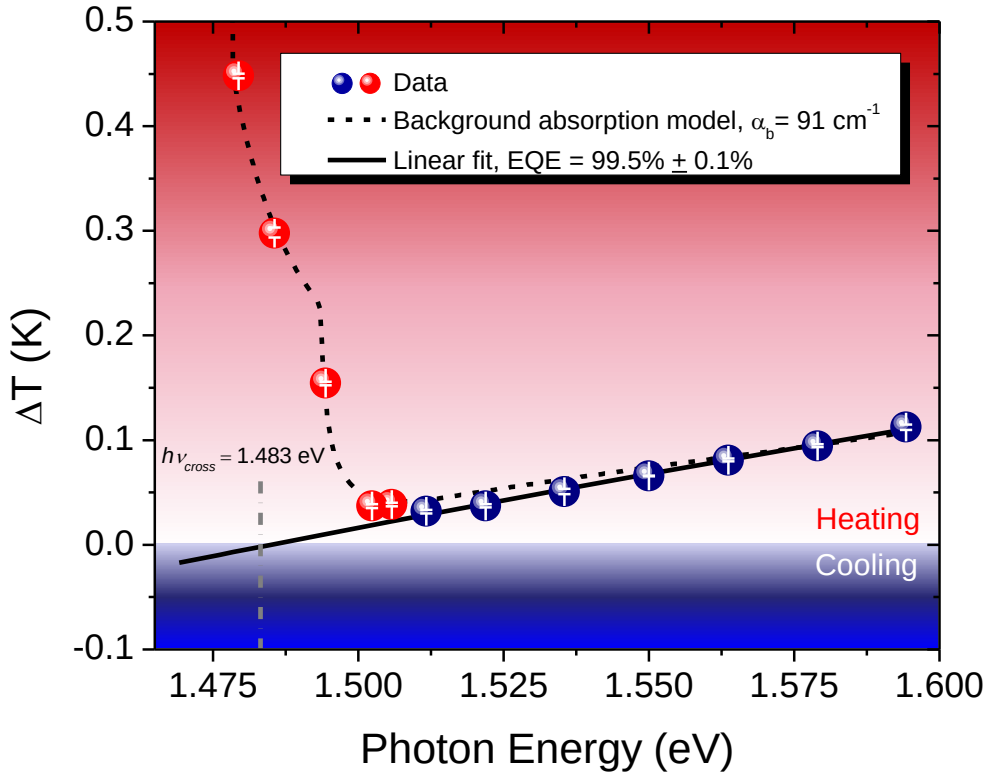

Fig.4.17. Laser cooling attempt of GaAs performed at 100 K. Data used in EQE fitting, blue spheres. Each data point is the average of three measurements. Error bars represent measurement spread. EQE fit to data giving a record EQE of 99.5% (solid line). Data in red spheres is used in fitting the background absorption model of Eq. (4.9). The resultant fit is shown (dashed line). Sample bandgap is 1.50 eV.

4.3.6 Investigation of background absorption

Even though we optimize the growth condition and carrier density and perform the cooling experiment at a favorable temperature, net cooling, however, has still not been observed because of residual background absorption in the GaAs/GaInP interface, GaInP/ZnS bonding interface, GaInP/air interface, bulk GaAs layer or bulk passivation

GaInP layer. We can set Eq. (4.9) equal to zero and solve for the α_b term to yield the maximum tolerable background absorption to reach zero-crossing. Given the EQE of 99.5%, $\alpha_b^{\max}$ = 0.19 cm^{-1} for pumping $k_B T$ below the mean fluorescent energy. These values are in good agreement with the theoretical analysis from Ref. [5]. With unity EQE and pumping $k_B T$ below $h\tilde{\nu}_f$ the maximum tolerable background absorption to achieve cooling would be 1.44 cm^{-1}, considerably lower than the experimentally determined 91cm^{-1}.

Identifying the source of this absorption is a challenging problem. From all the ASLC results in Appendix A, we cannot find a direct correlation between EQE and background absorption. That is, improving EQE does not necessarily lower background absorption and vice versa.

To investigate the wavelength dependence of the background absorption, we perform an experiment to measure the temperature change of the sample using DLT technique under constant pump power for a wide range of wavelengths below bandgap. The temperature change is directly related to the absorbed power of the sample at a particular wavelength. The pump source is the same home-built tunable Ti:Sapphire laser used in ASLC. Since the mirror set used for ASLC only covers wavelength range of 740nm-950nm, we did a second experiment, using a different mirror set, to cover wavelength range of 930nm-1080nm. The experiment was done at 100K on a typical laser cooling DHS sample bonded on a ZnS hemisphere lens. As shown in Fig.4.18, the absorption shows little dependence for a wide range of wavelengths below bandgap (above 830nm for GaAs at 100K). The modulation of absorption as seen in Fig.4.18 is

caused by the etalon effect from the thin layer of the DHS, which fits well with simulation. The lack of dependence on wavelength make it difficult for us to identify the source for the background absorption.

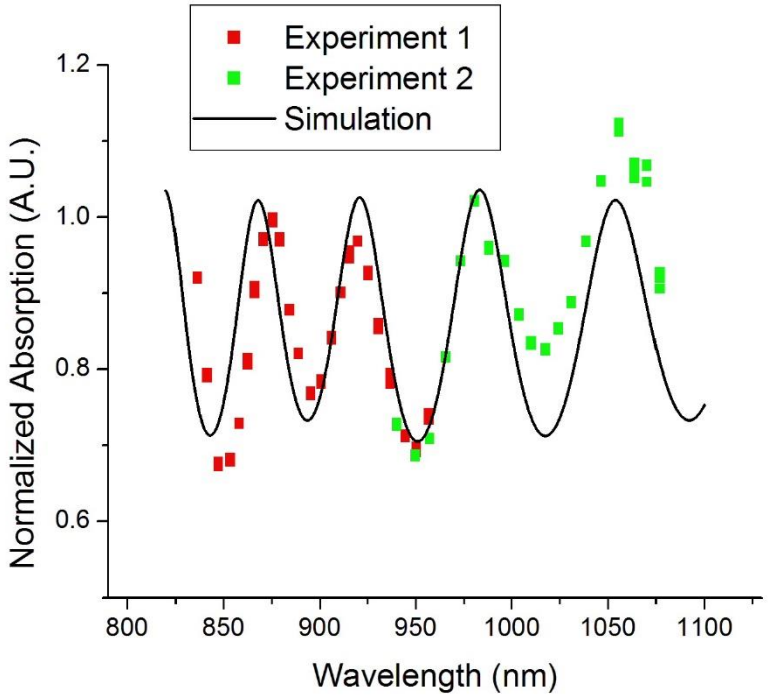

Fig.4.18. Parasitic background absorption as a function of wavelength. Data is combined with two separate experiments using different mirror sets. The modulation of absorption is explained by the etalon effect of the thin GaAs DHS sample, which fits well with simulation. Apart from that effect, the absorption shows little wavelength dependency.

As mentioned above, the possible sconces of background absorption comes from GaAs/GaInP interface, GaInP/ZnS bonding interface, GaInP/air interface, bulk GaAs layer or bulk passivation GaInP layer. To narrow down the possible causes, samples grown with different thicknesses for GaAs active layer and GaInP passivation

layers (See Fig.4.19) are tested by ASLC and compared with typical samples. The results are summarized in Table.4.2.

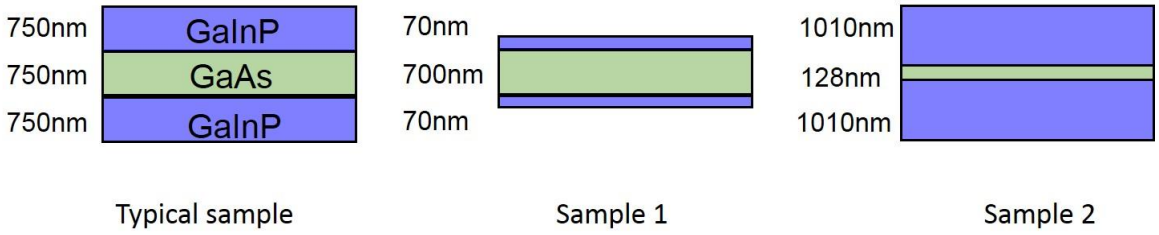

Fig.4.19. Sample structure used for investigating the source of background absorption.

	Typical samples (22 measurements in total)	Sample 1	Sample 2
Background Absorption (cm^{-1})	53	100	150

Table.4.2. Results of background absorption by ASLC on samples in Fig.4.19.

The passivation layer thickness is 10 times smaller in sample 1 than typical samples. If the background absorption comes from InGaP passivation layers, the value we get from ASLC for sample 1 is expected to be also 10 times smaller. The measured value shows the same order of magnitude compared to typical samples (averaged from 22 separate measurements), which rules out the passivation layers as the source for the background absorption.

The active layer thickness is 6 times smaller in sample 2 than typical samples. If the background absorption comes from GaAs active layers, the value we get from

ASLC is expected to be the same. If it comes from elsewhere, it is expected to be 6 times larger. The measured value is about 3 times larger than typical samples and the largest ever measured. Even though it is not conclusive, the GaAs active layer is not likely to be the source for the background absorption.

Two-color thermal Z-scan measurement is also performed by Nathan Giannini to independently verify the value of background absorption [96]. Two-color thermal Z-scan [97, 98] is a technique that measures beam transmission as a function of the refractive index of the sample. It involves using a pump beam that is absorbed by the sample, creating a thermal gradient, which then corresponds to a refractive index gradient. This index gradient is then probed by a laser at a wavelength well outside the bandgap. The index gradient acts like a lens and depending on the position of the sample with respect to the probe's focus, will weakly focus/ defocus the probe beam at the detector. This causes an increase/ decrease in the measured strength of the probe. Scanning this effect in Z direction then creates a signal that varies in strength over the scanning range. The setup for two-color thermal Z-scan measurement is shown in Fig.4.20.

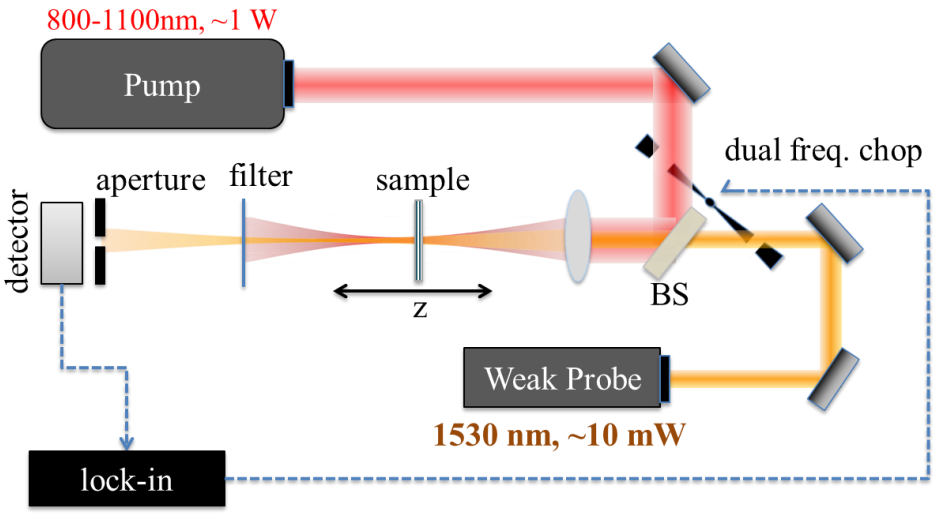

Fig.4.20. Experimental setup for two-color thermal Z-scan.

For our experiment, we used two reference samples, 15% doped Yb:YLF of length 3mm and a GaP sample of length 0.5 mm, to increase the accuracy of the measurement. We used a technique called double chopping, where the pump and probe are chopped at different frequencies. The lock-in is then set to the difference of these two frequencies, 17 Hz in our case, giving an enhancement to the signal to noise ratio of our measurements. A 1530nm fiber coupled diode laser served as our probe laser. As a pump, we used a tunable Ti:Sapphire laser.

Performing such measurements gives a background absorption value of to 98.1 ± 11 cm^{-1} for sample 2 and 12.7 ± 1.6 cm^{-1} for a typical sample. This result is consistent with ASLC and indicates that GaAs active layer is not the source for background absorption.

In addition, Z-scan measurement is taken on a double-side polished bare GaAs wafer, showing very small background absorption (~0.06cm^{-1}), which further rules out the GaAs layer as the source for background absorption.

At present, the origin of background absorption in InGaP/GaAs/InGaP DHS cooling samples is still unknown. Based on the current data, the next focus will be investigating the interfaces as the source for the background absorption. Net cooling will only be achievable by identifying and significantly reducing the background absorption.

4.4 Conclusion

In summary, we have shown that All-optical Scanning Laser Calorimetry (ASLC) can characterize the performance and efficiency of photonic devices made from high quality GaAs heterostructures. This is a relatively simple experiment procedure that can directly deduce the external quantum efficiency of a photonic device – a parameter that incorporates internal quantum efficiency and light-coupling efficiency. We describe an all-optical temperature measurement technique (differential luminescence thermometry) in which changes in the luminescence spectrum provide a direct measure of temperature. Performance is optimized at a specific photo-excitation level that can be determined in independent photo-luminescence measurements. We have presented results obtained with GaAs, but emphasize that the concepts have general validity and can be applied to other systems.

Through precise control of the growth sequence, improved crystallographic order at the inverted GaAs/GaInP heterojunction results in record high EQE but net cooling is still not observed due to the existence of high parasitic background absorption. Progress have been made on identifying the source for background absorption but more work is needed in the future.

Chapter 5

Power-Dependent Photo Luminescence Measurement

Photoluminescence is an established non-destructive spectroscopic technique for analyzing the properties of semiconductors. A general introduction can be found in the review paper [99]. The relation between excitation density and integrated photoluminescence can identify different recombination mechanisms [100, 101].

In Chapter 4, we have shown that PDPL measurement can be used to determine the optimum power or optimum carrier density for the external quantum efficiency (EQE) of the cooling sample. In this chapter, we further develop the PDPL technique and make it a useful tool to rapidly screen the semiconductor cooling samples before commencing complicated fabrication procedures.

5.1 Low carrier density PDPL

In this section, we show that PDPL technique in the low excitation range can be combined with time-resolved photoluminescence (TRPL) measurement to obtain the

non-radiative decay coefficient. This will allow us to screen the samples prior to processing (patterning and liftoff) more rapidly.

Note that in the low excitation regime, however, the recombination processes is not necessarily determined by the non-radiative *A* term but may be dominated by impurity meditated radiative recombination.

In this case, the rate equation for electron-hole pairs is given by:

$$\frac{dN}{dt} = \frac{\alpha_r I}{h\nu} - (A + \eta_e B N_d)N - \eta_e B N^2 - CN^3 \tag{5.1}$$

where N is the photo-excitation density, N_d is the impurity (donor or acceptor) density and I is the pump intensity. We have ignored impurity mediated Auger recombination by assuming low enough doping concentrations: $N_d << N_{opt}$.

The various recombination pathways are isolated using spectrally-integrated, time-resolved PL (TRPL) after pulsed excitation [44]. Note there are two terms that are first-order in N. At late times where $N << N_d$, the carrier density rate equation is dominated by the sum of the non-radiative recombination and impurity mediated luminescence:

$$\frac{dN}{dt} = -(A + \eta_e B N_d)N \tag{5.2}$$

The solution for N is exponential decay

$$N(t) = N_0 e^{-t/\tau} \tag{5.3}$$

where N_0 is the initial photo-injected carrier density and the photoluminescence lifetime has the form:

$$\tau = \frac{1}{A + \eta_e B N_d} \tag{5.4}$$

Separation of A and N_d requires a second, independent measurement that is accomplished by PDPL. The spectrally-integrated photoluminescence power density P_{lum} is related to the radiative parts of Eq. (5.1) by:

$$P_{lum} = h\tilde{\nu}_f \eta_e B(N(t)^2 + N_d N(t)) \tag{5.5}$$

At steady-state and assuming the excitation is low enough to ignore Auger recombination, Eq. (5.1) reduces to:

$$\frac{\alpha_r I}{h\nu} = (A + \eta_e B N_d) N + \eta_e B N^2 \tag{5.6}$$

Substituting the solution of N into Eq. (5.5) followed by some algebraic simplification gives:

$$\frac{P_{lum}}{\alpha_r I} = \frac{P_{lum}}{P_{abs}} \propto 1 - 2(1 - \eta_d) \frac{\sqrt{\overline{P_d} + 1} - 1}{\overline{P_d}} \tag{5.7}$$

where $\overline{P}_d = P_{abs} / P_d$ is the normalized absorbed laser power (density), and the expression on left hand side is defined as the normalized luminescence efficiency η_L with the dopant characteristic power density and efficiency defined as:

$$P_d = \frac{(A + \eta_e B N_d)^2 h\nu}{4\eta_e B} \tag{5.8}$$

and

$$\eta_d = \frac{\eta_e B N_d}{A + \eta_e B N_d} \tag{5.9}$$

Eq. (5.7) is plotted on a log-log scale in Fig.5.1 for η_d values in the range 0.1--1.0. A PDPL experiment requires that the pump power be varied over many orders of magnitude to resolve the features shown in Fig.5.1. After normalization, the curve will approach the value of η_d at sufficiently weak pumping.

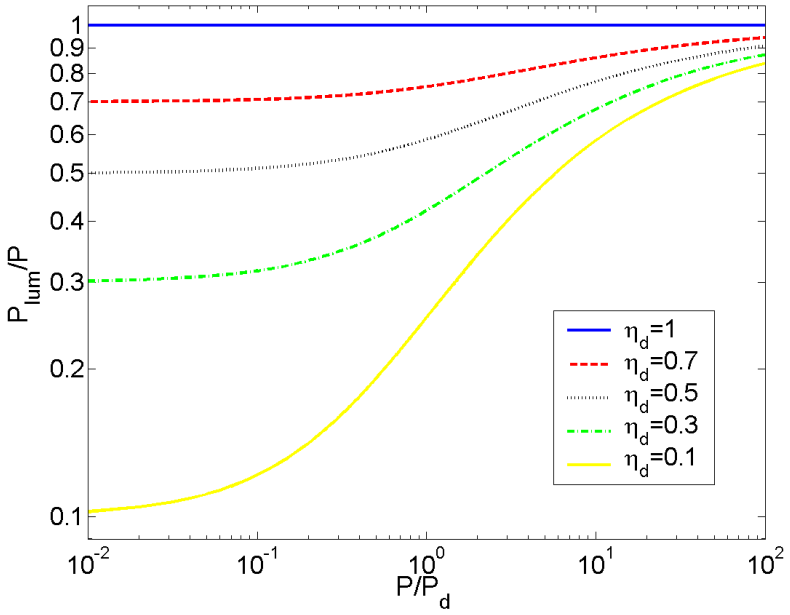

Fig.5.1. Theoretical low carrier density PDPL curves for different dopant luminescence efficiencies η_d.

Eqs. (4.14) and (5.7) are both approximate solutions pertaining to the two extreme cases of high and low density excitations, respectively. An exact solution covering the full power range is possible and requires finding the roots of a third-order polynomial. For comparison, we plot the results of Eq. (4.14) & (4.18), and Eq. (5.7), together with the results of exact calculations for a particular case in Fig.5.2.

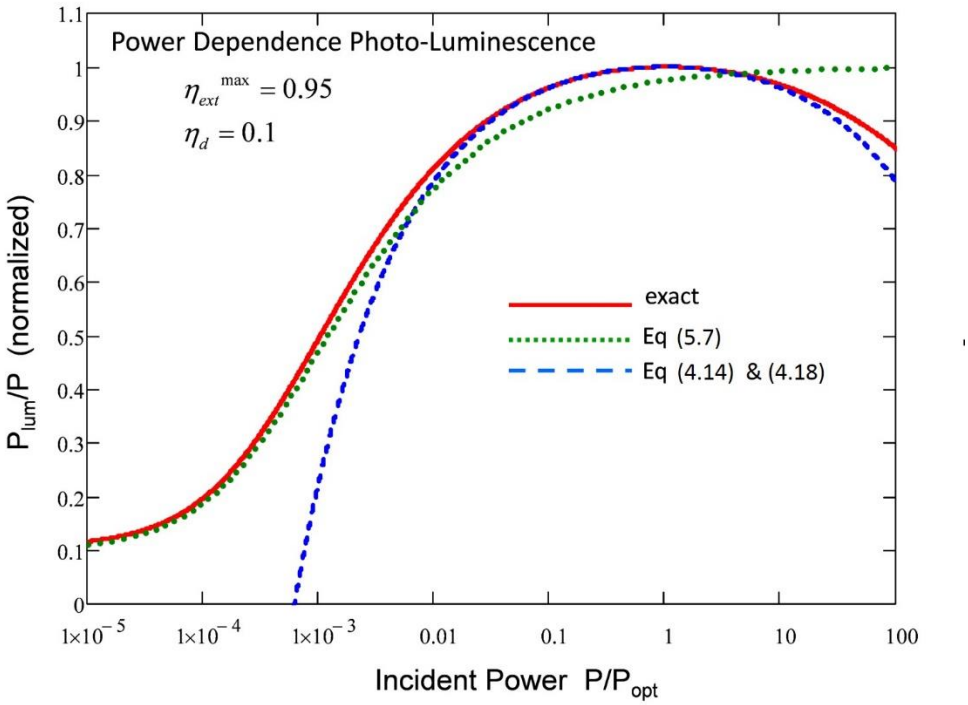

Fig.5.2. Normalized PL power versus incident excitation power calculated using approximate and exact solutions.

It should be noted that the incident power in Fig.5.2 (x-axis) is normalized to the optimum power (P_{opt}). Thus comparisons to Fig.5.1 (normalized to P_d) should be made accordingly.

We perform a number of low-density PDPL/TRPL experiments on various InGaP/GaAs/InGaP double heterostructures at room temperature. For the PDPL, we use a CW diode laser (λ= 780 nm) chopped at 250Hz for carrier excitation. The PL is collected using a photo-multiplier tube with the help of lock-in detection (Fig.5.3). The collected data is then normalized and fitted using Eq. (5.7) with coefficients η_d and P_d as the fitting parameters.

Time resolved PL data on the same sample is obtained using a pulsed diode laser (λ= 780 nm, pulse width ~5ns and repetition rate ~40 KHz) and a photo-multiplier tube. Time constant τ is obtained by linear fit of the curve on a semi-log scale.

Self-consistent, simultaneous analysis of separate PDPL and TRPL experiments can quantify the coefficients A and BN_d at a specific temperature. They are obtained by simultaneous solution of Eqs. (5.4) and (5.9).

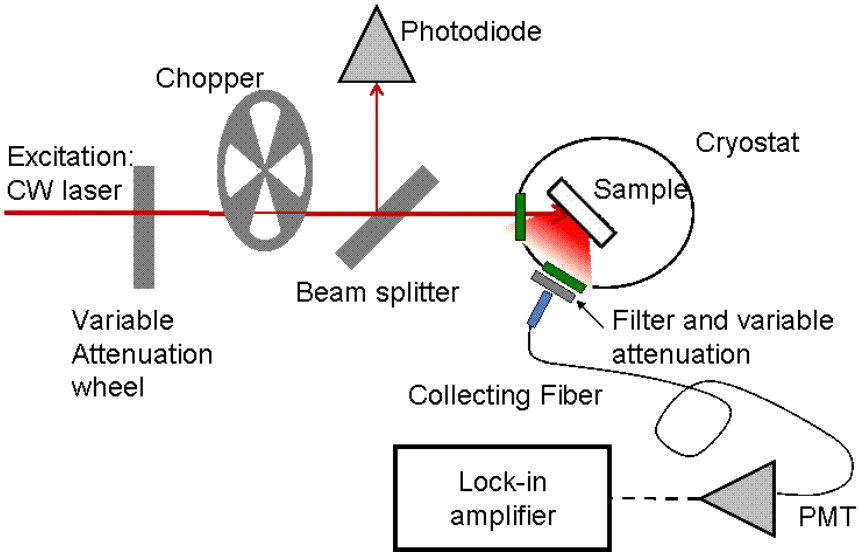

Fig.5.3. PDPL experimental setup.

Fig.5.4 shows the experimental results of two MOCVD grown (1 and 2) and two MBE grown (3 and 4) samples; results are summarized in Table.5.1. In the analysis, we take $\eta_e B = 0.75 \times 10^{-10}\ cm^3/s$ [30]. EQE is measured via All-optical Scanning Laser Calorimetry (ASLC) described in Chapter 4. We find that MBE samples have lower

impurity content and also confirm that slower non-radiative recombination rates *A* produce higher EQE.

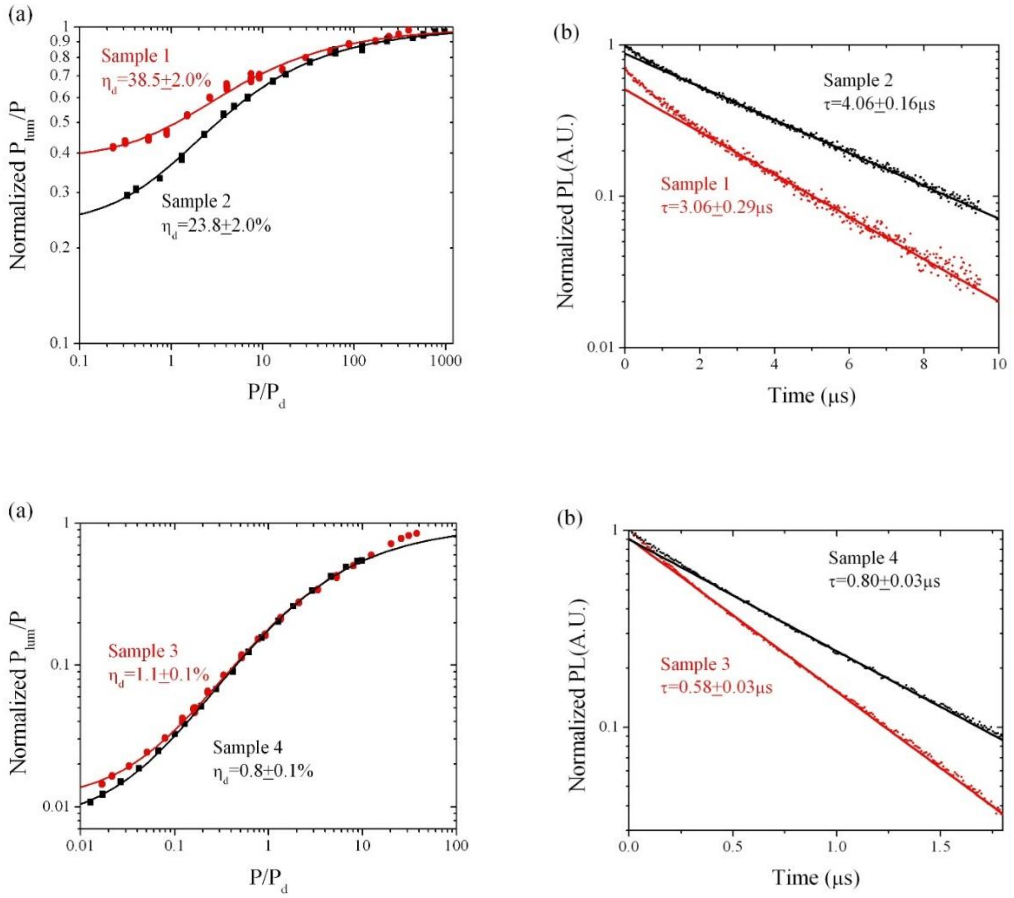

Fig.5.4. Experimental data for two MOCVD samples and two MBE samples. Sample 1 has a release layer while sample 2 does not. Sample 3 and sample 4 have different passivation layers. (a). PDPL measurements with normalized integrated PL plotted against the normalized excitation intensity. (b). time-resolved PL lifetime measurements.

Although the observed overall trend is as expected, there exist some small discrepancies where samples with larger *A* produce slightly higher η_{ext}. This is explained by sample-to-sample variations in bonding integrity at the semiconductor

dome lens interface, which affects the extraction efficiency η_e. Differences in η_e translate into difference in η_{ext}, according to Eq. (4.12). An earlier investigation [82] as well as a recent theoretical study [40] suggests that non-radiative recombination rate may also depend on the injected carrier density. The fact that we measure the EQE and lifetime at different pump intensities may explain such discrepancies.

Sample number	Growth technique	Optimum Power (mW)	EQE (%)	η_d (%)	τ (μs)	A ($1/\mu s$)	N_d ($10^{14}\ cm^{-3}$)
1	MOCVD	50	96.4	38.5 ±2.0	3.1 ±0.3	0.20 ±0.02	2.5 ±0.3
2	MOCVD	50	96.9	23.8 ±2.0	4.1 ±0.2	0.19 ±0.01	1.2 ±0.1
3	MBE	100	91.0	1.1 ±0.1	0.6 ±0.03	1.7 ±0.1	0.4 ±0.04
4	MBE	200	90.0	0.81 ±0.1	0.8 ±0.03	1.2 ±0.05	0.2 ±0.03
5	MOCVD	200	87.9	1.29 ±0.2	2.9 ±0.3	0.35 ±0.03	0.09 ±0.02
6	MOCVD	200	78.0	0.68 ±0.2	3.5 ±0.2	0.28 ±0.02	0.04 ±0.01

Table.5.1 Summary of sample parameters.

5.2 High carrier density PDPL

In Chapter 4, we use PDPL at high excitation to find the optimum pump power for EQE. We have shown that the normalized luminescence power scales directly with

EQE and shows a maximum at the optimum pump power. Normalizing to the peak of the curve, the analytical expression can be given as:

$$\frac{P_{lum}/P}{(P_{lum}/P)^{\max}} = \frac{1}{\eta_{ext}^{\max}}[1-(1-\eta_{ext}^{\max})\frac{1+\bar{P}}{2\sqrt{\bar{P}}}] \tag{5.10}$$

where

$$\bar{P} = \frac{P_{abs}}{P_{opt}} \approx \frac{N^2}{N_{opt}^2} \tag{5.11}$$

$$\eta_{ext}^{\max} = \frac{\eta_e B N_{opt}^2}{AN_{opt} + \eta_e B N_{opt}^2 + CN_{opt}^3} \approx 1 - \frac{2\sqrt{AC}}{\eta_e B} \tag{5.12}$$

$$N_{opt} = \sqrt{\frac{A}{C}} \tag{5.13}$$

This is plotted in Fig.5.2 (blue curve) and experimentally demonstrated (covered in Chapter 4).

Using Eq. (5.10), we can plot P_{lum}/P as a function of P (pump power) in semi-log scale (See Fig.5.5). After normalizing to the peak of the curve, plots of samples with different EQE show different slopes before and after the peak. We can then fit the experimental data with theory using η_{ext}^{opt} as a fitting parameter. In this way, PDPL measurement can independently provide us the optimum external quantum efficiency of the cooling sample.

Experimentally, however, we find that at low pump powers, the data obtained using this technique is very noisy. To address this, we develop a technique called Differential PDPL.

5.2.1 Differential PDPL

We combine the pump laser with a low-power diode laser modulated at ~60kHz at around the same wavelength and measure the modulated PL signal using lock-in detection. Note that the modulation frequency has to be smaller than the inverse of non-radiative lifetime, which is about ~100kHz. We call this differential PDPL. The experiment setup is shown is Fig.5.6.

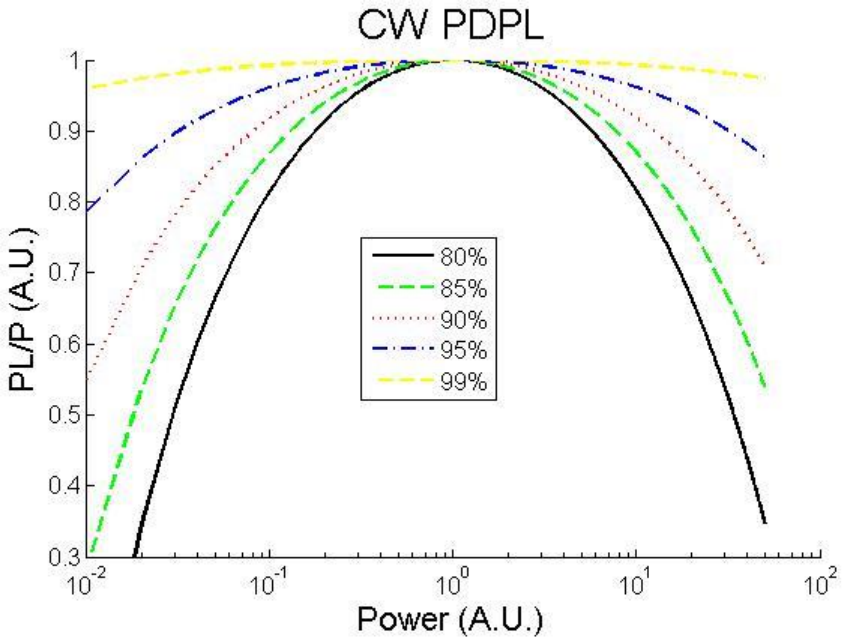

Fig.5.5. (CW) PDPL theoretical curve for different optimum external quantum efficiency.

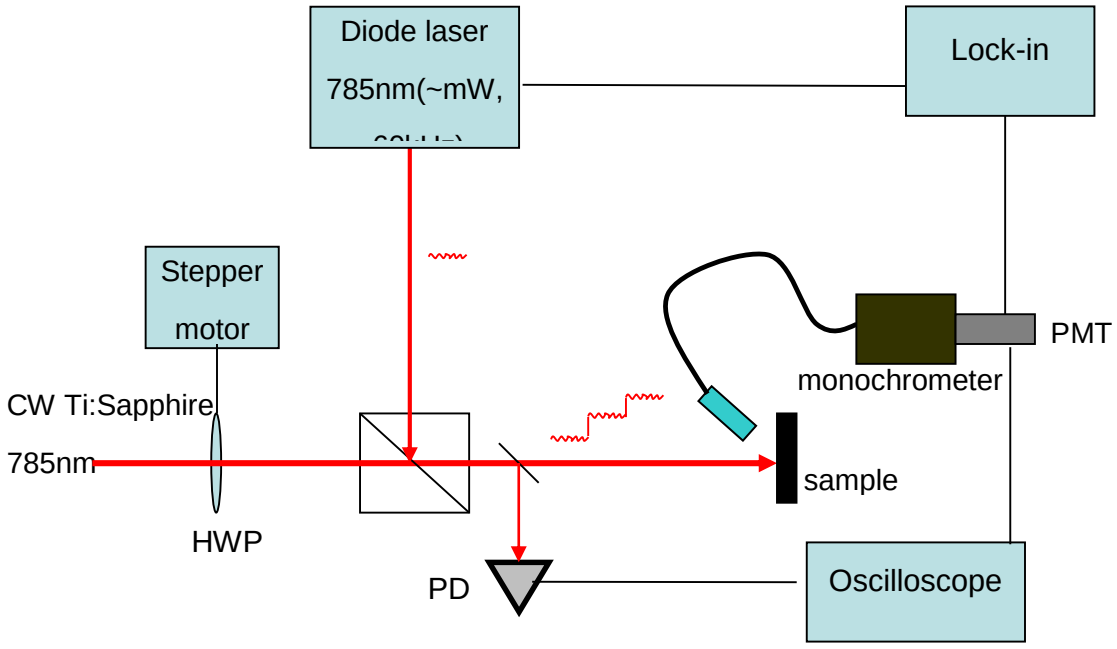

Fig.5.6. Experiment setup for differential PDPL.

The analytical expression of differential PDPL differs from conventional PDPL as:

$$\frac{dP_l}{(dP)^{\max}} = \frac{1-(1-\eta_{ext}{}^{\max})(\frac{3}{2}\sqrt{P}+\frac{1}{2\sqrt{P}})}{1-\sqrt{3}(1-\eta_{ext}{}^{\max})} \tag{5.14}$$

We plot this curve together with the conventional PDPL curve in Fig.5.7. on a semi-log scale.

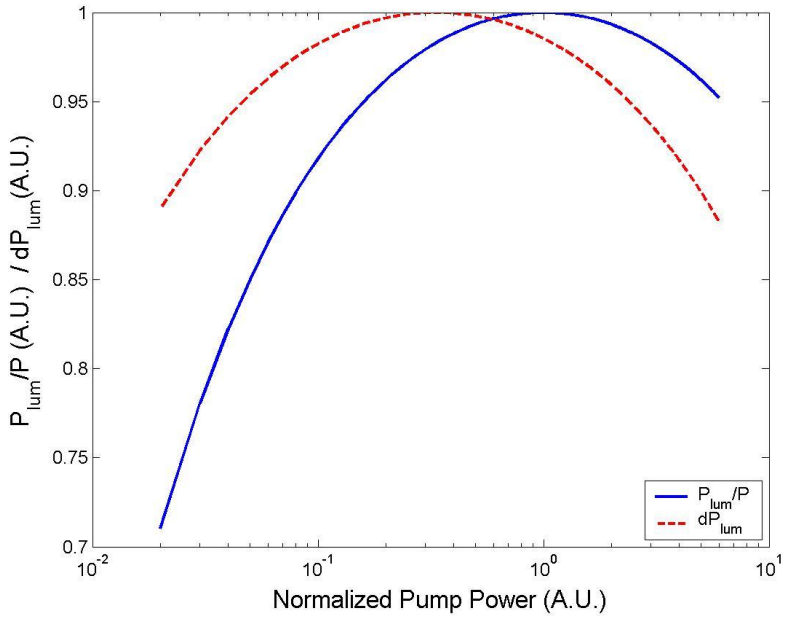

Fig.5.7. Theoretical calculation of conventional PDPL and differential PDPL, both normalized to the peak of the curve.

We notice that the peak in differential PDPL plot occurs at about one third of the power needed in conventional PDPL, which makes it easy to find and impose less risk of overheating the sample. To retrieve the EQE from the differential PDPL plot, we can simply fit the plot with the analytical form Eq. (5.14), taking η_{ext} as a fitting parameter. Even simpler, we find that at 0.075 times the peak power, the value of the differential PDPL plot roughly gives the number of EQE.

Fig.5.8 shows the experimental data and the corresponding theoretical curve. They match very well. The uncertainty of EQE in this experiment is about $\pm$1% as shown in Fig.5.8. We also compare the EQE of several different samples under the same condition by the different techniques (ALSC and differential PDPL). The results are shown in Fig.5.9. The relative value agrees with each other, while differential PDPL

consistently gives smaller EQE than Laser scanning calorimetry, which is upon further investigation.

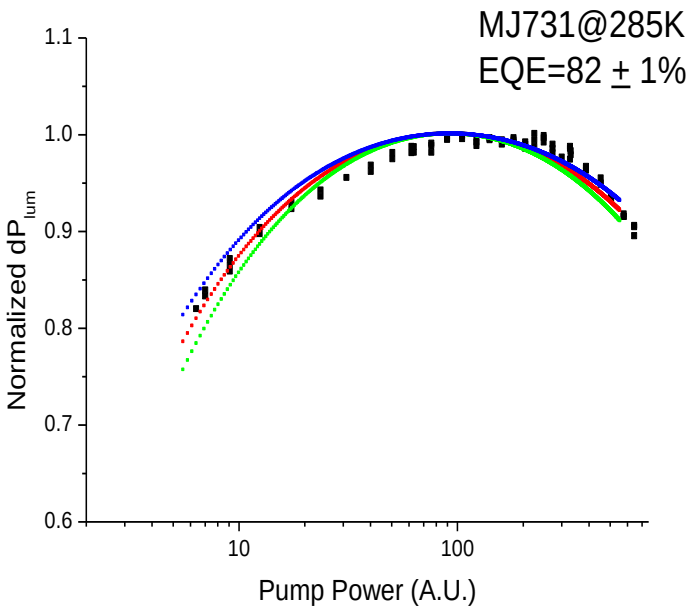

Fig.5.8. Experimental data of differential PDPL experiment. The colored lines are theoretical curve with fitting parameter of EQE as 81%, 82% and 83%, respectively. The uncertainty of this technique is about ±1%

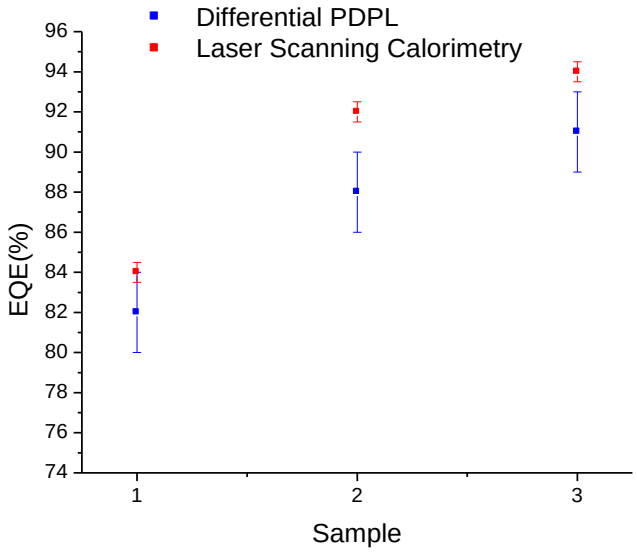

Fig.5.9. Comparison of external quantum efficiency measured by ASLC and differential PDPL under the same condition.

5.2.2 Pulsed PDPL

Temperature change of the sample was an issue in all previous PDPL experiments as a CW laser was used as a pump laser. The temperature change will then alter luminescence intensity, distorting the PDPL data. Here, we modify the previous PDPL experiment by using a pulsed laser source, which will create as much carrier density as the CW laser but generate much less heat. We call this pulsed PDPL experiment.

The analytical expression of pulsed PDPL differs from conventional CW PDPL and can be derived from the rate equation subject to an impulsively injected initial carrier density N_0:

$$\frac{dN}{dt} = -(AN + BN^2 + CN^3) \tag{5.15}$$

Rewrite the equation in the form:

$$[\frac{1}{N} - \frac{N+q}{(N-s_1)(N-s_2)}]dN = -Adt \tag{5.16}$$

where $q=B/C$, $s_{1,2} = \frac{-B \pm \sqrt{B^2 - 4AC}}{2C} = N^{opt}(\frac{-1 \pm \sqrt{1-(1-\eta_{ext}{}^{opt})^2}}{1-\eta_{ext}{}^{opt}})$ and $\eta_{ext}{}^{opt} \approx 1 - \frac{2\sqrt{AC}}{B}$,

$N^{opt} = \sqrt{\frac{A}{C}}$.

The solution of differential equation (5.16) is given by the following transcendental equation:

$$n(t)\left\{\frac{1+\frac{\sigma_1}{\varphi}}{n+\frac{\sigma_1}{\varphi}}\right\}^{\nu_1}\left\{\frac{1+\frac{\sigma_2}{\varphi}}{n+\frac{\sigma_2}{\varphi}}\right\}^{\nu_2} = \exp^{-At} \tag{5.17}$$

where we define normalized carrier density n(t)=N(t)/N$_0$, $\sigma_{1,2} = \frac{1 \mp \sqrt{1-(1-\eta_{ext}{}^{opt})^2}}{1-\eta_{ext}{}^{opt}}$,

$\nu_1 = \frac{-s_2}{s_1 - s_2} = \frac{-\sigma_2}{\sigma_1 - \sigma_2}$ $\nu_2 = \frac{-s_1}{s_2 - s_1} = \frac{-\sigma_1}{\sigma_2 - \sigma_1}$ and $\varphi = \frac{N_0}{N^{opt}}$, where N_0 is the initial carrier density at t=0.

Equation (5.17) gives the carrier density N as a function of t. We can then obtain the luminescence power by

$$P_{lum} = h\tilde{\nu}_f \eta_e \int BN(t)^2 dt \propto \int n(t)^2 dt \tag{5.18}$$

Here, we have assumed that the incident pulse is instantaneous (delta-function), thus:

$$\alpha I \Delta t = h\nu N_0 \tag{5.19}$$

where α is the resonant absorption coefficient, I is the incident pump intensity, Δt is the incident pulse duration, h is the Plank constant, ν is incident optical frequency. Since incident pump power $P = IS$, where S is the pump spot area, so $P \propto N_0$.

We plot P_{lum}/P as a function of P (pump power) for different optimum external quantum efficiency in Fig.5.10. Similar to CW PDPL, after normalizing to the peak of the curve, plots of samples with different EQE show different slopes before and after the peak. We then can use this feature to obtain the value of η_{ext}^{opt} by comparing the experimental data with the theoretical curve.

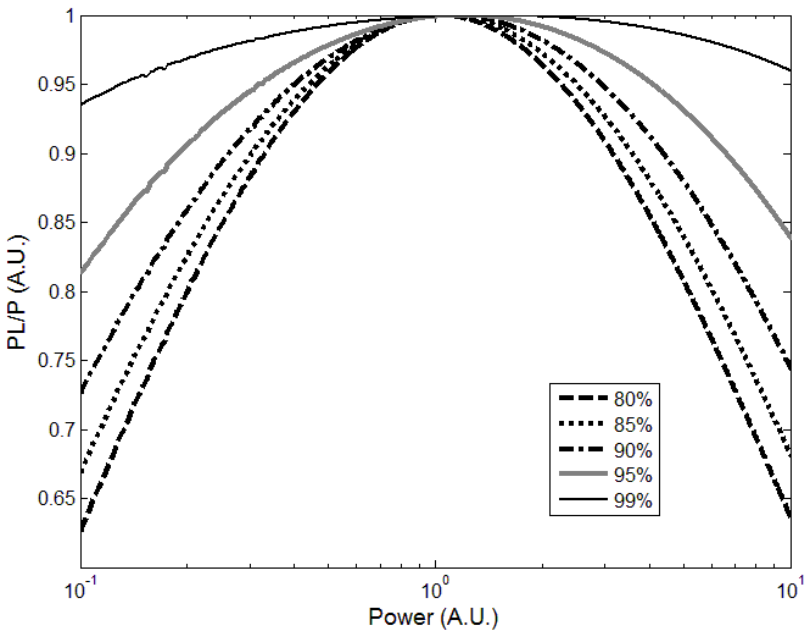

Fig.5.10. Pulsed PDPL theoretical curve for different optimum external quantum efficiency.

We also plot pulsed PDPL curve together with the CW PDPL curve for the same condition ($\eta_{ext}^{opt} = 0.9$) in Fig.5.11 for comparison.

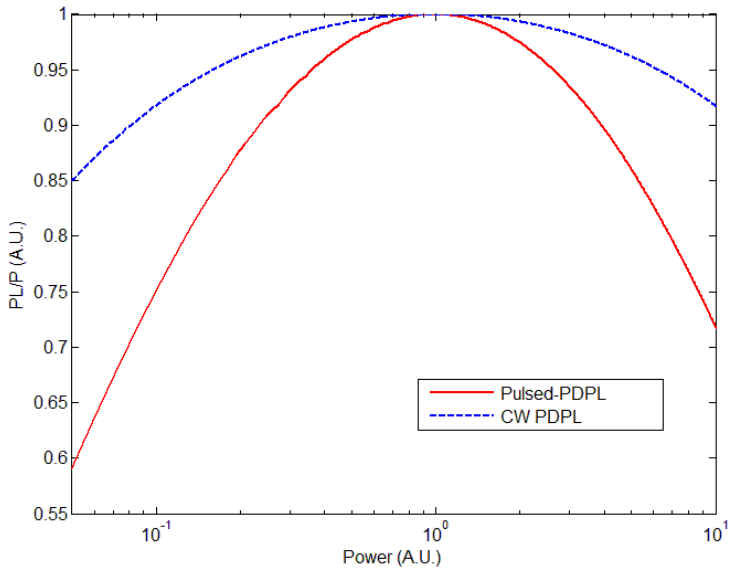

Fig.5.11. Theoretical calculation of pulsed PDPL and CW PDPL for $\eta_{ext}^{opt} = 0.9$, both normalized to the peak of the curve.

The theoretical curve of pulsed PDPL decreases faster both before and after the peak than the CW PDPL curve, which relaxes the experiment resolution.

The experimental setup is shown in Fig.5.12. We use the second harmonic of a pulsed 1535nm laser (a miniature diode-pumped Q-switched Er:YAG laser, Photop Technologies, Model DPQL-1535-C-0040-005N-03), with 5ns pulse-width and 1kHz repetition rate, as the pump source. Reference power and luminescence is collected by two identical photo-detectors. The pump light is modulated with a rotating half-wave

plate at ~1.5Hz followed by a polarizing bean-splitter to obtain nearly three orders of magnitude of extinction ratio.

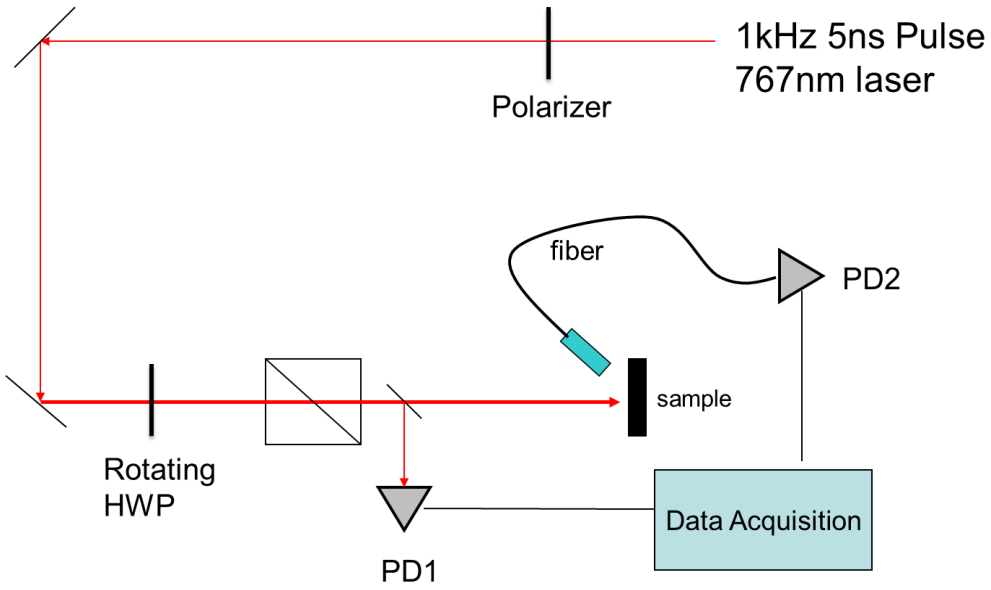

Fig.5.12. Experiment setup for pulsed PDPL.

Signals from both photo detectors are sent to an oscilloscope. The pulse stream for one cycle (or half cycle) of the modulation is then recorded and the peak signals of each pulse are picked out by a numerical algorithm using Matlab (See Fig.5.13). The ratio of the peak signals from two detectors is then plotted against the peak signals (incident power) of the reference detector (PD1).

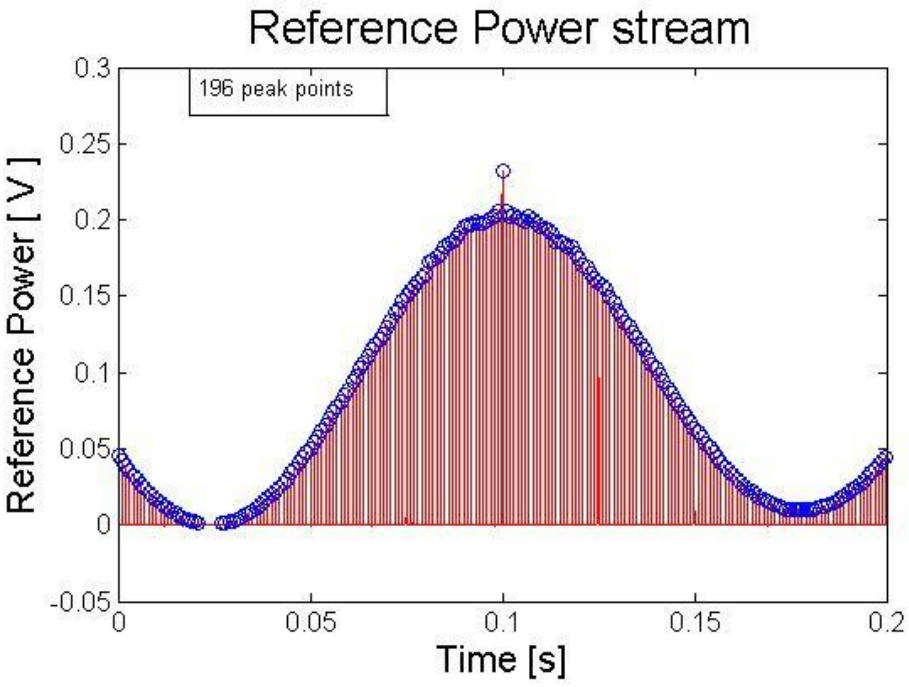

Fig.5.13. Data recorded with a typical reference pump power stream (red) and peak values obtained from algorithm (blue).

To check to validity of the setup, we first replace the semiconductor sample with a gold-plated metal piece and collected the scattered laser light from the metal piece with PD2. Neutral density filters are placed in front of the two photo detectors so that the signals from both detectors are within the same range. This is to ensure the same linearity for both detectors. The ratio of the signals from two detectors is plotted against the incident power. As shown in Fig.5.14, the ratio is flat for more than two orders of magnitude, indicating both detection arms perform identically.

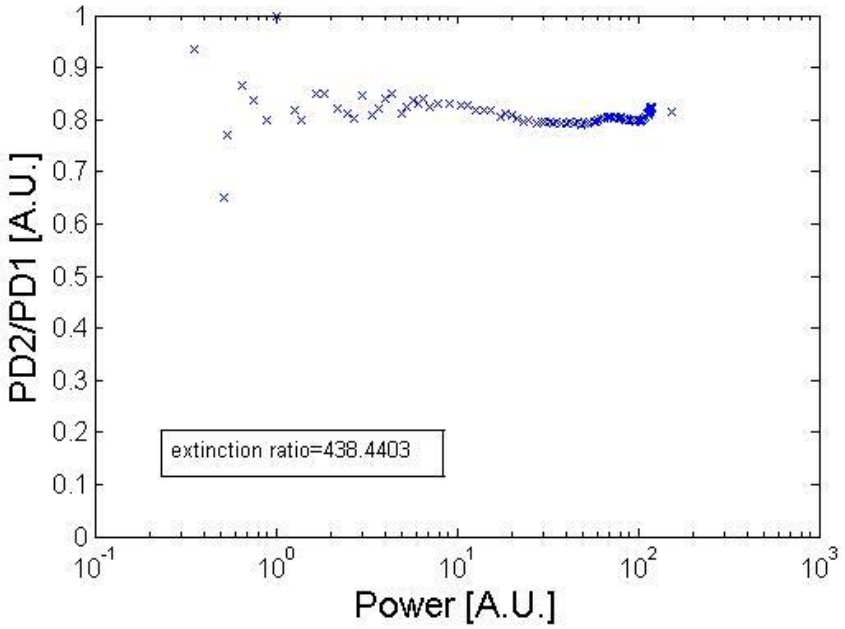

Fig.5.14. Power ratio of two detectors is flat for more than two orders of magnitude.

Fig.5.15. shows the room-temperature pulsed PDPL experimental data for two different samples with different EQE values and the corresponding theoretical curves. All samples are DHS bonded to ZnS dome lens. They both match theoretical curves very well. The uncertainty of EQE in this pulsed PDPL experiment is about $\pm$1% to $\pm$2%. We compare the EQE of several different samples under the same condition by two different techniques (ASLC and pulsed PDPL). The results are summarized in Table 5.2. The relative value agrees with each other, while pulsed PDPL consistently gives smaller EQE than ASLC. The discrepancy can be attributed to the density-dependence of radiative recombination coefficient *B* and the peak detection method used in the data processing, both of which will be discussed later in this Chapter.

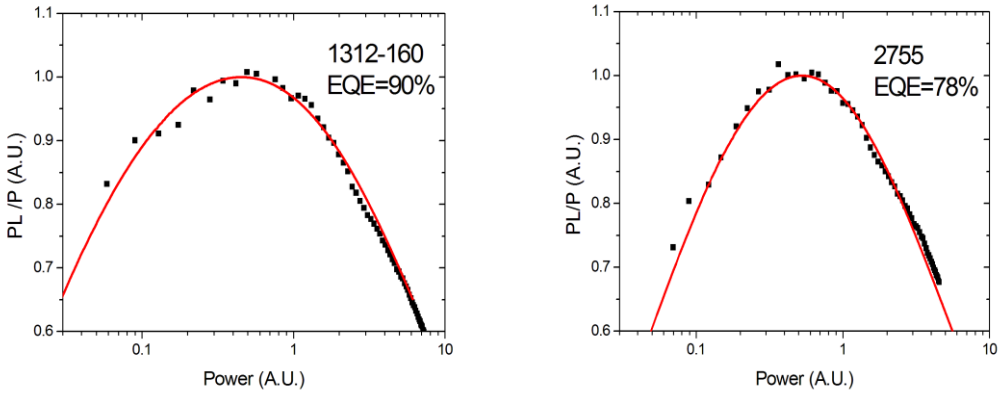

Fig.5.15. Experimental data of pulsed PDPL experiment (dots). The solid lines are theoretical curves with fitting parameter of EQE =90% and 78%, respectively. The uncertainty of this technique is about ±1%.

Sample	EQE by pulsed PDPL on bonded samples	EQE by ASLC
2755	78%	82%
1312-345	85%	86%
MF444	89%	92%
1312-160	90%	94%

Table 5.2. Comparison of external quantum efficiency measured by ASLC and pulsed PDPL under the same condition on bonded samples.

In striking contrast to the ASLC technique, PDPL can be used to easily screen samples without complicated and time-consuming lift-off processing and lens bonding. We perform pulsed PDPL on several DHS samples with substrate (before processing). Fig.5.16 shows the experimental data for two samples at room temperature and the corresponding theoretical curves. The complete results are summarized in Table.5.3 with comparison with EQE obtained from ASLC on bonded samples from the same

wafer. The EQE number obtained from PDPL on sample with substrates shows the same trend but are consistently higher than the EQE obtained from ASLC on bonded samples, which is expected since the existence of the substrate will increase the extraction efficiency of the DHS sample and thus increase EQE. The summarized data shows that in general PDPL is an accurate tool to predict the EQE and screen the sample effectively before processing.

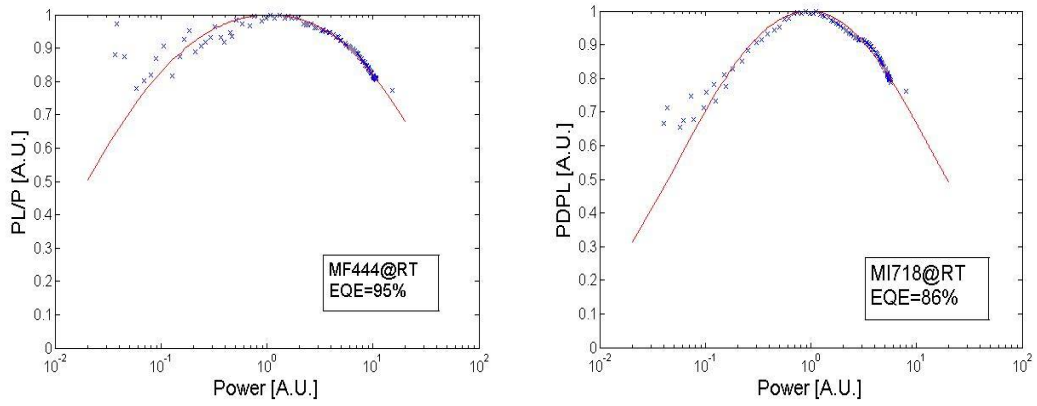

Fig.5.16. Experimental data of pulsed PDPL experiment (dots) on samples with substrate. The solid lines are theoretical curves with fitting parameter of EQE =95% and 86%, respectively.

Sample	EQE by pulsed PDPL on sample with substrate	EQE by ASLC
MF444	95%	92%
1312-160	94.5%	94%
MI718	86%	73.4%

Table 5.3. Comparison of external quantum efficiency measured by ASLC on bonded samples and pulsed PDPL on samples with substrates under the same condition.

We also perform PDPL measurement at low temperatures. However, the data at low temperatures cannot be explained completely by the analytical solution of Eq. (5.17) and Eq. (5.18). First, radiative recombination coefficient *B* is a function of carrier density; second, the peak detection method used in the data processing is different from integrating the photoluminescence over infinite time as described in Eq.(5.18). Both factors have a stronger influence at low temperatures. Therefore, we simulate the problem numerically at low temperatures.

As introduced in Chapter 2, the density-dependence of resonant absorption coefficient α results from both Coulomb screening and band-blocking (saturation) effects. The latter can be approximated by a blocking factor such that [53]:

$$\alpha(\nu, N) = \alpha_0(\nu)\{f_v - f_c\} \tag{2.46}$$

The strongly density-dependent blocking factor in the brackets contains Fermi-Dirac distribution functions for the valence (f_v) and conduction (f_c) bands. Using the "non-equilibrium" van Roosbroeck-Shockley relation, the luminescence spectral density *R* is related to the absorption coefficient [53]:

$$R(\nu, N) = \frac{8\pi n^2 \nu^2}{c^2}\alpha(\nu, N)\left\{\frac{f_c(1-f_v)}{f_v - f_c}\right\} \tag{5.20}$$

where *c* is the speed of light and *n* is the index of refraction.

Note that the radiative recombination coefficient *B* is obtained by $BN^2 = \int R(\nu)d\nu$ which results in a dependence of *B* on *N* at the high carrier densities.

In our application, we use an empirical form for the temperature and density-dependent *B* coefficient:

$$B = \frac{5.5\times10^{-10}(\frac{300}{T})^{2.5}}{1+[\frac{N}{1.5\times10^{19}(\frac{T}{300})^{10}}]^{0.5}} \tag{5.21}$$

The empirical form is based on the calculations from plasma theory of Banyai and Koch [65, 66]. The parameters in this empirical equation are determined by fitting it with the pulsed PDPL data at various temperatures. Eq. (5.21) is plotted in Fig.5.17 for 300K and 100K.

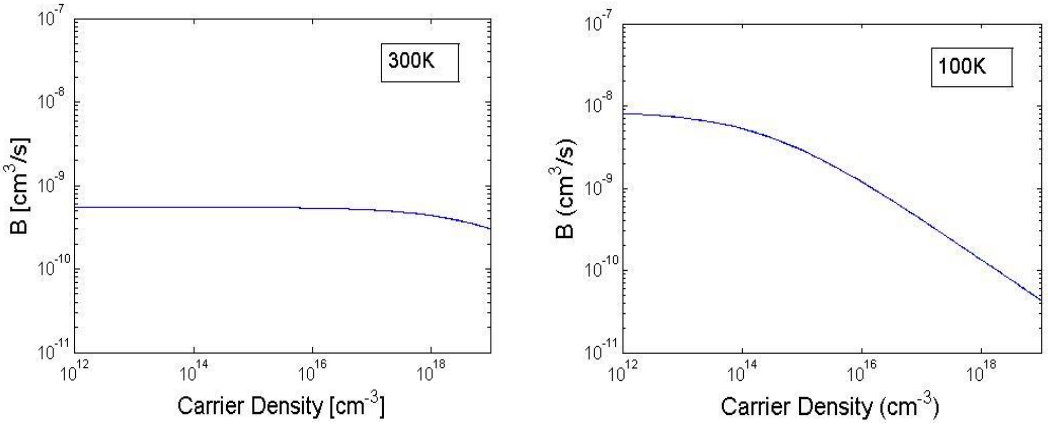

(a) (b)

Fig.5.17. Density-dependent *B* coefficient at 300K (a) and 100K (b) used to fit the PDPL measurement data.

Rupper *et al.* [31] have studied the density dependence of *B* coefficient using different models of rigorous microscopic theory. Their result at 300K is shown in Fig.5.18. It is consistent with our empirical form plotted in Fig.5.17. Their results at 100K is unavailable.

To reflect the actual peak detection method used in current data processing, we calculate the time-dependent detector signal using:

$$V(t) = \int_0^t PL(t')e^{\frac{-(t-t')}{\tau}} dt' \tag{5.22}$$

where *PL(t')* is time-dependent photo luminescence signal calculated from Eq. (5.17), and τ is the detector rise time. We then find the maximum (peak) value of *V(t)*.

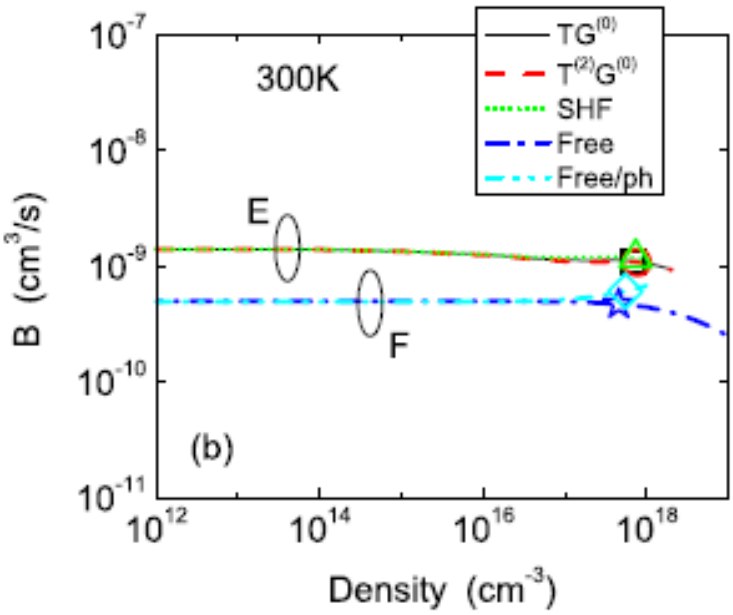

Fig.5.18. (Color online) The density-dependent radiative recombination coefficient for 300K calculated using several different models. Group "E" comprises several excitonic models: full T-matrix ($TG^{(0)}$), second-order T-matrix ($T^{(2)}G^{(0)}$), and screened Hartree-Fock (SHF) model. Group "F" contains models without e-h Coulomb interaction: "free" and "free with phonons" ("Free/ph") [31].

Fig.5.19 shows the results for both the numerical simulation and analytical solution at room temperature and 100K under the same condition. Note that numerical results also considered the pulse shape of the incident laser while analytical solution assumes a delta-function pulse. The results at 300K show very little difference, indicating that our previous fit using analytical solution are generally valid at room temperature. If using numerical simulation instead at room temperature, the obtained

optimum EQE value will be slightly higher than the ones obtained from analytical equations, which explains the discrepancies we observed earlier. The results, however, differ a lot at 100K, warranting the use of numerical simulation at low temperatures.

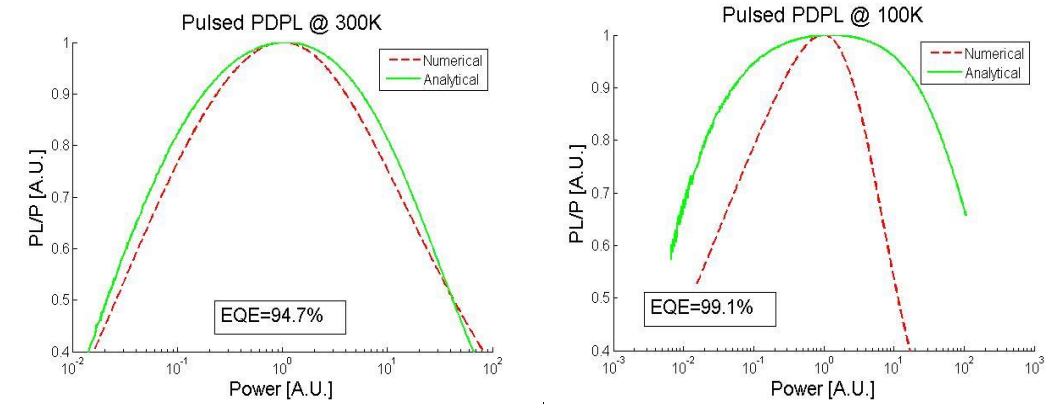

(a) (b)

Fig.5.19. Calculated PDPL curve from analytical solution (green) using Eq. (5.17) and (5.18) and from numerical simulation (red) at (a) 300K and (b) 100K.

Fig.5.20 shows the experimental data at 100K, 200K and room temperature for one cooling sample before processing and the corresponding numerical simulation curve. They match very well and the obtained EQE values are in general consistent with ALSC measurement at low temperatures on the same sample.

We can also plot the numerical simulation results for various temperatures in one plot without normalizing the pump power (See Fig.5.21). Fig.5.21 shows that the optimum pump power decreases with deceasing temperature, which is consistent with both theory and experimental observation.

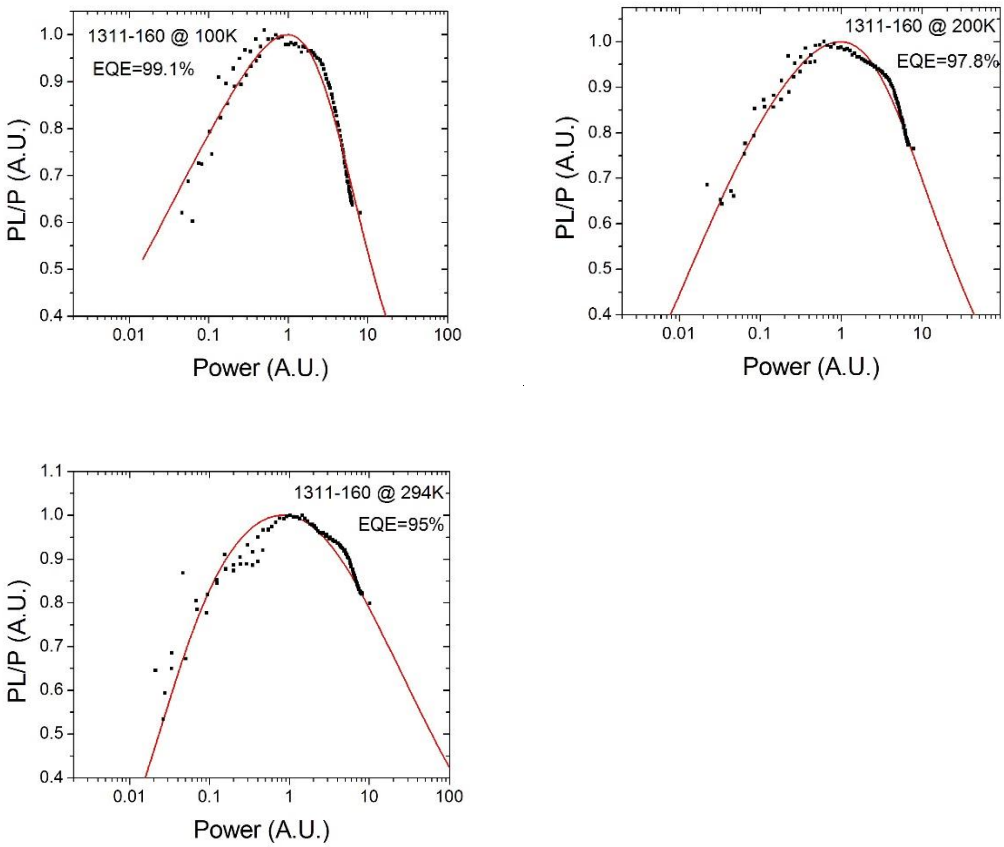

Fig.5.20. Experimental data of pulsed PDPL experiment (dots) on samples with substrate at different temperatures. The solid lines are simulation curves with fitting parameter of EQE =99.1% at 100K, 97.8% at 200K and 95% at 294K, respectively.

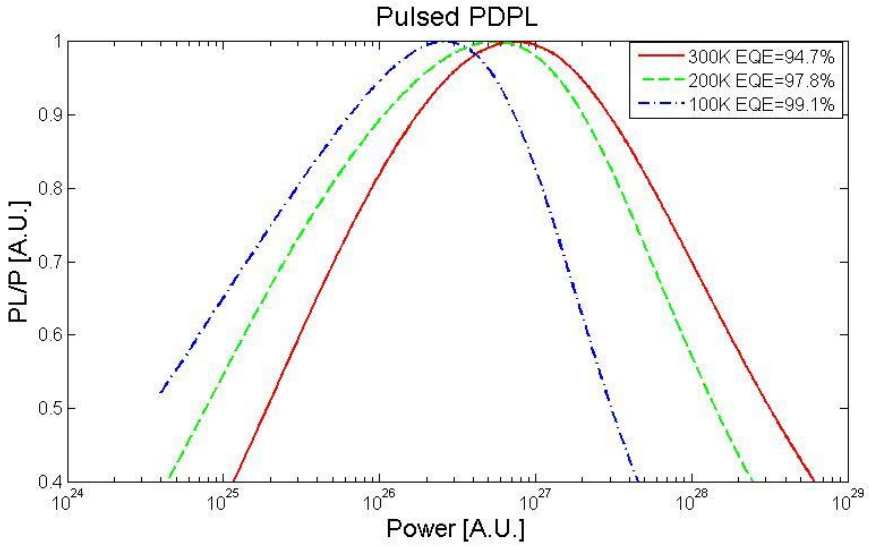

Fig.5.21. Numerical simulation of PDPL measurement at 300K, 200K and 100K without normalizing pump power.

Chapter 6

Observation and Simulation of Lateral Lasing in Semiconductors

6.1 Lateral lasing in DHS samples

During the PDPL experiment, which is covered in Chapter 5, we observe a strange phenomenon at 100K for the DHS cooling samples: the photo luminescence signal drops slightly at certain pump power then seem to be clamped at a level even when the pump power keeps increasing (See Fig.6.1).

This strange behavior prompts us to make more careful observation. The first distinct thing we notice is that when this happens, the image of the sample on a IR camera shows very bright spots on the edge of the sample (See Fig.6.2).

This makes us suspect that a laser cavity has formed in the lateral direction parallel to the surface of the sample and lateral lasing happens when the pump power reaches threshold.

We align the collection fiber so that it mainly picks up the light signal scatted from the edge of the sample. Threshold is then clearly observed when we scan the pump power (See Fig.6.3).

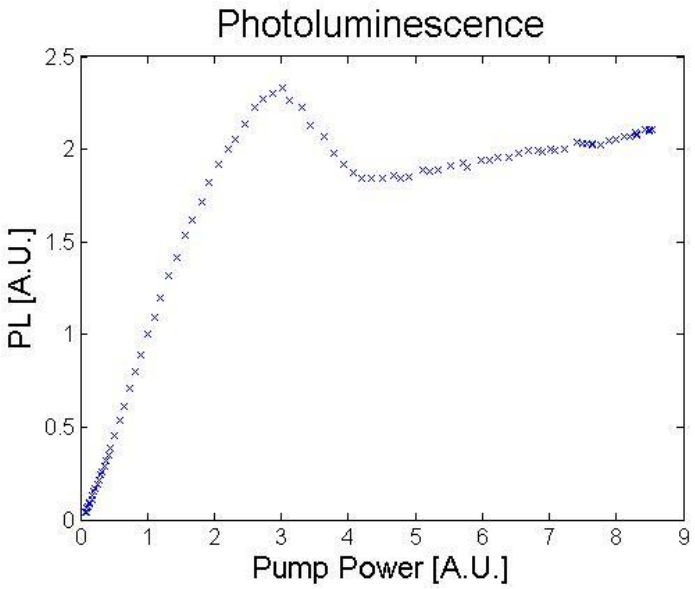

Fig.6.1 Photoluminescence signal as a function of pump power for a DHS cooling sample at 100K. PL drops and then clamps at a level when pump power increases, indicating lasing operation.

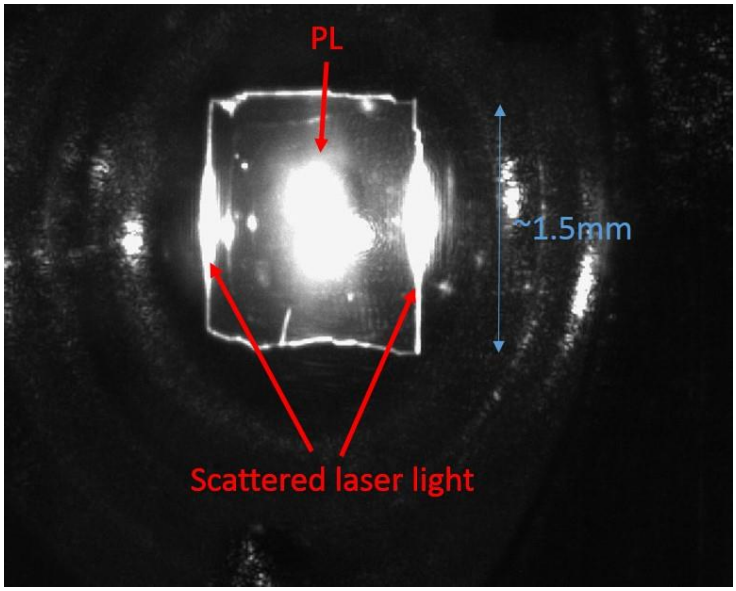

Fig.6.2. Image of square-sized DHS sample at 100K. Bright spots on the edges of sample are from scattered light of lateral lasing.

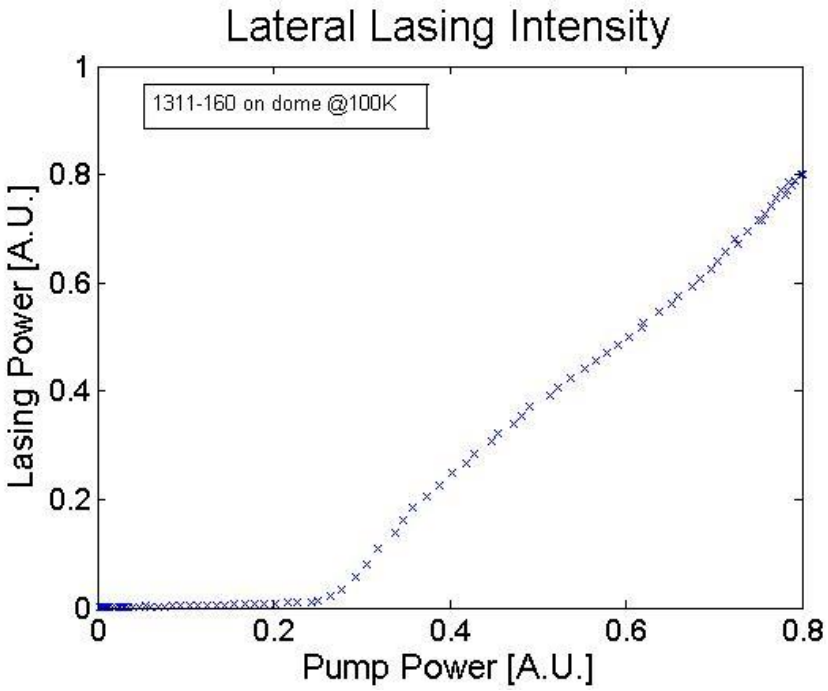

Fig.6.3 Scattered laser light as a function of pump power. Threshold behavior is observed.

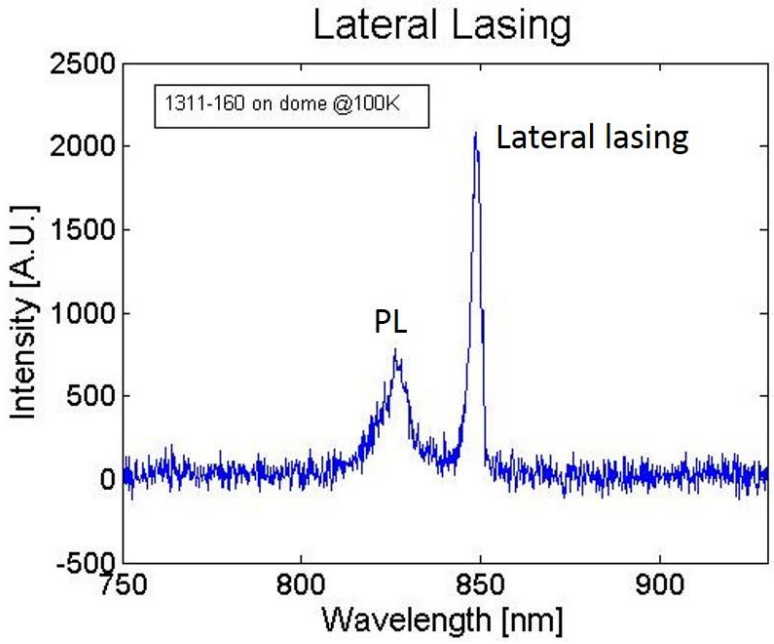

Fig.6.4 Spectrum of photoluminescence signal and lateral lasing signal on a DHS sample at 100K.

The scattered light is then sent to an Ocean Optics spectrometer and a laser peak signal is clearly seen besides the PL signal (See Fig.6.4). The lasing wavelength λ~850 nm is much longer than the peak of the luminescence at 825nm.

It is concluded then, that we have observed the effect of lateral lasing in the InGaP/GaAs/InGaP DHS sample. The reason that it was not observed at room temperature or 200K is because the semiconductor material gain increases with deceasing temperature, making the lasing threshold lower at 100K. In fact, after we increase the pump power scan range, lateral lasing is also observed at room temperature and 200K.

In addition to the square-sized sample above, we also investigated circular DHS cooling samples and observed the same lateral lasing effect at room temperature. Fig.6.5 shows the results for a 600μm diameter GaInP/GaAs/GaInP (0.75μm/0.75μm/0.75μm thick) DHS bonded to a ZnS substrate (See inset of Fig. 5-a). The lasing operation is indicated by the observation of a distinct threshold (Fig.6.5-a) at 0.33 μJ of pump pulse energy, corresponding to a threshold carrier density of $\sim 2\times 10^{19} cm^{-3}$. Similar to the square-sized sample, the lasing wavelength λ~890 nm is much longer than the peak of the luminescence at 860nm (Fig.6.5-b).

To confirm that the lasing operation indeed happen in the lateral direction, we investigate samples from the same gain chip prior to lifting off from the GaAs substrate, making it impossible to lase vertically. Similar lasing action is still observed.

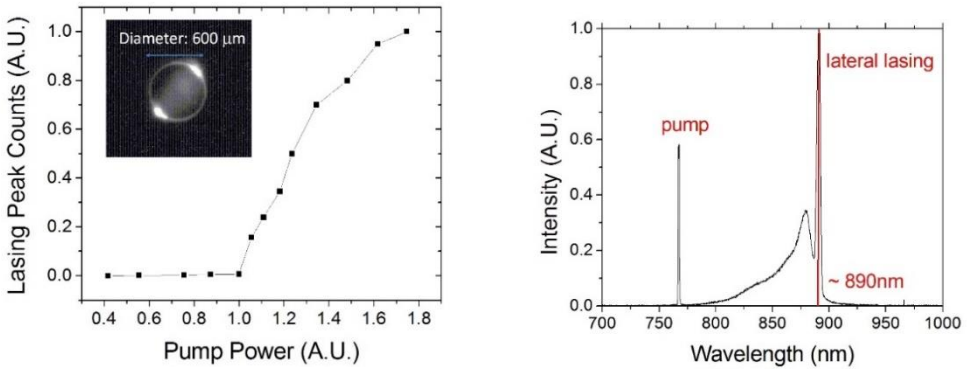

(a) (b)

Fig.6.5 (a) lateral lasing threshold is observed for a double heterostructure sample (600 µm in diameter) bonded to ZnS substrate (b) Spectral measurement showing the lateral lasing emission.

Lateral lasing action is found to be a universal phenomenon that occurs in samples with different sizes, different shapes, and with or without substrate. In addition, we observe persistent lateral lasing in multiple quantum well (MQW) samples for the application of Vertical External Cavity Surface Emitting Lasers (VECSELs).

6.2 Lateral lasing in VECSEL samples

6.2.1 Introduction

Vertical External Cavity Surface Emitting Lasers (VECSELs), also known as Optically Pumped Semiconductor Lasers (OPSLs), have been generating a great amount of interest due to their superior performance in beam quality, power scaling capability and wavelength flexibility [102-104].

In order to power scale the VECSEL device, the pump spot size needs to be increased. The large pump area will increase the gain length in the lateral plane amplifying the spontaneous emission. This effect has been mentioned in the very early development of Vertical Cavity Surface Emitting Lasers (VCSELs) [105] as well as other types of disk lasers [106]. Detection of such lateral spontaneous emission has been used to determine the non-radiative recombination coefficient in VCSELs [107] as well as for VCSEL optical power monitoring [108]. With sufficient feedback from the edges of the device, lateral lasing can be observed, which in turn hampers the lasing operation in the vertical direction [109-111]. Hessenius *et al.* also observed an interesting yet puzzling phenomenon in which lateral lasing happens even when the pump spot size is significantly smaller than the lateral dimension of the sample [109]. This implies that, the total optical gain within the small pump region has to be larger than the total optical absorption (loss) in the much longer un-pumped region of the sample. They attribute this phenomenon to the thermal shift of the bandgap: As the device is pumped, the active region begins to heat, leading to the red-shifting of the bandgap in the pumped region compared to the surrounding area. This, they reasoned, results in the un-pumped region to be transparent to the spontaneous emission from the active region.

In this Chapter, however, we show that even after the heating effect is eliminated by using a pulsed optical excitation with very low duty cycle, the same lateral lasing effect is still observed in a lifted-off VECSEL structure bonded to a crystal substrate. Such pulsed lateral lasing occurs in both multiple-quantum well (MQW) as well as double heterostructure (DHS) gain chips, and cannot be explained

by the thermal model. We propose a new model based on the effect of bandgap renormalization due to Coulomb screening (Section 6.3).

A typical VECSEL chip consists of an active region and a distributed Bragg Reflector (DBR), which has tens of pairs of lattice-matched alternating index layers. The high thermal resistance associated with the DBR layer hampers the thermal management of the gain chip and ultimately limits the power of VECSEL. A novel design, called DBR-free VECSEL, was proposed and demonstrated recently [112, 113], in which the semiconductor gain chip without DBR was lifted off from the substrate and Van Der Waals bonded to a transparent crystal. Two external mirrors complete the cavity. For gain-chip testing and screening, various samples were bonded to glass or sapphire substrates and pumped with low-duty cycle pulse lasers to avoid any thermal degradation. However, we encountered lateral lasing in many of these samples under high enough excitation.

6.2.2 Observation of lateral lasing in MQW samples

The description of the experimental setup is as follows. The MQW gain chip is grown by metalorganic chemical vapor deposition (MOCVD) and consists of 10 GaInAs quantum wells in a resonant periodic gain structure barriered by GaAs layers. The structure is passivated by AlGaAs layers both at the top and at the bottom. And another thin layer of AlGaAs layer with high Al content is grown between the substrate and the structure as a release layer for lift off. The photoluminescence of the multi quantum wells peaks at 1001nm. The optical pump source is the same used for PDPL experiment,

a miniature diode-pumped Q-switched Er:YAG laser (1535 nm) (Photop Technologies, Model DPQL-1535-C-0040-005N-03) frequency doubled to 767nm. It delivers ~3.5ns (FWHM) pulses having ~0.6 μJ energy at 1 kHz repetition rate.

Fig.6.6(a) shows the top-view image of the MQW sample during the experiment; it clearly shows the scattered (laser) light from the chip's four edges due to lateral lasing along both directions. Fig.6.6(b) is the spectrum collected from the edge of the sample. The lasing wavelength (shown in Fig.6.6(b)) is about 1030nm, much longer than the peak of the gain (λ~1005 nm) as designed for the vertical lasing operation.

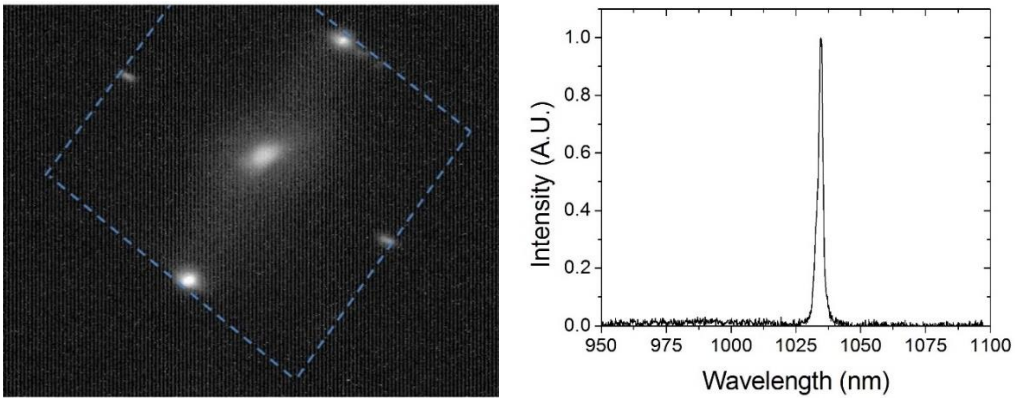

(a) (b)

Fig.6.6. (a) Quantum well sample (2mm×2mm square) bonded to substrate showing lateral lasing scattered from chip edge, (b) Spectral measurement from the edge of the sample shows the lateral lasing light emission.

6.2.3 Persistence of lateral lasing

Since lateral lasing is an unwanted effect in both PDPL and VECSEL application, we tried to suppress it by damaging of edge of the sample intentionally by a razor blade.

However, it is observed that even with damaged edges, the sample can still form a cavity for most occasions (See Fig.6.7).

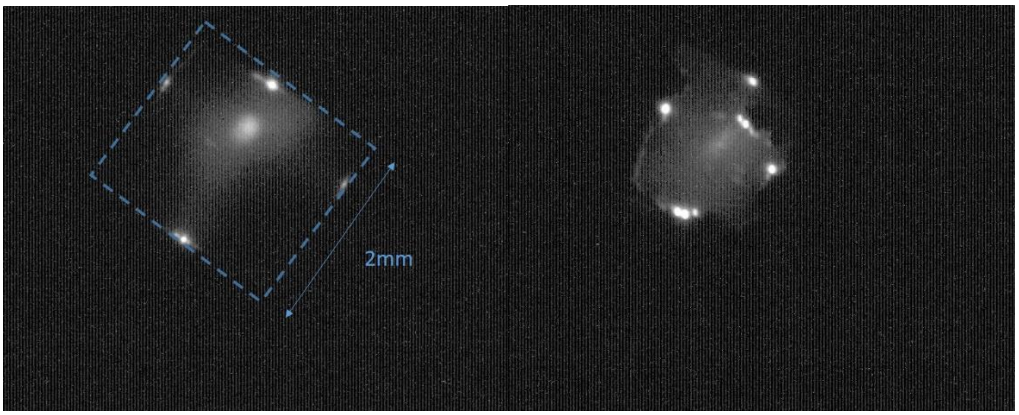

(a) (b)

Fig.6.7. (a) A square sized MQW sample showing scattered light from lateral lasing at all four edges. (b) after all four edges are damaged by a razor blade, lateral lasing persists.

As was also reported in Ref [109], it is also quite striking that lateral lasing is persistent even when the dimension of the pump area is significantly smaller than the lateral dimension of the sample. As shown in Fig.6.8, the square MQW sample is 2mm wide and long, while the pump spot size is only about 50 μm by calculation. It is also experimentally proved by a knife-edge test, in which a razor blade is placed right in front of the sample. As the blade is moved such that more than half of the sample is blocked from pump light, the scatted light at the edge of sample from lateral lasing is still clearly observed (See Fig.6.9).

The use of pulsed excitation in our experiment assures negligible heating within the active region, therefore the thermal model in Ref. [109] cannot explain the lateral lasing phenomenon observed in our samples. In the following, we present a plausible

mechanism based on bandgap renormalization due to Coulomb screening in the presence of a high concentration of optically injected electron-hole (e-h) density. We show theoretical results based on a simple plasma theory is in good agreement with the experimental data for GaAs bulk (DHS) gain chips.

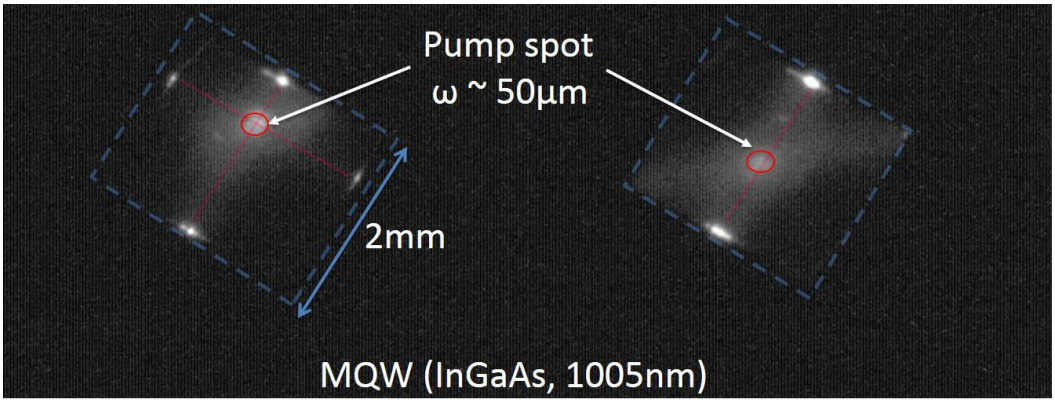

Fig.6.8. Dimension of the pump area is significantly smaller than the lateral dimension of the sample.

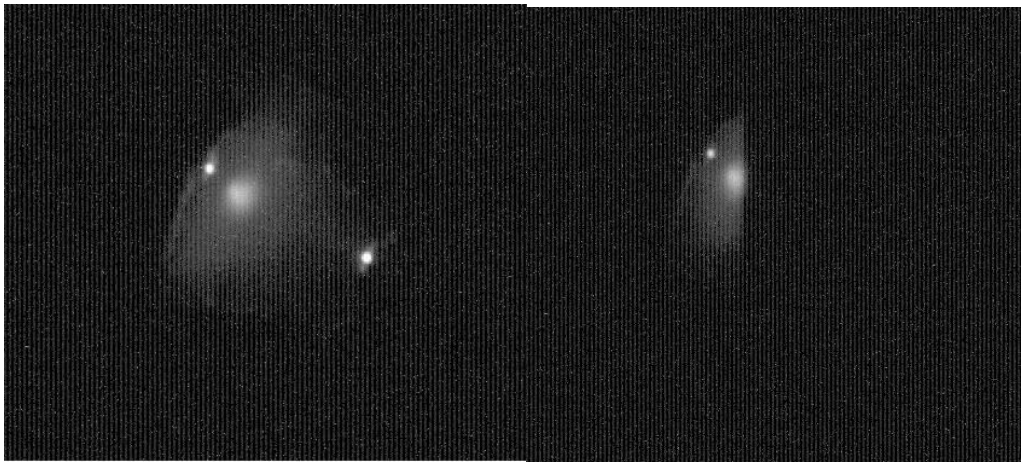

(a) (b)

Fig.6.9. (a) MQW sample shows scattered light from two edges, indicating lateral lasing. (b) Razor blade right in front of the sample blocks more than half of the sample. Lateral lasing persists.

6.3 Theory of coulomb screening and simulation

Coulomb screening is the damping of electric fields caused by the presence of mobile carriers. In semiconductors, when the excited carrier density is high, the effect of Coulomb screening will cause bandgap renormalization. Following the theory of Banyai and Koch [65, 66], the renormalized bandgap is given by

$$E_g(N) \approx E_g{}^0 - E_R / g \tag{6.1}$$

where $E_g{}^0$ is the unrenormalized semiconductor band-gap energy, $E_R = \frac{\hbar^2}{2m_r a_0{}^2}$ is the (exciton) Rydberg energy, $g = \frac{\pi^2 a_0 \kappa}{12}$ with κ denoting the inverse of Coulomb screening length as determined by:

$$\kappa^2 = \frac{e^2}{\pi^2 k_B T} \int d^3k \left[\left(1 - f_e\right) f_e + \left(1 - f_h\right) f_h \right], \tag{6.2}$$

and $a_0 = \frac{\hbar \varepsilon_0}{m_r e^2}$ is the exciton Bohr radius . Here m_r is the reduced mass of the electron-hole pair. The common physical constants used are: ε_0 =permittivity of free space, $\hbar$ =reduced Planck constant, k_B=Boltzmann constant, and e=electronic charge. At a given temperature T, the distribution of electrons and holes in the conduction and valence bands are given by the Fermi-Dirac functions:

$$f_{e,h} = \left(e^{(\varepsilon_{e,h}(k) - \mu_{e,h})/\mathrm{k_B T}} + 1 \right)^{-1} \tag{6.3}$$

where $\mu_{e,h}$ denotes the quasi-Fermi levels. Parabolic bands are assumed with dispersion $\varepsilon_{e,h}(k) - E_g{}^0 / 2 = \pm \hbar^2 k^2 / 2m_{e,h}$ where $m_{e,h}$ is the effective mass for

electrons and holes. The variation of chemical potentials with the injected electron-hole density (N) is therefore given by: $N = 2\left(m_{e,h}k_B\,T\,/2\pi\hbar^2\right)^{\frac{3}{2}}F_{1/2}\left(\mu_{e,h}/k_B\,T\right)$ where $F_{1/2}$ is the Fermi integral.

Using Eq. (6.1), we can calculate the renormalized band-gap energy for GaAs at room temperature as a function of the excited carrier density, as shown in Fig.6.10.

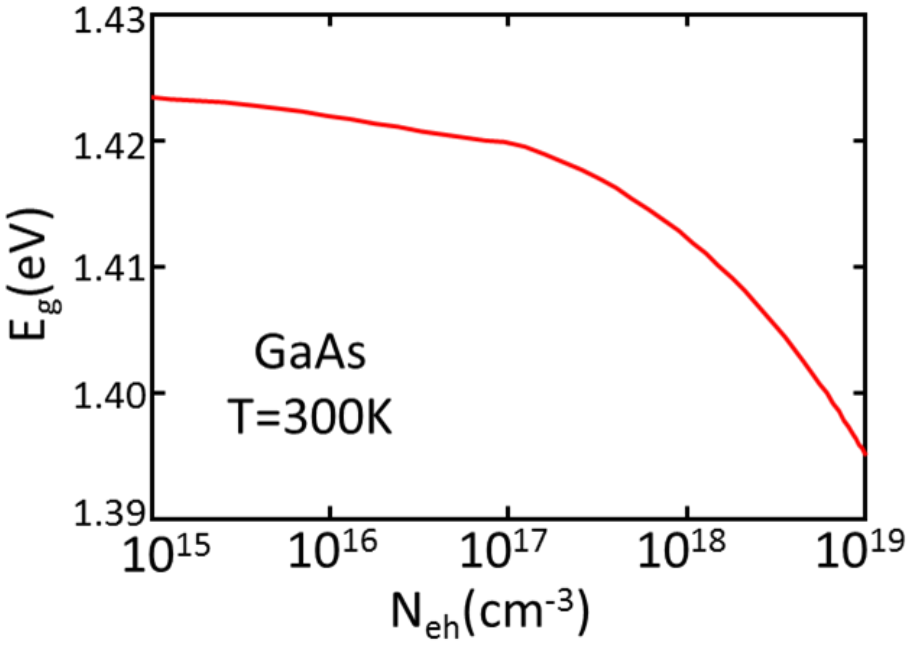

Fig.6.10. Calculated renormalized band-gap energy as a function of carrier density for GaAs at 300K.

The absorption coefficient is given by:

$$\alpha(\nu, N) = \left\{\alpha_0^{\,bound} + \alpha_0^{\,free}\right\}\left[1 - f_e - f_h\right] \tag{6.4}$$

The contributions from bound and free excitons as given by the plasma theory of Banyai and Koch [66] are:

$$\alpha_0^{bound} = \alpha_0 \sum_n \frac{1}{n}\left[\frac{1}{n^2} - \frac{n^2}{g^2}\right]\delta_\Gamma\left[\frac{\hbar\omega - E_g + E_n}{E_R}\right] \tag{6.5}$$

$$\alpha_0^{free} = \alpha_0 \int_0^\infty dx \frac{\sinh(\pi g\sqrt{x})}{\cosh(\pi g\sqrt{x}) - \cos(\pi\sqrt{4g - xg^2})}\delta_\Gamma\left[\frac{\hbar\omega - E_g}{E_R} - x\right] \tag{6.6}$$

where $E_n = E_R\left(\frac{1}{n} - \frac{n}{g}\right)^2$ is the exciton binding energy and $\delta_\Gamma(x) = \frac{1}{\pi\Gamma\cosh(x/\Gamma)}$ is a broadened delta-function having a width Γ that represents phenomenological carrier-phonon interaction. For T~300K, we assume $\Gamma \sim E_R$ [65]. From theory and experiments $\alpha_0 \sim 10^4$ cm^{-1}.

Fig.6.11-a shows the calculated absorption (gain) spectra for the active region for different carrier densities and for the un-pumped passive region of the GaInP/GaAs/GaInP double heterostructure sample at 300K.

As can be seen, the renormalized band-gap energy in the active region red-shifts the gain spectrum. When the carrier density is sufficiently high, there is a spectral window in the long-wavelength end of the gain spectrum where the passive (unpumped) region of the sample is nearly transparent. With sufficient feedback from the facets of the sample, lateral lasing will occur.

Based on the absorption and gain spectrum, we can calculate the lateral emission integrated gain spectrum for different carrier densities (Fig.6.11-b) and estimate the lasing wavelength. We calculate the roundtrip survival factor given by $R^2 exp(\gamma d - \alpha(L-D))$ where R is the Fresnel reflectivity of the facets, γ is the calculated gain (=-α from Eq. (6.4)) in the pumped region and α is the absorption in the passive

(N=0) region. The results are shown in Fig.6.11(a). The lateral dimension of the wafer (L) and diameter of the pumped region (D) are shown in the inset of the Fig.6.11(b). The result predicts a lasing wavelength of ~887nm when the carrier density is above $\sim 10^{19}\,cm^{-3}$ for the double heterostructure sample, which is in great agreement with our observation as shown in Fig.6.5(b).

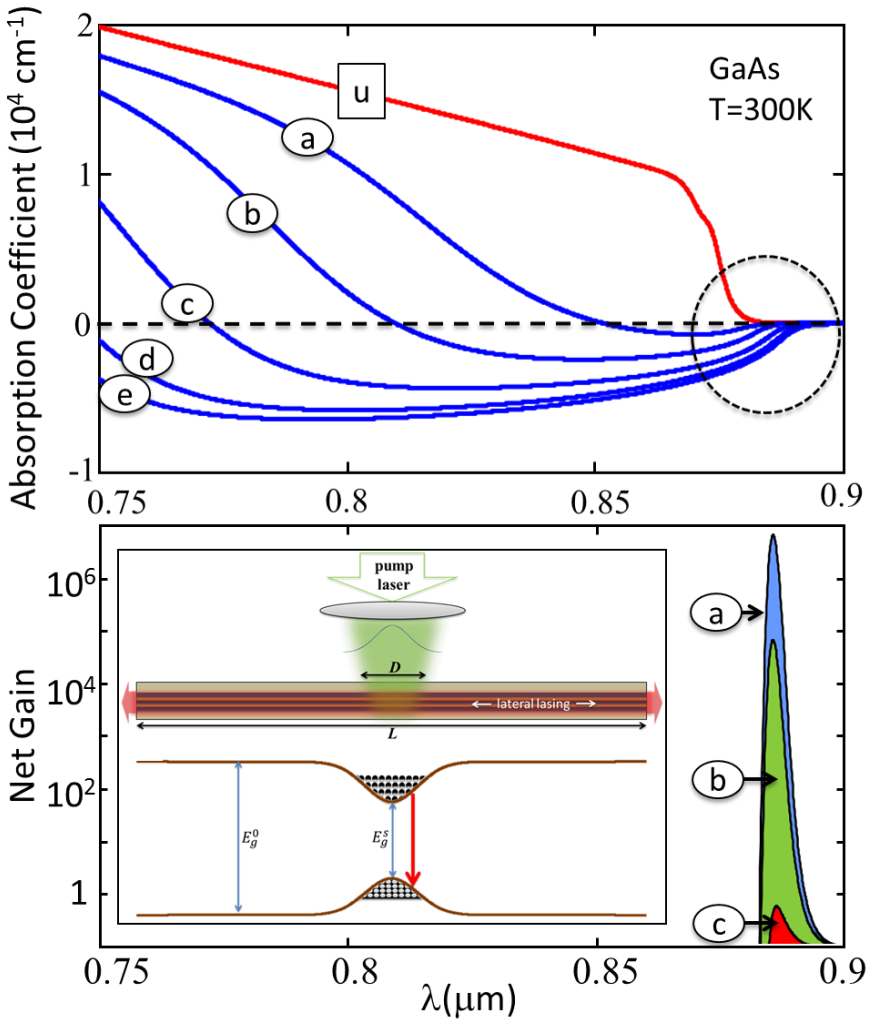

Fig.6.11. (a) Calculated absorption (gain) spectra for the active region for carrier densities of a) 2×10^{18}cm^{-3} b) 4×10^{18}cm^{-3} c) 6.5×10^{18}cm^{-3} d) 9×10^{18}cm^{-3} e) 1×10^{19}cm^{-3} and for the un-pumped passive region of the GaInP/GaAs/GaInP double heterostructure sample at 300K. (b) Simulated lateral emission spectrum for different carrier densities.

In conclusion, we observe the lateral lasing effect in both optically pumped quantum well and double heterostructure semiconductor samples and show that the phenomenon can be explained by the effect of bandgap renormalization due to Coulomb screening.

Chapter 7

Conclusions and Future Works

7.1 Conclusion

The prospects for laser cooling in III-V compound semiconductors, in particular GaAs double heterostructures (DHS), have been investigated theoretically and experimentally. The fundamental issues for achieving net cooling have been addressed. These include light extraction efficiency, the critical importance of external quantum efficiency, and the need for low background absorption.

GaInP/GaAs/GaInP DHS epilayers have been fabricated for laser cooling experiments. A procedure of epitaxial lift-off followed by direct van der Waals wafer bonding to a ZnS dome lens has been developed. Processing issues and the quality of the interface contact have been discussed.

Laser cooling experiments have been performed by extending and refining the previous work. A high sensitivity (temperature resolution: < 100 mK), non-contact thermal measurement technique called Differential Luminescence Thermometry (DLT) was developed and implemented for this purpose. Direct wafer bonding of DHS on dome lenses made from nearly index-matched low absorption material has been

used to enhance the extraction efficiency. External quantum efficiency in different devices has been measured at room temperature and low temperatures using All-optical Scanning Laser Calorimetry (ASLC) with high precision. A record external quantum efficiency of 99.5% has been obtained with a GaAs laser cooler held at 100 K. This result shows that the current GaAs-based device has sufficient EQE for the realization of net laser cooling. It is believed that deleterious background absorption in the present device design has to be identified and significantly reduced before net laser cooling can be observed.

Optimum EQE is attained at an optimum photo-excitation level that can be determined with an independent measurement of power-dependent temperature or power-dependent photoluminescence (PDPL). Pulsed Power-dependent photoluminescence measurement (Pulsed PDPL) is proved to be an efficient way to determine the quantum efficiency and screen the sample quality before processing and fabrication.

We observe the lateral lasing effect in both optically pumped quantum well and double heterostructure semiconductors and show that the phenomenon can be explained by the effect of bandgap renormalization due to Coulomb screening.

7.2 Future works

The following are suggested as future directions for research on laser cooling of semiconductors:

I) Reducing parasitic absorption is currently an ongoing and active area of research. The four possible sources of parasitic absorption are: i) the dome lens, ii) interfaces between GaAs/GaInP, DHS to dome lens or DHS to air, iii) GaInP passivating layer, and iv) GaAs active layer. Preliminary data indicates the source of background absorption is from the interfaces. More investigation is needed to verify, accurately identify and eventually reduce the background absorption.

II) Bonding quality is of critical importance to laser cooling experiment as well as other application such as VECSEL device. The current lift-off and van der Waals bonding procedures are improved based on Yablonovitch's method. The high EQE number obtained shows the good bonding quality achieved through current process. However, the consistency of bonding quality is still far from perfect, which leads to sample to sample variation and sometimes make data interpretation and comparison difficult. The possibility of introducing sources for high background absorption during fabrication needs further investigation. Areas for improvement include 1) more consistent way to apply black wax on the sample, such as using molten wax dissolved in a solution, 2) using better fixture to apply pressure after the bonding, 3) further investigation on the possibility of post annealing to improve bonding quality.

III) The effect of doping in the passivation layer is another subject of great interest. The non-radiative interface recombination physics may be favorably altered if the passivating layer is doped p-type or n-type.

IV) Even though this dissertation is dedicated for III-V compound semiconductors, the recent breakthrough of laser cooling on II-V materials opens another way to future design of material for laser cooling in semiconductors. More

understanding of the cooling results is needed and testing other II-VI materials in the single-crystal, thin-film structures would be an interesting research field.

Appendix A

Summary of ASLC data on all measurements of cooling samples

Measurement Date	Sample Number	Growth Technique	Measurement temperature [K]	Pump Power [mW]	Mean luminescence wavelength [nm]	EQE [%]	Background Absorption [cm-1]
7/14/2014	1311-160	MOCVD	100	90	826.1	78.5	15
3/30/2014	1313-412	MOCVD	100	100	825	88	150
7/5/2013	1312-522	MOCVD	100	100	826.7	94	55
3/25/2013	1312-520	MOCVD	100	60	831	96.5	25
1/14/2013	1312-345	MOCVD	100			78.1	100
12/3/2012	1312-445	MOCVD	100	120	827.2	93.6	60
10/7/2012	1312-233	MOCVD	100	100	825.6	94.4	50
10/7/2012	1312-233	MOCVD	293	100	862.3	90.2	45
5/20/2012	1311-269	MOCVD	100	60	824.7	91.5	70
5/30/2012	1311-269	MOCVD	100	50	827.2	94.9	110
5/1/2012	1311-168	MOCVD	100	50	826.1	96.6	50
4/27/2012	1311-160	MOCVD	285	150	862.3	94	100
4/27/2012	1311-160	MOCVD	in air	135	862.3	97.6	120
3/29/2012	1311-160	MOCVD	100	30	835	99.5	95
3/19/2012	1311-160	MOCVD	250		852.2	97.2	

3/19/2012	1311-160	MOCVD	100	300	833	98	35
12/10/2010	MJ537	MOCVD	200	100		84	
12/10/2010	MJ538	MOCVD	200	100		91.3	
12/1/2010	CHTM2750	MBE	200	100		88	
1/15/2010	MH701	MOCVD	200			96.5	40
1/15/2010	MH701	MOCVD	100			94.5	50
1/15/2010	MH714	MOCVD	200			85	60
1/15/2010	MH714	MOCVD	100			88	20
1/15/2010	CHTM2750	MBE	200			90	15
1/8/2010	MH701	MOCVD	200			95	20
1/8/2010	MH701	MOCVD	100			95	60
12/18/2009	2755	MBE	100	400		93	45
12/18/2009	2755	MBE	100	50		92	25
12/11/2009	MI718	MOCVD	100			78	
12/7/2009	MI718	MOCVD	285			73.4	
12/10/2009	2755	MBE	100			93.9	
11/23/2009	2755	MBE	100			91	
11/23/2009	2755	MBE	200			89.7	
11/23/2009	2755	MBE	285			82.3	
11/2/2009	MH701	MOCVD	285	400		90.6	
11/2/2009	MH701	MOCVD	285	100		90.6	
10/31/2009	MF444	MOCVD	285	50		92	
10/31/2009	MF444	MOCVD	285	400		94.9	
10/15/2009	MF444	MOCVD	285	400	853.6	94.9	
10/26/2009	MF444	MOCVD	285	400		91.6	
10/26/2009	MF444	MOCVD	285	100		91.8	
10/1/2009	MF444	MOCVD	285	50		92	
10/12/2009	MF444	MOCVD	285	400		95.3	

10/1/2009	MF444	MOCVD	285	400		96	
10/2/2009	MF444	MOCVD	100	300		93.7	
9/21/2009	MF444	MOCVD	100	50		92.5	
9/21/2009	MF444	MOCVD	200	100		92.8	
9/24/2009	MF444	MOCVD	200	100		97.3	
9/21/2009	MF444	MOCVD	200	50		93.6	
9/10/2009	MH700	MOCVD	100	100		96.6	
8/28/2009	MF444	MOCVD	100	100		94.1	
8/28/2009	MF444	MOCVD	100	100		94.5	
11/3/2008	MH700	MOCVD	100	400		94.8	
11/3/2008	MH700	MOCVD	200	50		95	
11/3/2008	MH700	MOCVD	200	50		94.5	
11/3/2008	MH701	MOCVD	77	200		97.4	
11/7/2008	MH701	MOCVD	100	100		96.9	
10/28/2008	MH701	MOCVD	200	100		96	
10/28/2008	MH701	MOCVD	285	50		94.1	
10/28/2008	MH701	MOCVD	100	200		97	
10/28/2008	MH701	MOCVD	77	400		96.8	
10/17/2008	MH701	MOCVD	100	100		96.4	
10/17/2008	MH701	MOCVD	100	400		96.2	
10/17/2008	MH701	MOCVD	100	25		95.6	
10/17/2008	MH701	MOCVD	100	100		96.9	
10/14/2008	MF444	MOCVD	100	100		94.8	
10/14/2008	MF444	MOCVD	100	25		93.2	
10/14/2008	MF444	MOCVD	100	100		94.7	
9/29/2008	MF444	MOCVD	285	500		94	
9/29/2008	MF444	MOCVD	285	300		93.3	
9/29/2008	MF444	MOCVD	285	100		93.4	

9/26/2008	MF444	MOCVD	100	500		96.3	
9/26/2008	MF444	MOCVD	100	500		96	
9/23/2008	MF444	MOCVD	285	500		94.3	
9/23/2008	MF444	MOCVD	285	500		93.9	
9/23/2008	MF444	MOCVD	100	500		95.9	
9/19/2008	MF444	MOCVD	100	100		94.7	
9/19/2008	MF444	MOCVD	100	350		95.7	
9/19/2008	MF444	MOCVD	200	100		96.3	
9/19/2008	MF444	MOCVD	200	100		94.7	
9/19/2008	MF444	MOCVD	200	200		95.2	
9/19/2008	MF444	MOCVD	200	200		95.1	
9/19/2008	MF444	MOCVD	100	50		93.1	
9/7/2008	MF444	MOCVD	100	200		94.2	
9/21/2008	MF444	MOCVD	100	200		94.7	
9/7/2008	MF444	MOCVD	100	200		93.9	
9/7/2008	MF444	MOCVD	100	200		94.8	
9/7/2008	MF444	MOCVD	100	350		96	
8/28/2008	MF444	MOCVD	100	50		94.3	
9/6/2008	MF444	MOCVD	100	50		92.8	
9/7/2008	MF444	MOCVD	100	50		93.8	
9/7/2008	MF444	MOCVD	100	50		93.1	
9/7/2008	MF444	MOCVD	100	350		95.6	
8/28/2008	MF444	MOCVD	100	100		95.4	
8/28/2008	MF444	MOCVD	100	100		93.5	
8/28/2008	MF444	MOCVD	100	100		94.9	
8/28/2008	MF444	MOCVD	100	100		95	
8/28/2008	MF444	MOCVD	100	50		93.7	
8/28/2008	MF444	MOCVD	100	100		94.3	

Glossary

Al	Aluminum
AlAs	Aluminum Arsenide
AlGaAs	Aluminum Gallium Arsenide
ASLC	All-optical Scanning Laser Calorimetry
CCD	Charge Coupled Device
CdS	Cadmium Sulfide
CHTM	Center for High Technology Materials
CW	Continuous Wave
DBR	Distributed Bragg Reflector
DHS	Double Heterostructure
DI water	Deionized water
DLT	Differential Luminescence Thermometry
EQE	External Quantum Efficiency
FCA	Free Carrier Absorption
GaAs	Gallium Arsenide
GaInP	Gallium Indium Phosphide
GaP	Gallium Phosphide
H_2O_2	Hydrogen Peroxide

HF	Hydrofluoric acid
ICP	Inductively Coupled Plasma
KMS	Kubo-Martin-Schwinger
LANL	Los Alamos National Laboratory
LED	Light Emitting Diode
LOP	Longitudinal Optical Phonon
MBE	Molecular Beam Epitaxial
MOCVD	Metalorganic Chemical Vapor Deposition
MQW	Multiple Quantum Well
NH_4OH	Ammonium Hydroxide
NREL	National Renewable Energy Laboratory
OPSL	Optically Pumped Semiconductor Laser
PDPL	Power-Dependent Photoluminescence
Pulsed-PDPL	Pulsed Power-Dependent Photoluminescence
PL	Photo Luminescence
PLE	Photoluminescence Excitation
PMT	Photo Multiplier Tube
PPLT	Pump-probe Luminescence Thermometry
RE	Rare-earth
Si	Silicon
SiO_2	Silicon Dioxide
SLN	Sandia National Laboratory
TCE	Trichloroethylene

TE cooler	Thermo-electric cooler
TRPL	Time-resolved Photoluminescence
TMGa	Trimethyl Gallium
TMIn	Trimethyl Indium
UNM	The University of New Mexico
UV	Ultraviolet
VCSEL	Vertical Cavity Surface Emitting Laser
VECSEL	Vertical External Cavity Surface Emitting Laser
ZnS	Zinc Sulfide
ZnSe	Zinc Selenide

References

[1] T. W. Hansch and A. L. Schawlow, "Cooling of gases by laser radiation," *Opt. Commun.,* vol. 13, no. 1, pp. 68-69, 1975.

[2] S. Chu, C. Cohen-Tannoudji and W. Philips, "Nobel Prize in Physics 1997 for development of methods to cool and trap atoms with laser light," 1997.

[3] E. Cornell, W. Ketterle and C. Weiman, "Nobel Prize in Physics 2001 for the achievement of Bose-Einstein condensation in dilute gases of alkali atoms, and for early fundamental studies of the properties of the condensates.," 2001.

[4] U. Vogl and M. Weitz, "Laser cooling by collisional redistribution of radiation," *Nature,* vol. 461, pp. 70-74, 2009.

[5] M. Sheik-Bahae and R. I. Epstein, "Optical refrigeration," *Nature Photonics,* vol. 1, pp. 693-699, 2007.

[6] P. Pringsheim, "Zwei Bemerkungen über den Unterschied von Lumineszenz- und Temperaturstrahlung," *Zeitschrift für Physik,* vol. 57, no. 11-12, pp. 739-746, 1929.

[7] L. Landau, "On the thermodynamics of photoluminescence," *Journal of Physics (Moscow),* vol. 10, pp. 503-506, 1946.

[8] R. I. Epstein, M. I. Buchwald, B. C. Edwards, T. R. Gosnell and C. E. Mungan, "Observation of laser induced fluorescent cooling of a solid," *Nature,* vol. 377, pp. 500-503, 1995.

[9] B. C. Edwards, M. I. Buchwald and R. I. Epstein, "Development of the Los-Alamos Solid-State Optical Refrigerator," *Rev. Sci. Instrum.,* vol. 69, no. 5, pp. 2050-2055, 1998.

[10] B. C. Edwards, J. E. Anderson, R. I. Epstein, G. L. Mills and A. J. Mord, "Demonstration of a solid-state optical cooler: An approach to cryogenic refrigeration," *J. Appl. Phys.,* vol. 86, no. 11, pp. 6489-6493, 1999.

[11] D. V. Seletskiy, S. D. Melgaard, S. Bigotta, A. D. Lieto, M. Tonelli and M. Sheik-Bahae, "Laser cooling of solids to cryogenic temperatures," *Nature Photonics,* vol. 4, pp. 161-164, 2010.

[12] S. Melgaard, D. Seletskiy, A. Albrecht and M. Sheik-Bahae, "Optical refrigeration demonstrates the first cooling below 100K," in *presentation at Laser Refrigeration of Solids VIII*, San Francisco, 2015.

[13] G. Mills and W. Good, "Modeling the performance of optical refrigerators," in *Ball space talk in laser cooling workshop*, 2005.

[14] G. Mills and A. Mord, "Performance modeling of optical refrigerators," *Cryogenics,* vol. 46, no. 2-3, pp. 176-182, 2006.

[15] S. Bowman, "Lasers without internal heat generation," *IEEE Journal of Quantum Electronics,* vol. 35, no. 1, pp. 115-122, 1999.

[16] S. Bowman and C. Mungan, "New materials for optical cooling," *Applied Physics B* , vol. 71, no. 6, pp. 807-811, 2000.

[17] J. Fernández, A. Mendioroz, A. J. Garcá, R. Balda and J. L. Adam, "Anti-stokes laser-induced internal cooling of Yb^{+3}-doped glasses," *Phys. Rev. B,* vol. 62, no. 5, pp. 3213-3217, 2000.

[18] J. Thiede, J. Distel, S. R. Greenfield and R. I. Epstein, "Cooling to 208 K by optical refrigeration," *Appl. Phys. Lett.,* vol. 86, no. 15, p. 154107, 2005.

[19] R. I. Epstein, J. J. Brown, B. C. E. Gibbs and A. Gibbs, "Measurements of optical refrigeration in ytterbium-doped crystals," *J. Appl. Phys.,* vol. 90, no. 9, pp. 4815-4819, 2001.

[20] A. Mendioroz, J. Fernández, M. Voda, M. Al-Saleh, R. Balda and A. J. Garcá-Adeva, "Anti-stokes laser cooling in Yb^{3+}-doped KPb_2Cl_5 crystal," *Optics Letters,* vol. 27, no. 17, pp. 1525-1527, 2002.

[21] S. Bigotta, D. Parisi, L. Bonelli, A. Toncelli, M. Tonelli and A. D. Lieto, "Spectroscopic and laser cooling results on Yb^{3+} -doped BaY_2F_8 single crystal," *J. Appl. Phys.,* vol. 100, no. 1, p. 013109, 2006.

[22] C. W. Hoyt, M. Sheik-Bahae, R. I. Epstein, B. C. Edwards and J. E. Anderson, "Observation of anti-stokes fluorescence cooling in thulium-doped glass," *Phys. Rev. Lett.,* vol. 85, no. 17, pp. 3600-3603, 2000.

[23] C. W. Hoyt, M. P. Hasselbeck, M. Sheik-Bahae, R. I. Epstein, S. Greenfield, J. Thiede, J. Distel and J. Valencia, "Advances in laser cooling of thulium-doped glass," *Journal of the Optical Society of America B,* vol. 20, no. 5, pp. 1066-1074, 2003.

[24] W. Patterson, S. Bigotta, M. Sheik-Bahae, D. Parisi, M. Tonelli and R. Epstein, "Anti-Stokes luminescence cooling of Tm^{3+}doped BaY_2F_8," *Optics Express*, vol. 16, no. 3, pp. 1704-1710, 2008.

[25] J. Fernandez, A. J. Garcia-Adeva and R. Balda, "Anti-Stokes laser cooling in bulk erbium-doped materials," *Phys. Rev. Lett.*, vol. 97, no. 3, p. 033001, 2006.

[26] A. J. Garcia-Adeva, R. Balda and J. Fernandez, "Upconversion cooling of Er-doped low-phonon fluorescent solids," *Phys. Rev. B*, vol. 79, no. 3, p. 033110, 2009.

[27] G. Rupper, N. H. Kwong and R. Binder, "Large excitonic enhancement of optical refrigeration in semiconductors," *Phys. Rev. Lett.*, vol. 97, no. 11, p. 117401, 2006.

[28] A. N. Oraevsky, "Cooling of semiconductors by laser radiation," *Journal of Russian Laser Research*, vol. 17, no. 5, pp. 471-479, 1995.

[29] L. A. Rivlin and A. A. Zadernovky, "Laser cooling of semiconductors," *Optics Communications*, vol. 139, no. 4-6, pp. 219-222, 1997.

[30] M. Sheik-Bahae and R. I. Epstein, "Can laser light cool semiconductors?," *Phys. Rev. Lett.*, vol. 92, no. 24, p. 247403, 2004.

[31] G. Rupper, N. H. Kwong and R. Binder, "Optical refrigeration of GaAs: Theoretical study," *Phys. Rev. B*, vol. 76, no. 24, p. 245203, 2007.

[32] D. Huang, T. Apostolova, P. M. Alsing and D. A. Cardimona, "Spatially selective laser cooling of carriers in semiconductor quantum wells," *Phys. Rev. B*, vol. 72, no. 19, p. 195308, 2005.

[33] D. Huang and P. M. Alsing, "Many-body effects on optical carrier cooling in intrinsic semiconductors at low lattice temperatures," *Phys. Rev. B*, vol. 78, no. 3, p. 035206, 2008.

[34] J. B. Khurgin, "Role of bandtail states in laser cooling of semiconductors," *Phys. Rev. B*, vol. 77, no. 23, p. 235206, 2008.

[35] J. B. Khurgin, "Surface plasmon-assisted laser cooling of solids," *Phys. Rev. Lett.*, vol. 98, no. 17, p. 177401, 2007.

[36] J. B. Khurgin, "Band gap engineering for laser cooling of semiconductors," *J. Appl. Phys.*, vol. 100, no. 11, p. 113116, 2006.

[37] J.-B. Wang, S. R. Johnson, D. Ding, S.-Q. Yu and Y.-H. Zhang, "Influence of photon recycling on semiconductor luminescence refrigeration," *J. Appl. Phys.*, vol. 100, no. 4, p. 043502, 2006.

[38] J. Li, "Laser cooling of semiconductor quantum wells: Theoretical framework and strategy for deep optical refrigeration by luminescence upconversion," *Phys. Rev. B*, vol. 75, no. 15, p. 155315, 2007.

[39] Y. Rakovich, J. Donegan, M. Vasilevskiy and A. Rogach, "Anti-Stokes cooling in semiconductor nanocrystal quantum dots: A feasibility study," *physica status solidi A*, vol. 206, no. 11, pp. 2497-2509, 2009.

[40] G. Rupper, N. H. Kwong, R. Binder, C.-Y. Li and M. Sheik-Bahae, "Effect of n-p-n heterostructures on interface recombination and semiconductor laser cooling," *J. Appl. Phys.*, vol. 108, no. 11, p. 113118, 2010.

[41] H. Gauck, T. H. Gfroerer, M. J. Renn, E. A. Cornell and K. A. Bertness, "External radiative quantum efficiency of 96% from a GaAs/GaInP heterostructure," *Applied Physics A* , vol. 64, no. 2, pp. 143-147, 1997.

[42] E. Finkeißen, M. Potemski, P. Wyder, L. Viña and G. Weimann, "Cooling of a semiconductor by luminescence up-conversion," *Appl. Phys. Lett.*, vol. 75, no. 9, pp. 1258-1260, 1999.

[43] T. H. Gfroerer, E. A. Cornell and M. W. Wanlass, "Efficient directional spontaneous emission from an InGaAs/InP heterostructure with an integral parabolic reflector," *J. Appl. Phys.*, vol. 84, no. 9, pp. 5360-5362, 1998.

[44] B. Imangholi, M. P. Hasselbeck, M. Sheik-Bahae, R. I. Epstein and S. Kurtz, "Effects of epitaxial lift-off on interface recombination and laser cooling in GaInP/GaAs heterostructures," *Appl. Phys. Lett.*, vol. 86, no. 8, p. 081104, 2005.

[45] S. Eshlaghi, W. Worthoff, A. D. Wieck and D. Suter, "Luminescence upconversion in GaAs quantum wells," *Phys. Rev. B*, vol. 77, no. 24, p. 245317, 2008.

[46] C. Wang, C.-Y. Li, M. P. Hasselbeck, B. Imangholi and M. Sheik-Bahae, "Precision, All-Optical Measurement of External Quantum Efficiency in Semiconductors," *J. Appl. Phys.*, vol. 109, no. 9, p. 093108, 2011.

[47] D. A. Bender, J. G. Cederberg, C. Wang and M. Sheik-Bahae, "Development of high quantum efficiency GaAs/GaInP double heterostructures for laser cooling," *Appl. Phys. Lett.*, vol. 102, no. 25, p. 252102, 2013.

[48] J. Zhang, D. Li, R. Chen and Q. Xiong, "Laser cooling of a semiconductor by 40 Kelvin," *Nature,* vol. 493, pp. 504-508, 2013.

[49] B. Imangholi, *Investigation of Laser Cooling in Semiconductors, PhD Dissertation,* Univ. New Mexico, 2006.

[50] M. P. Hasselbeck, M. Sheik-Bahae and R. I. Epstein, "Effect of high carrier density on luminescence thermometry in semiconductors," in *Proc. SPIE 6461, Laser Cooling of Solids,* San Jose, 2007.

[51] D. Huppert, M. Evenor and Y. Shapira, "Measurements of surface recombination velocity on CdS surfaces and Au interfaces," *Journal of Vacuum Science & Technology A,* vol. 2, no. 2, pp. 532-533, 1984.

[52] P. Asbeck, ", Self-absorption effects on radiative lifetime in GaAs-GaAlAs double heterostructures," *J. Appl. Phys.,* vol. 48, no. 2, pp. 820-822, 1977.

[53] P. K. Basu, Theory of optical processes in semiconductors, Clarendon Press, 1998.

[54] J. I. Pankove, Optical processes in semiconductors, New York: Dover Publication, 1971.

[55] G. N. Childs, S. Brand and R. A. Abram, "Intervalence band absorption in semiconductor laser materials," *Semicond. Sci. Technol.,* vol. 1, no. 2, pp. 116-120, 1986.

[56] S. Li, Semiconductor physical electronics, Springer, 2006.

[57] S. L. Chuang, Physics of Optoelectronic Devices, Wiley, 1995.

[58] J. Piprek, Semiconductor Optoelectronic Devices: Introduction to Physics and Simulation, Academic Press, 2003.

[59] A. Haug, "Free-carrier absorption in semiconductor-lasers," *Semicond. Sci. Technol.,* vol. 7, no. 3, pp. 373-378, 1992.

[60] H. Yi, J. Diaz, B. Lane and M. Razeghi, "Optical losses of Al-free lasers for λ=0.808 and 0.98 μm," *Appl. Phys. Lett.,* vol. 69, no. 20, pp. 2983-2985, 1996.

[61] G. P. Agrawal and N. K. Dutta, Long-Wavelength Semiconductor, Springer, 2012.

[62] G. W. '. Hooft and C. v. Opdorp, "Temperature-dependence of interface recombination and radiative recombination in (Al, Ga)As heterostructures," *Appl. Phys. Lett.,* vol. 42, no. 9, pp. 813-815, 1983.

[63] R. K. Ahrenkiel, J. M. Olson, D. J. Dunlavy, B. M. Keyes and A. E. Kibbler, "Recombination velocity of the $Ga_{0.5}In_{0.5}P$/GaAs interface," *J. Vac. Sci. Technol. A,* vol. 8, no. 3, pp. 3002-3005, 1990.

[64] J. M. Olson, R. K. Ahrenkiel, D. J. Dunlavy, B. Keyes and A. E. Kibbler, "Ultralow recombination velocity of the $Ga_{0.5}In_{0.5}P$/GaAs heterointerfaces," *Appl. Phys. Lett.*, vol. 55, no. 12, pp. 1208-1210, 1989.

[65] L. Bányai and S.W.Koch, "A simple theory for the effects of plasma screening on the optical-spectra of highly excited semiconductors," *Zeitschrift für Physik B,* vol. 63, no. 3, pp. 283-291, 1986.

[66] H. Haug and S. Koch, Quantum Theory of the Optical and Electronic Properties of Semiconductors, Singapore: World Scientific , 1994.

[67] J. P. Löwenau, F. M. Reich and E. Gornik, "Many-body theory of room-temperature optical nonlinearities in bulk semiconductors," *Phys. Rev. B,* vol. 51, no. 7, pp. 4159-4165, 1995.

[68] T. Meier and S. Koch, "Coulomb correlation signatures in the excitonic optical nonlinearities of semiconductors," in *Ultrafast Physical Processes in Semiconductors,* San Diego, Academic Press, 2001, pp. 231-313.

[69] J. Verdeyen, Laser electronics, Prentice Hall, 2000.

[70] D. Gräf, M. Grundner, D. Lüdecke and R. Schulz, "Reaction of hydrofluoric acid and water with the GaAs(100) surface," *J. Vac. Sci. Technol. A,* vol. 8, no. 3, pp. 1955-1960, 1990.

[71] X. Xu, L. Coldren and J. Merz, "Selective etching characteristics of HF for $Al_xGa_{1-x}As$/GaAs," *Electronics Letters,* vol. 21, no. 13, pp. 558-559, 1985.

[72] M. M. A. J. Voncken, J. J. Schermer, A. T. J. v. Niftrik, G. J. Bauhuis, P. Mulder, P. K. Larsen, T. P. J. Peters, B. d. Bruin, A. Klaassen and J. J. Kelly, "Etching AlAs with HF for Epitaxial Lift-Off Applications," *J. Electrochem. Soc.,* vol. 151, no. 5, pp. 347-352, 2004.

[73] Z. Liau, "Semiconductor wafer bonding via liquid capillarity," *Appl. Phys. Lett.,* vol. 77, no. 5, pp. 651-653, 2000.

[74] E. Yablonovitch, T. Sands, D. M. Hwang, I. Schnitzer, T. J. Gmitter, S. K. Shastry, D. S. Hill and J. C. C. Fan, "Van der Waals bonding of GaAs on Pd leads to a permanent, solid-phase-topotaxial, metallurgical bond," *Appl. Phys. Lett. ,* vol. 59, no. 24, pp. 3159-3161, 1990.

[75] E. Yablonovitch, D. M. Hwang, T. J. Gmitter, L. T. Florez and J. P. Harbison, "Van der Waals bonding of GaAs epitaxial liftoff films onto arbitrary substrates," *Appl. Phys. Lett.* , vol. 56, no. 24, pp. 2419-2421, 1990.

[76] P. Demeester, I. Pollentier, P. D. Dobbelaere, C. Brys and P. V. Daele, "Epitaxial lift-off and its applications," *Semicond. Sci. Technol.,* vol. 8, no. 6, pp. 1124-1135, 1993.

[77] J. Lepore, "An improved technique for selective etching of GaAs and $Ga_{1-x}Al_xAs$," *J. Appl. Phys.,* vol. 51, no. 12, p. 6441, 1980.

[78] O. D. Miller, E. Yablonovitch and S. R. Kurtz, "Strong internal and external luminescence as solar cells approach the Shockley-Queisser limit," *IEEE Journal of Photovoltaics,* vol. 2, no. 3, pp. 303-311, 2012.

[79] I. Schnitzer, E. Yablonovitch, C. Caneau and T. J. Gmitter, "Ultrahigh spontaneous emission quantum efficiency, 99.7% internally and 72% externally, from AlGaAs/GaAs/AlGaAs double heterostructures," *Appl. Phys. Lett.,* vol. 62, no. 2, p. 131, 1993.

[80] D. J. Dunstan, "On the measurement of absolute radiative and non-radiative recombination efficiencies in semiconductor lasers," *Journal of Physics D: Applied Physics,* vol. 25, no. 12, pp. 1825-1828, 1992.

[81] K. R. Catchpole, K. L. Lin, P. Campbell, M. A. Green, A. W. Bett and F. Dimroth, "High external quantum efficiency of planar semiconductor structures," *Semicond. Sci. Technol.,* vol. 19, no. 11, pp. 1232-1235, 2004.

[82] R. K. Ahrenkiel, B. M. Keyes and D. J. Dunlavy, "Intensity-dependent minority-carrier lifetime in III-V semiconductors due to saturation of recombination centers," *J. Appl. Phys.,* vol. 70, no. 1, p. 225, 1991.

[83] I. Schnitzer, E. Yablonovitch, C. Caneau, T. J. Gmitter and A. Scherer, "30% external quantum efficiency from surface textured, thin-film light-emitting diodes," *Appl. Phys. Lett.,* vol. 63, no. 16, p. 2174, 1993.

[84] S. Fan, P. R. Villeneuve, J. D. Joannopoulos and E. F. Schubert, "High extraction efficiency of spontaneous emission from slabs of photonics crystals," *Phys. Rev. Lett.* , vol. 78, no. 17, p. 3294, 1997.

[85] W. N. Carr and G. E. Pittman, "One-watt GaAs p-n junction infrared source," *Appl. Phys. Lett.,* vol. 3, no. 10, p. 173, 1963.

[86] B. Imangholi, M. P. Hasselbeck and M. Sheik-Bahae, "Absorption spectra of wide-gap semiconductors in their transparency region," *Optics Communications*, vol. 227, no. 4-6, pp. 337-341, 2003.

[87] Z. Zhang and L. Grattan, Fiber Optic Fluorescence Thermometry, Springer, 1994.

[88] R. Bhat, M. Koza, M. Brasil, R. Nahory, C. Palmstrom and B. Wilkens, "Interface control in GaAs/GaInP superlattices grown by OMCVD," *Journal of Crystal Growth*, vol. 124, no. 1-4, pp. 576-582, 1992.

[89] T. Nittono, S. Sugitani and F. Hyuga, "Photoluminescence characterization of InGaP/GaAs heterostructures grown by metalorganic chemical vapor deposition," *J. Appl. Phys.* , vol. 78, no. 9, p. 5387, 1995.

[90] R. Kudela, M. Kucera, B. Olejnikova, P. Elias, S. Hasenohrl and J. Novak, "Formation of interfaces in InGaP/GaAs/InGaP quantum wells," *Journal of Crystal Growth*, vol. 212, no. 1-2, pp. 21-28, 2000.

[91] T. Sharma, M. Gokhale and B. Arora, "Long-wavelength photoluminescence from InGaP/GaAs heterointerfaces grown by metal organic vapour-phase epitaxy," *Journal of Crystal Growth*, vol. 213, no. 3-4, pp. 241-249, 2000.

[92] X. Zhang, J. Ryou, R. Dupuis, G. Walter and N. Holonyak, "Metalorganic chemical vapor deposition growth and characterization of InGaP/GaAs superlattices," *Journal of Electronic Materials*, vol. 35, no. 4, pp. 705-710, 2006.

[93] R. B. Laghumavarapu, N. Nuntawong, A. R. Albrecht and D. L. Huffaker, "Growth and characterization of GaAs/InGaP heterostructure for semiconductor laser cooling," in *Proc. SPIE 6461, Laser Cooling of Solids*, San Jose, 2007.

[94] T. Nakano, T. Shioda, E. Abe, M. Sugiyama, N. Enomoto, Y. Nakano and Y. Shimogaki, "Abrupt InGaP/GaAs heterointerface grown by optimized gas-switching sequence in metal organic vapor phase epitaxy," *Appl. Phys. Lett.*, vol. 92, no. 11, p. 112106, 2008.

[95] C. Frigeri, G. Attolini, M. Bosi, C. Pelosi and F.Germini, "Parasitic Interlayer at the GaAs-on-InGaP Interface in MOVPE InGaP/GaAs : A Study by the Chemically Sensitive (200) Diffraction," *J. Electrochem. Soc.*, vol. 156, no. 6, pp. H448-H452, 2009.

[96] N. Giannini, J. R. Silva, C. Wang, A. R. Albrecht, S. D. Melgaard and M. Sheik-Bahae, "High sensitivity background absorption measurements in

semiconductors," in *Proc. SPIE 9380, Laser Refrigeration of Solids VIII*, San Francisco, 2015.

[97] J. Shen, R. D. Lowe and R. D. Snook, "A model for the cw laser induced mode-mismatched dual beam thermal lens spectrometry," *Chemical Physics*, vol. 165, no. 2-3, pp. 385-396, 1992.

[98] A. Marcano, C. Loper and N. Melikechi, "Pump-probe mode-mismatched thermal lens Z-scan," *Journal of the Optical Society of America B,* vol. 19, no. 1, pp. 119-124, 2002.

[99] L. Pavesi and M. Guzzi, "Photoluminescence of $Al_xGa_{1-x}As$ alloys," *J. Appl. Phys.,* vol. 75, no. 10, p. 4779, 1994.

[100] J. E. Fouquet and A. E. Siegman, "Room-temperature photoluminescence times in a $GaAs/Al_xGa_{1-x}As$ molecular beam epitaxy multiple quantum well structure," *Appl. Phys. Lett.,* vol. 46, no. 3, p. 280, 1985.

[101] J. Fouquet and R. Burnham, "Recombination dynamics in $GaAs/ Al_xGa_{1-x}As$ quantum well structures," *IEEE Journal of Quantum Electronics,* vol. 22, no. 9, pp. 1799-1810, 1986.

[102] M. Kuznetsov, F. Hakimi, R. Sprague and A. Mooradian, "Design and characteristics of high-power (>0.5-W CW) diode-pumped vertical-external-cavity surface-emitting semiconductor lasers with circular TEM_{00} beams," *IEEE Journal of Selected Topics in Quantum Electronics,* vol. 5, no. 3, pp. 561-573, 1999.

[103] O. G. Okhotnikov, Semiconductor Disk Lasers: Physics and Technology, Wiley, 2010.

[104] B. Heinen, T.-L. Wang, M. Sparenberg, A. Weber, B. Kunert, J. Hader, S. Koch, J. Moloney, M. Koch and W. Stolz, "106 W continuous-wave output power from vertical-external-cavity surface-emitting laser," *Electronics Letters,* vol. 48, no. 9, pp. 516-517, 2012.

[105] K. Iga, F. Koyama and S. Kinoshita, "Surface emitting semiconductor lasers," *IEEE Journal of Quantum Electronics,* vol. 24, no. 9, pp. 1845-1855, 1988.

[106] G. JA, G. S and T. JB., "Parasitic suppression in large aperture Nd:glass disk laser amplifiers," *Appl. Opt. ,* vol. 13, no. 12, pp. 2808-2811, 1974.

[107] J. Shin and Y. H. Lee, "Determination of nonradiative recombination coefficients of vertical-cavity surface-emitting lasers from lateral spontaneous emission," *Appl. Phys. Lett.,* vol. 67, no. 3, pp. 314-316, 1995.

[108] C. Bringer, V. Bardinal, E. Daran, T. Camps, Y. G. Boucher, G. Almuneau, O. Gauthier-Lafaye, P. Dubreuil, J.-B. Doucet and C. Fontaine, "Detection of lateral spontaneous emission for VCSEL monitoring," in *Proc. SPIE 5453, Micro-Optics, VCSELs, and Photonic Interconnects*, 2004.

[109] C. Hessenius, M. Fallahi, J. Moloney and R. Bedford, "Lateral lasing and ASE reduction in VECSELs," in *Proc. SPIE 7919, Vertical External Cavity Surface Emitting Lasers (VECSELs)*, San Francisco, 2011.

[110] R. G. Bedford, M. Kolesik, J. L. A. Chilla, M. K. Reed, T. R. Nelson and J. V. Moloney, "Power-limiting mechanisms in VECSELs," in *Proc. SPIE 5814, Enabling Photonics Technologies for Defense, Security, and Aerospace Applications*, Orlando, 2005.

[111] S. Kaspar, M. Rattunde, T. Topper, R. Moser, S. Adler, C. Manz, K. Kohler and J. Wagner, "Recent Advances in 2-μm GaSb-Base Semiconductor Disk Laser—Power Scaling, Narrow-Linewidth and Short-Pulse Operation," *IEEE Journal of Selected Topics in Quantum Electronics*, vol. 19, no. 4, p. 1501908, 2013.

[112] M. Sheik-Bahae, "Evanescent-Wave Subcavity Amplifiers and Lasers". United States Patent 11,845,367, 2007.

[113] Z. Yang, A. R. Albrecht, J. G. Cederberg and M. Sheik-Bahae, "DBR-free optically pumped semiconductor disk lasers," in *Proc. SPIE 9349, Vertical External Cavity Surface Emitting Lasers (VECSELs) V*, San Francisco, 2015.